TEXTURAL AND CHEMICAL CONSEQUENCES OF INTERACTION BETWEEN HYDROUS MAFIC AND FELSIC MAGMAS: AN EXPERIMENTAL STUDY

Mattia Pistone [1,2], Jonathan D. Blundy [1], Richard A. Brooker [1], EIMF [3]

1) *School of Earth Sciences, University of Bristol, Wills Memorial Building, Queen's Road, BS8 1RJ, Bristol, United Kingdom.*

2) *Department of Mineral Sciences, National Museum of Natural History, Smithsonian Institution, 10th Street & Constitution Avenue NW, Washington, DC 20560-0119, United States.*

3) *Edinburgh Ion Microprobe Facility, School of Geosciences, University of Edinburgh, Grant Institute, Kings Buildings, West Mains Road, EH9 3JW, Edinburgh, United Kingdom.*

Abstract

Mantle-derived, hydrous mafic magmas are often invoked as a mechanism to transfer heat, mass and volatiles to felsic plutons in Earth's crust. Field observations suggest that mafic, water-rich magmas often intrude viscous felsic crystal-rich mushes. This scenario can advect water from the crystallising mafic magma to the felsic magma, leading to an increase of melt fraction in the felsic mush, and subsequent mobilisation, at the same time as the mafic magma becomes quenched through a combination of cooling and water loss. To investigate such a scenario we conducted experiments on a water-undersaturated (4 wt.% H_2O in the interstitial melt) dacitic crystal mush (50-80 vol.% quartz crystals) subject to volatile supply from a water-saturated ($\geq$ 6 wt.% H_2O) andesite magma at 950 °C and 4 kbar (12 km depth). Our experimental run products show unidirectional solidification textures (i.e. comb layering) as crystals nucleate at the mafic-felsic interface and grow into the mafic end-member. This process is driven by isothermal and isobaric undercooling resulting from a change in liquidus temperature as water migrates from the mafic to the felsic

magma. We refer to this process as "chemical quenching" and suggest that some textures associated with natural mafic-felsic interactions are not simply cooling-driven in origin, but can be caused by exsolution of volatiles adjacent to an interface, whether a water-undersaturated felsic magma (as in our experiments) or a fracture.

1. Introduction

Mantle-derived, hydrous mafic magmas provide heat, mass and volatiles to felsic magma reservoirs in Earth's crust. Inputs of mafic magma can lead to a wide range of physical and chemical interactions. Mafic dykes, sheets and inclusion swarms are commonly associated with granitoids worldwide (e.g. Blundy and Sparks 1992; John and Blundy 1993; Sisson et al. 1996; Czuppon et al. 2012). Mafic magmas have been frequently invoked as a means of contributing to crustal pluton construction (e.g. John and Blundy 1993; de Saint Blanquat et al. 2006; Leuthold et al. 2012), sustaining shallow magmatic bodies (e.g. Murphy et al. 2000; Ruprecht and Bachmann 2010; Ruprecht et al. 2012) and favouring the generation of ore deposits (e.g. Hattori and Keith 2001; Sinclair 2007; Blundy et al. 2015). Primary, subduction-related mafic magmas are generally crystal-poor and hydrous (H_2O contents of 1-7 wt.%, with 4 wt.% on average; Sisson and Layne 1993; Ulmer 2001; Plank et al. 2013; CO_2 contents of > 250 ppm; Cervantes and Wallace 2003), and intrude more felsic magmas resident in shallower crustal reservoirs. These felsic magmas are generally crystal-rich mushes and rheologically locked-up (solid fraction $\geq$ 0.5, Bachmann and Bergantz 2004), which hampers convection.

Broadly two main types of mafic-felsic magma interactions have been described: magma mingling, and magma mixing. Magma mingling is the physical interaction between two magmas that are unable to mix thoroughly as a result of high

viscosity (Sparks and Marshall 1986; Frost and Mahood 1987; Sato and Sato 2009) and density contrast (Blake and Fink 1987; Koyaguchi and Blake 1989; Grasset and Albarède 1994) or low degree of mechanical stirring (D'Lemos 1987). Magma mixing is the chemical interaction between two magmas that forms a new "daughter magma" with composition intermediate between the original interacting compositions. Vigorous convective stirring (e.g. Oldenburg et al. 1989) by chaotic advection (e.g. Perugini and Poli 2004; Morgavi et al. 2012) and chemical diffusion (e.g. Watson 1982; Lesher 1994) can lead to the complete blending (or hybridisation) of the two original compositions leaving nearly no vestige of the magmatic "protoliths" (e.g. Humphreys et al. 2010).

Magma mixing involves diffusion of heat and melt components, including volatiles, between the mafic and felsic end-member magmas. Diffusion is a relatively slow process in nature, which cannot lead to large-scale redistribution of chemical components in the absence of convection (Bindeman and Davis 1999). Diffusion in natural silicate melts is a relatively slow process for many of the melt components (except for H_2O and alkalis; Ni and Zhang 2008; Morgan et al. 2008; Acosta-Vigil et al. 2012), and cannot lead to their large-scale redistribution in the absence of convection. Thermal diffusivities are of the order of 10^{-7} m^2/s in H_2O-bearing rhyolitic melts at high temperature (> 800 °C; Romine et al. 2012). This is orders of magnitude larger than chemical diffusivities in silicate melts (Hofmann 1980; Watson 1981; Sparks and Marshall 1986). Volatile diffusion is about 3 orders of magnitude slower than heat diffusion: in hydrous rhyolite melt at 950 °C and 4 kbar (experimental conditions of this study) the diffusivity of H_2O (the most abundant volatile) is about 10^{-10} m^2/s (Ni and Zhang 2008). At these temperature and pressure conditions, the diffusivities of major elements are 1-3 orders of magnitude lower than H_2O

77 diffusivity, with the diffusivities of network-forming species (SiO_2 and $Al_2O_3 \approx 10^{-12}$
78 m^2/s) less than those of network-modifying species (CaO $\approx 10^{-12}$ m^2/s; MgO and K_2O
79 $\approx 10^{-11}$ m^2/s; $Na_2O \approx 10^{-10}$ m^2/s) (van der Laan and Wyllie 1993).

80 Experimental studies designed to better understand the chemistry of magma
81 mixing have tended to focus on the interaction between two liquids of contrasted
82 composition either under anhydrous (Watson 1982; Watson and Jurewicz 1984;
83 Bindeman and Perchuk 1993) or hydrous conditions (Yoder 1973; Johnston and
84 Wyllie 1988; van der Laan and Wyllie 1993). In the latter case both end-member
85 compositions contained identical initial H_2O contents. In a few cases, magma mixing
86 was investigated through dynamic experiments where two or more samples are forced
87 to mix under an applied torque (i.e. mixing and mingling). In these tests the
88 interacting samples display efficient mixing at super-liquidus conditions (Kouchi and
89 Sunagawa 1982; 1985; Morgavi et al. 2012) or, conversely, very poor mixing when
90 one of the two samples is crystal-bearing and, thus, the viscosity contrast between the
91 two systems is large (Laumonier et al. 2014). To date, there are only a few high-
92 temperature and -pressure melting experiments designed to simulate interaction
93 between mafic and felsic magmas, as opposed to liquids. None of these studies has
94 investigated interaction in a realistic scenario where the two samples have different
95 H_2O content and crystallinity prior to interaction, and interact at temperatures
96 consistent with thermal convergence between a hot mafic H_2O-rich magma and a
97 relatively cool hydrous felsic magma. This interaction scenario is the focus of the
98 present experimental study.

99 Our principal motivation is to interpret features of felsic-mafic magma
100 interaction observed in the field. A well-known example is the Tertiary Adamello
101 Massif (Alps, Italy), where dominantly tonalite and subordinate granodiorite plutons

102 are associated with small mafic/ultramafic intrusions, syn-plutonic mafic dykes and
103 sills, and ubiquitous mafic inclusions (Blundy 1989; Blundy and Sparks 1992; John
104 and Blundy 1993). The mafic bodies are texturally and compositionally heterogeneous
105 as a result of variable assimilation of tonalite leading to xenocrystic textures. For
106 example, reactions of quartz phenocrysts from the tonalite with fine-grained dark
107 hornblende-bearing mafic magma produce coronas of green hornblende (Figure 1A).
108 It has also been observed that several mafic and ultramafic rocks can display comb
109 layering at the margins with juxtaposed silicic rocks (e.g. crescumulates layers in
110 Cornone di Blumone, Adamello Massif, Alps, Italy; Ulmer 1986; mafic and
111 ultramafic zonations in Cortland, Duke Island, Ardara and Lac des Iles complexes;
112 Sha 1995). In such a case, elongate grains of hornblende and feldspars are found
113 perpendicular to the interface between felsic and mafic rocks and/or in proximity of
114 fractures in the mingled rock structures (Figure 1B, C). The comb layers are typically
115 asymmetric, and hence display a variety of unidirectional solidification textures
116 (USTs). The presence of hornblende in the gabbroic rock suggests significant H_2O in
117 the original mafic melt (at least 4 wt.% H_2O; e.g. Yoder and Tilley 1962; Holloway
118 and Burnham 1972). Field relationships suggest that the tonalitic crystal mush
119 experienced rheological remobilisation during mafic magma intrusions. Based on
120 such field relationships (Figure 1A), Blundy and Sparks (1992) hypothesise the
121 following scenario: (i) a felsic pluton formed in the crust (< 10 km depth) comprises a
122 crystal mush close to its rheological lock-up point (≥ 0.5 solid fraction) and at or close
123 to H_2O-saturation for the interstitial melt; (ii) this pluton is intruded by a H_2O-rich
124 mafic magma coming from greater depth (< 20 km); (iii) during the subsequent
125 thermal and chemical interaction the two magmas act as a closed-system (i.e. no net
126 loss of volatiles). Interaction might be expected to produce: i) advection of H_2O from

the crystallising mafic magma to the felsic mush; ii) melting and remobilisation of the felsic mush; iii) thermal quenching of the mafic magma. We simulated this interaction scenario experimentally with an H_2O-undersaturated (4 wt.% H_2O in the interstitial melt) dacitic crystal mush (50-80 vol.% quartz crystals) subject to a volatile supply from a nearly H_2O-saturated ($\geq$ 6 wt.% H_2O) andesite magma at 4 kbar and 950 °C. In this contribution we will show that mafic-felsic interactions of the type shown in Figure 1A can also lead to comb layering textures such as that in Figure 1B, C.

Experimental and analytical methods

Experimental strategy

Preparation and synthesis of the starting materials

Preparation of the starting materials was carried out following the approach of Pistone et al. (2012) and Pistone (2012). The two silicate compositions (F = felsic; M = mafic) are synthetic equivalents of natural Adamello bulk compositions JM101 (dacite/tonalite) and JM102 (andesite/diorite) reported by Blundy and Sparks (1992), who used a natural powder of the latter for a series of H_2O-saturated, 1 kbar experiments. However, with respect to the original recipe of JM102 composition, M composition has been modified to generate a more felsic system approaching the composition of F (= JM101). Such a compositional modification of M, which violates the original definition of "mafic composition", represents an experimental compromise that allows constraining the influence of H_2O only and, simultaneously, attenuating the diffusion of other slower melt components driven by limited chemical gradients, which otherwise could have "overwritten" the H_2O signature during interaction experiments. In addition, sample M is crystal-free to maximise H_2O content in the melt during synthesis; however, this differs from the original natural

scenario depicted in Figure 1A where the mafic magma is expected to carry some phenocrysts during the interaction with felsic crystal mushes. Oxides (SiO_2, Al_2O_3, Na_2SiO_3) and hydroxides ($Al(OH)_3$, $K_2Si_3O_7 \bullet 3H_2O$) were used for material preparation; hydroxides provide different amounts of structurally-bound H_2O to F (4 wt.% H_2O) and M (6 wt.% H_2O). The mafic (M) end-member was crystal-free. Crystal-free felsic starting material is designated F0. Aliquots of F were mixed with quartz particles to create additional starting materials of different crystallinity: F50 = 50 vol.% crystals; F60 = 60 vol.%; F70 = 70 vol.%; F80 = 80 vol.%. Quartz crystals (DORSILIT 2500: SiO_2 = 98.90 wt.%; Al_2O_3 = 0.41 wt.%; Fe_2O_3 = 0.02 wt.%; TiO_2 = 0.04 wt.%; Alberto Luisoni AG, Switzerland) were chosen as suspended particles (rough particles with aspect ratios between 1.0 and 3.5) for the preparation of the crystal mushes due to their advantageous properties at the temperature and pressure conditions of our experiments: they do not dissolve appreciably in the felsic melt (JM101 is already at quartz saturation), and inhibit further crystallisation of the residual melt (Pistone et al. 2012). The small amounts of Ti-Fe oxide impurities on the surface of the quartz grains facilitate wetting by the silicate melt during high-temperature and -pressure synthesis (Rutter et al. 2006). Crystals were fired for five hours in a one-atmosphere muffle furnace at 1000 °C to dry the surfaces and to remove any fluid inclusions. Their size was selected by sieving and checked by Malvern Laser Diffraction Grain Sizer at the Limno-Geology Laboratory of ETH-Zurich. The 3D grain size distribution shows a mean value of 68 μm with a sorting of 2.43 and a positive skewness of 0.37 (Pistone et al. 2012). To mix the powders with the appropriate amount of quartz particles, densities of the employed glasses were estimated from the equation of Lange and Carmichael (1987) at room conditions (298 K and 1 bar).

Following the approach of Pistone et al. (2012) and Pistone (2012), the starting material powders were cold-pressed into cylindrical stainless steel canisters (110 mm long, 35 mm inner diameter, 3 mm wall thickness) lined with a thin (25 μm) Mo foil to avoid chemical contamination. Filled canisters were stored at 100 °C to remove any adsorbed humidity and arc-welded shut. Tightness of the seal was checked under vacuum in a water bath and by weighing. The canisters were hot isostatically pressed (HIP) for 24 hours in a large capacity (170 mm in diameter; 500 mm high), industrial, internally-heated pressure vessel (Sinter-HIP-Kompaktanlage; ABRA Fluid AG, Switzerland) at 1.8 kbar and 1200 °C at the Rock Deformation Laboratory of ETH-Zurich. The temperature was nearly constant over the entire volume of the vessel (maximum difference of 18 °C along the length of a sample). A two-step cooling was applied: a rapid decrease of temperature (60 °C/minute) down to the inferred glass transition temperature (when the viscosity is considered equivalent to 10^{12} Pa·s) followed by slow cooling (0.6 °C/minute) to room temperature. The first cooling segment was designed to avoid crystallisation; the second segment produces thermally relaxed glasses (Webb and Dingwell 1990). During cooling the confining pressure decreased slightly with decreasing temperature (38 bar/minute in the first cooling stage; 1 bar/minute in the second one). A total of 6 hydrous samples were produced: M, F0, F50, F60, F70, F80. The weight of the canisters after the HIP run was compared with the initial weights and revealed no significant differences (less than 1 g over 200 g in total) suggesting that no H_2O was lost during synthesis.

Experiments

Cylinders of 3 mm diameter and variable length (Table 1) were cored from the synthesised glasses and polished on the top and bottom surfaces to ensure a perfect

initial contact between the interacting samples. The sandwiched samples were inserted into Au capsules (3-4 mm diameter), which, in turn, were inserted in larger Mo-lined Au capsules (6 mm diameter) filled with Al_2O_3 powder and deionised H_2O (0.1-0.2 ml). Experiments were conducted under oxidised conditions (fO_2 =NNO+1 to +2; see below). In contrast, the starting materials were synthesised at reduced conditions ($\log fO_2$ = -13.08 at 950 °C for $MoMoO_2$ buffer, which is close to IW buffer; O'Neil 1986). The presence of Mo in the double capsule setup slowed down the oxidation of the starting materials by loss of H_2 on the experimental timescale.

Experiments were carried out at the University of Bristol in an end-loaded Boyd and England (1960) type piston cylinder apparatus. Run conditions are given in Table 1. The chosen experimental temperature (950 °C) approximates a mafic magma emplaced at 1100 °C against a felsic host at 800 °C (Blundy and Sparks 1992). Since no latent heat of crystallisation or heat transfer can be experimentally reproduced, experiments simulated that mafic-felsic magma interaction after the interacting systems experienced heat transfer and achieved thermal equilibration. Experiments were carried out in a 19 mm talc-pyrex cell (manufactured by Ceramic Substrates and Components, Isle of Wight, UK), based upon the original design of Kushiro (1976). This type of cell uses a tapered furnace (with 3° taper), which minimises the thermal gradient to < 10 ºC at 1000 ºC over the central 10 mm of the cell (McDade et al. 2002). Based on the CsCl melting reactions the friction correction was 3.6 ±1.0 % at 10 kbar and 1000 °C (McDade et al. 2002) and 20 ±1.0 % at 5 kbar and 950 °C. Also, based on the H_2O solubility conditions of the H_2O-saturated sample M, the effective applied confining pressure to the run products was circa 4 kbar. Temperature was monitored by a D-type ($W_{97}Re_3/W_{75}Re_{25}$) thermocouple connected to a Eurotherm 800 series controller, with no correction for the pressure effect on the electromotive

227 force (Mao and Bell 1971). The hot piston-out technique (Johannes et al. 1971) was
228 used in all experiments. Experiments ran for 24 hours (except for one that lasted for
229 one week; Table 1) and were terminated by turning off the power. Recovered charges
230 were impregnated in epoxy and polished.

231 Two different interaction setups were used in the experiments: i) classic two-
232 layer Setup A with felsic overlying mafic, and ii) "intrusion-type" Setup B with mafic
233 sandwiched between two felsic samples. The two approaches allowed us to simulate
234 the mafic-felsic magma interaction at different mass ratios (mafic-felsic ratio of 1:1 in
235 Setup A, and 1:2 in Setup B; Table 1), and potentially retrieve information on the
236 volatile depletion of the mafic sample during the interaction with one or two felsic
237 samples respectively. To better constrain the textures and chemistry generated during
238 the interaction experiments we also performed simple equilibrium runs on felsic and
239 mafic starting materials. Additionally, after 30 minute dwell time at 1000 °C, four
240 isobaric (4 kbar) cooling experiments from 1000 to 950 °C, with two different cooling
241 rates (slow cooling = 1 °C/minute, and fast cooling = 3.3 °C/second; Table 1), were
242 conducted on crystal-free mafic samples to provide a textural comparison with the
243 microstructures generated in the interaction experiments. A single 48-hour experiment
244 (Table 1) was conducted in cold-seal, externally-heated vessel (with an intrinsic fO_2
245 close to NNO+1; Rouse 2000) to simulate volatile exsolution from the mafic end-
246 member during slow isothermal decompression at low pressure (from 2 to 1 kbar at
247 0.35 bar/minute) and relatively low temperature (870 °C). This test provided a
248 comparison between conditions of volatile-saturation (cold-seal) and volatile-
249 undersaturation (piston cylinder).

250

251 ***Analytical techniques***

252 ***Electron microprobe and scanning electron microscopy***

253 Glasses and minerals from the starting materials and experimental charges
254 were analysed with a CAMECA SX-100 wavelength-dispersive electron probe micro-
255 analyser (EPMA). Glasses were analysed with a 15 kV acceleration voltage, 2-5 nA
256 beam current and 10-20 μm diameter (defocused) beam. Minerals were analysed with
257 a focused (1 μm) 10 nA beam current and an accelerating voltage of 20 kV. Natural
258 and synthetic standards were used for calibration. Table 2 shows compositions of
259 starting glass and minerals in representative experimental charges. Chemical profiles
260 in the glass composition across the run products based on EPMA data are reported in
261 Table 3. H_2O concentrations were estimated by the volatile-by-difference method
262 (Devine et al. 1995; Humphreys et al. 2006) and by SIMS (see below).

263 Using the approach of Saunders et al. (2014) to analysing crystal zoning, lines
264 of quantitative spot analyses to produce quantitative element profiles through quartz
265 crystals and surrounding glass were conducted using a JEOL 8530F field emission
266 gun electron probe micro-analyser (FEG-EPMA). Analyses were carried out with a 10
267 kV acceleration voltage, 1 nA beam current and 1 μm beam diameter. These
268 analytical conditions allowed us to explore potential quartz dissolution in the silicate
269 melt at run conditions. Primary calibrations for FEG-EPMA used the same mixture of
270 synthetic and natural standards as were used with the conventional EPMA.
271 Supplementary material displays chemical data from the lines of quantitative spot
272 analyses in quartz crystals and surrounding silicate glass.

273 Backscattered (BSE) images of the experimental charges were acquired on a
274 Hitachi S-3500N scanning electron microscope (SEM) with 15 to 25 kV accelerating
275 voltage and 1 nA beam current. Images were used to estimate volume fraction and
276 size of the different phases using the Java-based software JMicro-Vision v1.2.7.

277 Characteristic X-ray distribution maps for Si-, Ca- and Fe-Kα, acquired using
278 EPMA and SEM, were used to evaluate the chemical diffusion in the interaction
279 experiments.
280
281 ***Secondary ion mass spectrometry***
282 Glassed starting materials and experimental charges were analysed by
283 secondary ion mass spectrometry (SIMS) for dissolved H_2O and a number of trace
284 elements, using a CAMECA ims-4f ion microprobe at the University of Edinburgh.
285 Au-coated samples were analysed with a 1.5 nA, 10.8 kV $^{16}O^-$ beam focussed to a 10
286 μm spot, with 15 keV net impact energy (i.e. 10.7 keV primary + 4.5 keV). Positive
287 secondary ions were extracted at 4.5 keV with a 75 eV offset and a 40 eV energy
288 window, to minimise molecular ion transmission. Prior to each analysis, a 7 μm^2
289 raster was applied for 2 minutes at the target glass areas in the sample to remove any
290 surface contamination around the edge of the sputter pit. NIST-610 (Hinton 1999),
291 hydrous silica-rich (SiO_2 > 52 wt.%) SISS-48, SISS-51, SISS-59, SISS-60 (H_2O
292 content ranging from 2.48 to 4.91 wt.%; Sisson and Grove 1993), a natural obsidian
293 glass from Lipari (0.72 wt.% H_2O; Humphreys et al. 2006), RB-480 (0.33 wt.% H_2O;
294 Field et al. 2012), RB-497 (0.31 wt.% H_2O; Richard Brooker, unpublished data),
295 SB21, SB23 (10.5 to 10.9 wt.% H_2O; Jenny Riker, unpublished data), and hydrous
296 haplogranitic HGG0, HGG3, HGG4, HGG5 glasses (0 to 5.25 wt.% H_2O; Ardia et al.
297 2008) were used as standards to monitor the H/Si ion yield and background
298 consistency at the start of each day. Ten cycles were counted, corresponding to a
299 counting time of about 10 minutes. In addition to ^1H and ^{30}Si, ^7Li, ^{11}B, ^{26}Mg, ^{42}Ca,
300 ^{47}Ti and ^{54}Fe were measured. The heavier elements were measured to assess the
301 consistency of the major element composition. The background H_2O correction (as

measured on NIST-610) was equivalent to ≤ 0.2 wt.% H_2O. To remove the effects of small variations in beam current, data are presented Si-normalised and corrected using the NIST-610 standard of the GeoReM database (http://georem.mpch-mainz.gwdg.de/). The analytical results are characterised by a low standard deviation (Li = 1.01 %, B = 0.45 %, Mg = 0.93 %, Ca = 1.30 %, Ti = 1.20 %, Fe = 2.25 %). C species was not measured; however, Raman spectra and CO_2-intensity maps of the glasses of the run products (not presented here) did not reveal any presence of CO_2. Table 4 reports the SIMS data.

Results

Run products are labelled with the abbreviations of the two or three separate components added (e.g. M-F0 is a couple made of andesite and crystal-free dacite; F0-M-F0 is a sandwich of andesite between two layers of crystal-free dacite, etc.). We present the microstructural and chemical results of the interaction experiments in three groups, each showing a specific sample-sample interaction:

1) andesite and crystal-free dacite (M-F0 = liquid-liquid interaction in absence of a pre-existing crystallinity in either sample)
2) andesite and crystal-bearing dacite (M-F50 to F80 = liquid-mush interaction)
3) chemically identical samples (M-M and F0-F50) for evaluating crystallisation kinetics in the absence of any difference in melt composition or H_2O content.

Microstructural and chemical results from additional tests simulating the isobaric cooling of a crystal-free andesite, and the interaction between a crystal-free andesite and a crystal-bearing dacite during isothermal decompression (M-F50) are also provided. The microstructural and chemical results of the phase equilibrium runs involving single samples (i.e. no interaction) show limited crystallisation in the

crystal-free felsic sample (< 40 vol.% in F0; Table 1), and no crystallisation in the felsic crystal-bearing samples (see F80 in Table 1). The andesitic samples in the phase equilibrium experiments crystallise with the same phase volumetric proportions observed in the run product M-M (< 50 vol.%; Table 1).

Microstructures

Crystallisation of the crystal-free samples (F0 and M) observed in the phase equilibrium experiments (i.e. in absence of other interacting samples) is driven by a combination of H_2O-undersaturation conditions (i.e. materials were originally synthesised at 2 kbar, corresponding to H_2O-saturation conditions), which render the samples more undercooled, and absence of initial crystal phases (such as quartz in the crystal-bearing materials), which prevents from additional crystallisation during experiments. Thus, the textures of the crystal-free samples observed in the interaction experiments (e.g. M-F0 or M-FX, with FX as crystal mush, which does not crystallise and, thus, remains quartz-saturated at 4 kbar) are the result of two processes: phase equilibrium crystallisation, and H_2O migration from high to low concentration (see below).

Interaction between initially crystal-free andesite and crystal-free dacite

Two runs were conducted to simulate interaction between initially crystal-free andesite (M) and dacite glasses (F0): F0-M and F0-M-F0 (Figure 2A-B). The main difference between the two runs is the experimental duration (24 hours versus 1 week). The longer run (F0-M-F0) generated more extensive crystallisation in both end-members, particularly in the M domain (Table 1). In both run products hornblende and plagioclase form a diktytaxitic texture (with less vesicular

352 groundmass than what observed in natural mafic enclaves) in M (Figures 2A-B).
353 Hornblende crystals in F0 domain in F0-M-F0 are arranged in two ways:
354 perpendicular to the interfaces with M, and, beyond a distance of ~0.5 mm from the
355 interface, with a diktytaxitic arrangement (Figure 2A-B). Along the interaction
356 interfaces of both samples crystal size reduction of hornblende in F0 (from about 200
357 μm length at ~0.5 mm from the interface to 2 μm at the interface) and plagioclase and
358 hornblende in M (from 40 μm at ~0.5 mm from the interface to 1 μm at the interface)
359 are observed (Figures 2A-B and 4A). Fe-Ti oxides (1-5 μm) are ubiquitous in all
360 domains with a mean number density of about 40 crystals per 0.01 mm^2. The largest
361 number density is found at the interface between the two samples (Figures 2A-B and
362 4A). Vesicles are mainly located along the interfaces in F0-M and F0-M-F0; larger
363 vesicles (up to 40 μm diameter) are found in F0 (Figures 2A-B).
364
365 ***Interaction between initially crystal-free andesite and dacitic crystal mush***
366 Four runs were conducted to simulate the interaction of andesite (M) and
367 dacitic crystal mush: F50-M, F60-M-F60, F70-M, and F80-M-F80 (Figure 2C-F). All
368 run products are characterised by the following microstructural features:
369 i) Extensive crystallisation of M, which becomes more evident when Setup B is
370 used (Table 1)
371 ii) Disseminated magnetite in M, whose number density increases towards the
372 interaction interface (Figures 2C-F, 5)
373 iii) A marked decrease in plagioclase and hornblende crystals size towards the
374 interface (from plagioclase length of 250 μm and hornblende length of 190 μm at
375 ~0.5 mm from the interface to 2 μm plagioclase and hornblende size at the
376 interface; Figures 2C-F, 5)

iv) Arrangement of plagioclase and hornblende crystals perpendicular (Figure 2C, E), or at high angle (circa 50-60°; Figure 2D, F), to the interface with F, up to distances of ~0.4 mm from the interaction interface

v) Perpendicular arrangement of hornblende and plagioclase crystals in M and decrease of their size (up to a mean size of 2 μm) to the inner walls of the gold capsule when Setup A is used (Figure 2C-F)

vi) Increase of the local crystal fraction in M domain by about 70% to circa 95% (Figure 2C-F) from ~0.5 mm from the interface towards the interface

vii) Crystal-free, glass layer (30 to 60 μm thick) in F along the interface with M (Figure 2C-F)

viii) Hornblende-rich layer located close to quartz crystal clusters (Figure 2C-F), and hornblende and/or magnetite crystallisation in glassy interstices between quartz crystals in F

ix) Reaction rims on quartz crystals displaying smooth boundaries and crowns of tiny (1 to 3 μm) hornblende microlites (Figure 2C-F)

x) Presence of vesicles in M and along the interface in F, particularly in the glass and/or hornblende-rich layer (Figure 2C-F).

The crystal size reduction of plagioclase and hornblende towards the interface observed in both samples is also evidenced by X-ray maps of Si- and Ca-Kα (Figure 4B). X-ray map of Fe-Kα evidences the large presence of Fe-Ti oxides in the andesite sample, with high number densities in proximity to the interface (Figure 4B). The reported textural features of the andesitic sample during interaction experiments are dramatically different from those observed in the phase equilibrium experiments. Specifically, phase equilibrium textures of M lack in: 1) more extensive crystallisation (> 50 vol.%; Table 1), with an increase in crystallinity (from 50 to 95 vol.%) towards

402 the interaction interface against the felsic, and 2) perpendicular arrangement of
403 minerals, with size reduction towards the interaction interface against the felsic
404 sample.
405
406 ***Interaction between chemically identical samples***
407 The interaction of samples with identical chemical composition and H_2O
408 content was tested with runs F50-F0 and M-M (Figure 2G-H). Run product F50-F0
409 shows extensive hornblende crystallisation in F0 (Table 1), with crystals arranged
410 perpendicular or at high angle (45° to 60°) to the interface (Figure 2G). Hornblendes
411 decrease in size (down to 2 μm) towards the interface (Figure 2G). In F50 quartz
412 microlites (up 10 μm long) lie perpendicular to the interface, without any observable
413 size reduction (Figure 3A). Hornblende and quartz microlites of 2-3 μm size are also
414 found in isolated glass pockets within quartz crystal clusters (Figure 2G).
415 Run product M-M displays disseminated Fe-Ti oxides and vesicles in both
416 sample domains (Figure 2H). The interface between the two samples is vague, but can
417 be discerned by the presence of hornblende crystals in the lower domain. Large
418 plagioclases (up to 100 x 10 μm wide) are found in the core of the two domains (at a
419 distance of ≥ 0.5 mm from the interface). Plagioclases form a loose diktytaxitic
420 texture and their size tends to decrease towards the interface (Figure 2H). Hornblende
421 crystals in the lower domain also decrease in size towards the interface (Figure 2H).
422
423 ***Isobaric cooling of initially crystal-free andesite***
424 Four runs at two different cooling rates (Table 1) were conducted in order to
425 compare textures generated solely by cooling versus those generated by interaction
426 (Figure 3). The fast-cooled (3.3 °C/s) run products show reduction in the size of

hornblende, but not plagioclase, towards the sample periphery (Figure 3A-B). Fe-Ti oxides are absent. The slow-cooled (1 °C/min) run products show extensive crystallisation (glass fraction < 0.06; Table 1), with no clear arrangement of plagioclase and hornblende (Figure 3C-D). Plagioclases are acicular, with constant size (10-15 μm length); hornblende crystals (2-30 μm length) are dendritic. Fe-Ti oxides are diffusely distributed. Similar crystal textures were generated in 1 kbar undercooling experiments on JM102 by Blundy and Sparks (1992; their Fig. 9b).

Interaction during isothermal decompression

One slow-decompression run at low pressure was conducted to simulate the interaction of initially crystal-free andesite and dacitic crystal mush (F50-M [CSV], where CSV means cold seal vessel; see Supplementary Material). Abundant vesicles are observed in both sample domains (Table 1). Vesicles (average diameter 15 μm) in M are concentrated in the core of the sample; larger vesicles (up to 100 μm) are found throughout F50. Overall, there are more vesicles in M than F50, which suggest that gas released from M during crystallisation rose into F50. Gaps between F50 and the capsule walls suggest the production of excess gas during the experiment. In M plagioclase and hornblende crystals lie perpendicular to the interface and, in the lower portion, to the capsule wall. Plagioclase and hornblende crystals decrease in size towards the periphery of M; in particular, tiny (1-2 μm size) plagioclase and hornblende crystals form a thin rim (3 to 10 μm) around M. The interior texture of M is diktytaxitic. In F50 a few hornblende crystals are found in glass-rich regions characterised by a high number density of vesicles. Fe-Ti oxides are observed throughout, often localised around the periphery of F50 (see Supplementary Material).

452 ***Chemistry***

453 ***Interaction between andesite and crystal-free dacite***

454 EPMA and SIMS analyses of run products F0-M and F0-M-F0 provide
455 chemical profiles of essential molar ratios (Figures 5A-B, showing ASI =
456 $Al_2O_3/[CaO+Na_2O+K_2O]$, Al/Si, Al/Na, Al/K, Na/K; Acosta-Vigil et al. 2012), major
457 and trace elements (Supplementary Material) and H_2O across the sample (Figures 6A-
458 B; Tables 3-4). The molar ratio profiles of Al/Si and ASI appear rather constant along
459 the entire domain of both run products, and close to the original values of the starting
460 glasses (Figure 5A-B; Table 2). Particolarly, the Al/Si suggests that Al_2O_3 and SiO_2
461 decrease and increase in the same proportion respectively (Supplementary Material).
462 Conversely, the other molar ratio distributions appear variable (Na/K, and Al/K) or
463 decrease from the andesite to the dacite (Al/K, and Al/Na) in run F0-M (Figure 5A).
464 Neither in the long duration run F0-M-F0 the same molar ratios show a perfectly
465 constant distribution in both dacite domains (Figure 5B). Overall, Al/K and Na/K are
466 lower than the original molar ratios of the starting materials, and Al/Na is higher than
467 the starting Al/Na in both andesite and dacite. These changes of the latter molar ratios
468 are suggestive of an increase of K_2O and Al_2O_3, and a decrease of Na_2O in the
469 residual glass (Supplementary Material) as a consequence of crystallisation of the
470 initially crystal-free dacite and andesite samples. Further details on the major and
471 trace element concentrations in the glass phase of each interacting sample are reported
472 in the Supplementary Material.

473 H_2O contents are similar in the two domains, with limited increase of H_2O in
474 the glass from the dacite (4-5 wt.%) to the andesite (6-7 wt.%; Figure 7A), with H_2O
475 content variations of up to 2 wt.% along the interface (Figure 6A-B). Based on the
476 glass fractions found in the interacting samples (Table 1), the H_2O content in the bulk

477 samples in run F0-M tends to increase from the dacite (2.5-3.1 wt.%) to the andesite
478 (3.3-3.9 wt.%). However, the andesitic sample crystallises largely along the interface
479 (up to circa 80 vol.%) whereas the dacite crystallisation along the interface reaches
480 only about 60 vol.% (Figure 4A). There is no evident H_2O gradient between the two
481 interacting domains after the 24-hour experiment. Conversely, in the longer run F0-
482 M-F0, the H_2O content in the bulk samples clearly changes from the andesite (100
483 vol.% crystalline; Table 1) to the dacite (~70 vol.% residual glass content in both
484 dacitic domains; Table 1). Indeed, all the H_2O is stored in the bulk dacite (2.8-3.5
485 wt.%), suggesting H_2O transfer from the andesite to the dacite. The latter is less
486 crystalline than the equivalent domain in run F0-M (Table 1).
487
488 ***Interaction between andesite and dacitic crystal mush***
489 EPMA and SIMS analysis profiles of run products from interaction
490 experiments generally show a change in chemistry from the dacite to the andesite,
491 particularly for the major oxides such as SiO_2 and Al_2O_3, which show larger
492 variations in the dacite sample portions where the glass is surrounded by quartz
493 crystals (Supplementary Material), suggestive of quartz dissolution at run conditions.
494 Similarly to the crystal-free runs (F0-M and F0-M-F0), runs involving a crystal mush
495 show constant profiles of Al/Si and ASI along the entire run product, and close to the
496 original values of the starting glasses, suggestive of the potential limited chemical
497 change induced by initial crystallisation (as observed in the phase equilibrium
498 experiments) prior to or at the onset of H_2O diffusion during interaction experiments.
499 Similarly to what observed in the crystal-free runs, the distributions of Na/K, Al/Na,
500 and Al/K appear to decrease from the andesite to the dacite domain in all run products
501 with crystallinities < 70 vol.% (Figures C-D). At higher crystallinity the molar ratio

Al/K displays an inverse trend, with a slight decrease from andesite to dacite (Figures 5E-F), suggesting an increase of available Al_2O_3 (melt component with slow diffusion; e.g. Acosta-Vigil et al. 2012) in the residual glass during fast H_2O diffusion. Overall, the values of Na/K, Al/Na, and Al/K are lower than those reported in the starting glasses. For the same reasons reported in the interacting crystal-free samples above, the decrease of these molar ratio values are suggestive of an increase of K_2O and Al_2O_3, and a decrease of Na_2O in the residual glass (Supplementary Material) as a consequence of the H_2O diffusion-induced crystallisation of the andesite and H_2O diffusion-induced quartz dissolution in the dacite. Also, the same molar ratios of the run products with Setup B result lower by 20% than those observed in the run products with Setup A, suggestive of the different impact of the mafic-felsic mass ratio on Al_2O_3 and alkalis contents in the residual glass in the mafic end-member. Further details on the major and trace element concentrations in the glass phase of each interacting sample are reported in the Supplementary Material.

H_2O contents in the glass increase from the dacite (5-6 wt.% H_2O) to the andesite (7-8 wt.%) (Figure 6C-F). In the dacite H_2O contents are higher in proximity to the interface, and lower in glass pockets within quartz crystal clusters (see SIMS analysis spots in the Supplementary Material). More interestingly, H_2O contents in the bulk samples change dramatically from the andesite to the dacite, particularly along the interface (< 1 mm distance from the interface; Figure 6C-F) where the andesite is largely crystalline (> 90 vol.%), whereas the dacite is glassy or displays limited hornblende crystallisation (< 7 vol.%; Table 1) around the quartz crystals (Figure 4B). Bulk H_2O contents in the two bulk domains varies from < 0.7-0.8 wt.% in the upper portion of the andesite (< 1 mm from the interface) to 1.1-2.9 wt.% in the dacite. The greater the crystal content in the dacitic mush, the higher the H_2O content in the glass

(Figure 6C-E) and the lower the H_2O content in the bulk dacite. Run F80-M-F80 represents an exception since both H_2O contents in the glass (3-4 wt.%) and in the bulk dacite (0.36-0.63 wt.%) are lower than in the other run products (Figure 6C-F), suggestive of the combination of large crystal content in the mush and dissolution of quartz during the experiment.

Interaction between chemically identical samples

As expected, SIMS analysis of run products involving interaction between chemically identical samples show no evident change in major oxides, trace elements and H_2O contents in the residual glass from one sample domain to the other (Table 4; Supplementary Material). Thus the chemical features described in preceding sections result from interaction, rather than any artefact of the experimental design.

Discussion

The change of the liquidus temperature as a function of H_2O content

Microstructural and chemical changes that occur during interaction experiments are most readily interpreted in terms of the changes in liquidus temperature (T_L) that arise when magmas of contrasted chemistry are juxtaposed. Because T_L is strongly reduced by the addition of H_2O, up to the point of saturation, so the flux of H_2O from one domain to another has the greatest influence on T_L. In our experiments the values of local T_L were computed using the model of Makhluf et al. (2014) using the EPMA data of residual silicic glass (Table 3), including SIMS-based H_2O content (Table 4), in order to estimate the local H_2O contents in the bulk rock based on the local glass volume fractions (see Supplementary Material). In our experiments there is an H_2O gradient between the two interacting samples (andesite

melt = 6 wt.% H_2O versus dacite melt = 4 wt.% H_2O; Table 2). The initial T_L results different in each starting material: the andesite has T_L = 816 ±1 °C (Figure 8), and the dacite displays a decrease of the initial T_L with increasing crystallinity in the felsic mush, ranging from T_L = 923 ±1 °C at 3.69 ±0.02 wt.% H_2O in initial crystal-free glass to 1109 ±1 °C at 0.74 ±0.02 wt.% H_2O in the most crystal-rich sample (Figures 6, 7). Given the chemical similarity of the interacting compositions (Table 2), the lower andesite T_L than the dacite T_L is due to the initial high H_2O content in the andesite (Table 2). The change of T_L is clearly evident in both interacting domains: T_L drops in the dacite, to below the experimental temperature at some locations, and increases markedly in the crystallising andesite (Figure 7). Such changes in T_L become more pronounced with increasing crystallinity in the felsic mush and with decreasing the mafic/felsic mass ratio (Figure 7).

One of the primary consequences of melt dehydration is isothermal crystallisation, first recognised by Tuttle and Bowen (1958) and invoked as a cause of crystallisation in hydrous magma by Blundy and Cashman (2001). This behaviour arises because, compared to other compositional parameters, H_2O has a disproportionate effect on the T_L of a magma (Yoder et al. 1957; Burnham and Jahns 1962; Merrill and Wyllie 1975). Thus, H_2O loss from any hydrous magma, whether by degassing or diffusion, will drive large increase in T_L leading to effective undercooling and consequent crystallisation.

During interaction of mafic and felsic magmas a number of simultaneous chemical and physical changes occur. These may drive crystallisation or melting, depending on the relationship between the interaction temperature and the T_L of each domain. We will express the change in T_L as normalised temperature: $T_{experimental}$ / T_L, both of which are known from our experiments (Figure 8A). In the case of

577 undercooling, crystallisation will result, but the extent to which nucleation, giving rise
578 to many small crystals, is favoured over growth, giving rise to large crystals, depends
579 on the magnitude of the undercooling. In general, larger values of undercooling
580 favour crystal nucleation, while small values of undercooling favour crystal growth
581 (Figure 8A). Crystallisation serves to reduce T_L and hence reduce undercooling,
582 eventually reaching zero at the point of chemical equilibrium. Where the interaction
583 temperature is greater than T_L, melting will result (Figure 8A). We can better
584 understand this complex interplay of diffusion of heat, diffusion of mass, and
585 crystallisation kinetics in terms of three end-member scenarios.

586 First, consider juxtaposition of two crystal-free, anhydrous melts of different
587 composition at two different temperatures. In this example only heat crosses the
588 interface between the two domains (Figure 8B). The contact temperature at the
589 interface ($T_{interface}$) will lie between the T_L of the felsic ($T_{L(felsic)}$) and mafic ($T_{L(mafic)}$)
590 domains. The initial undercooling that occurs in the mafic domain is $\Delta T = T_{interface}$ -
591 $T_{L(mafic)}$ and will be greatest (i.e. most negative) at the interface. Thus, crystal
592 nucleation is favoured close to the interface and a so-called "chilled margin" results.
593 A crystallisation front propagates away from the interface into the mafic domain, with
594 progressively smaller ΔT and consequently larger, but fewer crystals. In the felsic
595 domain $\Delta T = T_{interface}$ - $T_{L(felsic)}$ may be positive at the interface. In that case a fully
596 molten layer may result. Elsewhere in the felsic domain some evidence of partial
597 melting will be apparent, although temperatures are unlikely to be sufficient to cause
598 complete melting (Figure 8B).

599 Next, consider the case where two melts at different temperature are brought
600 into contact but the mafic magma is H_2O-saturated and the felsic magma is
601 anhydrous. In this case both heat and H_2O will pass from the mafic to the felsic

602 domain, complicating the textural consequences of interaction (Figure 8C). As before,
603 thermal undercooling of the mafic domain at the interface will lead to crystallisation.
604 However the loss of H_2O from the mafic domain to the felsic domain will drive up
605 $T_{L(mafic)}$, further increasing ΔT and leading to more pronounced nucleation. We call
606 this "chemical undercooling". The chemical and thermal undercooling fronts will
607 propagate away from the interface at rates controlled by the relative diffusivities of
608 H_2O and heat. The relative rates of migration will determine the extent to which
609 nucleation is favoured over growth and vice versa. Although heat diffuses three orders
610 of magnitude faster than H_2O, the effect of reducing the temperature on ΔT is much
611 less than the effect of dehydration on T_L. An inverse consequence can be expected in
612 the felsic domain, where both heat and H_2O are being supplied. Both of these will
613 serve to reduce (or eliminate) the amount of undercooling, and increase the likelihood
614 of a crystal-free melt layer forming at the interface (Figure 8C).

615 Last, consider the case of isothermal interaction between an H_2O-saturated
616 mafic magma and a dry (or H_2O-undersaturated) felsic magma, such as that simulated
617 by our experiments. In this case only H_2O passes from mafic to felsic domains and
618 any undercooling is entirely chemical in origin (Figure 8D). As H_2O is lost to the
619 felsic domain, a front of increasing T_L will propagate into the mafic domain.
620 Crystallisation will tend to follow this front. Depending on the evolution of ΔT with
621 time, i.e. the relative rates of H_2O loss (increasing ΔT) and crystallisation (reducing
622 ΔT), the migration of the crystallisation front may be dominated either by nucleation
623 or growth (Figure 8D).

624 The above discussion makes a distinction between thermal undercooling, due
625 to heat loss, and chemical undercooling due to the loss of H_2O (or any other
626 component that has a profound effect on T_L). Our experiments were designed to look

627 at both chemical undercooling (interaction experiments) and thermal undercooling
628 (cooling-rate experiments) and to compare the results.

629 In our experiments diffusion of chemical components other than H_2O plays a
630 minor role since the interacting compositions are chemically relatively similar
631 (compare F and M composition reported in Table 2). In contrast to previous
632 experiments on magma mixing between hydrous compositions (Johnston and Wyllie
633 1988; van der Laan and Wyllie 1993), no "uphill diffusion" of alkalis is noticed in our
634 tests (Figure 5C-F), likely because of a lack of large K and Na gradients between F
635 and M (Table 3). Additionally, since H_2O diffusivity between interacting silicic melts
636 is much greater than the diffusivities of major elements (van der Laan and Wyllie
637 1993), at identical temperature and pressure conditions the flux of H_2O from andesite
638 to dacite strongly affects the diffusivities of the major chemical elements, including
639 the "fast" alkalis (Acosta-Vigil et al. 2005). As already observed by van der Laan and
640 Wyllie (1993), both K_2O and Na_2O are uniformly distributed through the entire length
641 of the capsule within 44 hours, suggesting transient two-liquid equilibrium
642 partitioning when large H_2O contents (5 wt.%) are present. In our experiments the
643 presence of > 5 wt.% H_2O in the silicic melt (Figure 6C-F) should allow a faster
644 uniform distribution of alkalis within 24 hours (Table 1); however, the molar ratio
645 profiles (i.e. Al/K, Al/Na, and Na/K; Figure 5) do not show perfectly constant
646 distribution profiles of alkalis throughout the glass phase (i.e. no field diffusion of
647 alkalis; Acosta-Vigil et al. 2002; 2006; 2012). This could mean that alkalis, in
648 presence of limited chemical gradients ($\Delta Na_2O_{mafic\text{-}felsic}$ < 0.25 wt.% and $\Delta K_2O_{mafic\text{-}}$
649 $_{felsic}$ < 0.04 wt.%; Table 2) except for H_2O (> 2 wt.%, including that the H_2O gradient
650 could be higher if the initial crystallisation of the mafic sample at equilibrium
651 conditions is considered; Table 1), are characterised by a relatively "slow" diffusion

652 with respect to H_2O within the timescale of our experiments (24 hours). Only after
653 sufficient long timescale (1 week; see run product F0-M-F0 in Figure 5B) during
654 which H_2O was uniformly distributed in both interacting samples (Figure 6B), alkalis
655 appear constantly distributed throughout the glass of the run products. In conclusion,
656 we are confident that the microstructural features generated in our experiments
657 received negligible contribution from diffusion of species other than H_2O, which
658 migrated from the mafic to the felsic end-member and the consequent change in T_L of
659 the interacting magmas (Figures 6C-F, 7C-F).
660
661 ***Unidirectional solidification textures driven by chemical undercooling***
662 The microstructural and chemical results of our experiments display a number
663 of interesting features that can be related to the changes in T_L that result from the flux
664 of H_2O from initially crystal-free mafic domain into the felsic mush. These include:
665 i) Reduction of crystal size in the mafic end-member towards to the interface of the
666 two samples (Figure 2C-F)
667 ii) Hornblende and plagioclase layering in the mafic end-member in which crystals
668 grow from the interface towards the interior of the mafic melt (Figure 2C-F)
669 iii) Formation of a melt-rich "hybrid front" with hornblende-rich coronas around
670 quartz crystals (Figure 2C-F)
671 As noted above, the "chilled margins" generated in the andesite during the isothermal
672 experiments are not a consequence of thermal quenching, but they rather represent a
673 chemical quenching due to H_2O migration from the mafic to the felsic end-member at
674 constant temperature and pressure. The linear arrangement of plagioclase and
675 hornblende crystals in the andesite and their size reduction towards the interaction
676 interface between dacite and andesite (Figures 2C-F, 4) is reminiscent of a number of

677 natural textures including “Willow Lake-type” layering (Poldervaart and Taubenek
678 1959), combed texture (Loomis 1963), comb layering (Moore and Lockwood 1973;
679 Lofgren and Donaldson 1975; Donaldson 1977; Lowenstern and Sinclair 1996;
680 Sinclair 2007), Stockscheider texture (Jackson and Power 1995; Breiter et al. 2005),
681 line rock texture (Webber et al. 1997; Nabelek et al. 2010) or, more generally,
682 unidirectional solidification texture (UST; Kormilitsyn and Manuilova 1957; Shannon
683 et al. 1982; Balashov et al. 2000; Breiter 2002; Hönig et al. 2010). USTs often involve
684 an alternation of coarse and fine crystals, leading some workers to invoke processes of
685 crystal growth and dissolution to operate in tandem. For example, comb layering
686 textures studied in pegmatitic systems (e.g. aplite-pegmatite transition; Webber et al.
687 1999; Baker and Freda 1999; 2001; London 2005; 2009) and orbicular rocks (Leveson
688 1966; Moore and Lockwood 1973; Ort 1992; Sylvester 2011), were explained as a
689 consequence of an Ostwald ripening process, where smaller crystals become unstable
690 relative to larger crystals of the same mineral composition (e.g. Boudreau and
691 McBirney 1997).

692 Our experiments suggest, alternatively, that USTs can be generated
693 isothermally simply due to volatile loss and the consequent change in ΔT, which
694 drives melts locally towards nucleation-dominated and growth-dominated regimes
695 (Figures 8A). In our experiments the loss of H_2O is a result of the H_2O-saturated
696 nature of the mafic melt and the H_2O-undersaturated nature of the felsic melt at run
697 conditions. The loss of H_2O from mafic to felsic domains drives undercooling in the
698 former, promoting crystal growth. The tendency of crystals to grow perpendicular to
699 the interface between the two domains suggests that following initial nucleation close
700 to the interface, the migration of the undercooling front away from the interface
701 serves to maintain ΔT at an optimum value for growth (Figure 8A). Although our

experiments are isothermal and isobaric, they simulate many situations in nature where magmatic H_2O loss occurs. This could be, for example, when hydrous magma is exposed to fractures whereupon the pressure drops driving fluids outwards. Such features have been widely invoked in ore-forming or pegmatitic systems and may occur repeatedly if the magma keeps undergoing failure and pressure drop. In a magma the development of fractures requires a relatively high crystal content and/or a high strain-rate. More generally, we would anticipate that any process that leads to pressure drops that are transient on the same timescales as H_2O diffusion in silicate melts would be capable of generating USTs. Magma mixing between H_2O-rich and H_2O-poor magmas, as simulated in our experiments, is just one such scenario. Our proposal is consistent with explanations of rhythmic comb-quartz and/or comb-feldspar layers developed in aplite granite groundmass attributed to abrupt adiabatic drop in pressure (due to fracturing; Shannon et al. 1982) promoting gas escape ("swinging eutectic" of Balashov et al. 2000). Thus, cooling is not a pre-requisite to UST formation. Rather it is undercooling resulting from H_2O exsolution from a crystallising melt. In general, USTs are generated at supersaturated boundaries and during rapid and repeated undercooling of the magmatic system (Fenn 1977; Webber et al. 1997; Nabelek et al. 2010) induced by fluid release (London 1992).

Interaction experiments involving dacitic crystal mush show that the presence of quartz crystals also plays an important role in driving textural evolution. As the felsic sample equilibrates at the experimental conditions, the quartz crystals begin to dissolve supplying SiO_2 to the surrounding melt (see Supplementary Material). The consequent SiO_2 content increase in the residual melt increases the local volatile solubility (Johannes and Holtz 1996) and, thus, attracts more H_2O from the adjacent andesite. This might explain the formation of hornblende in proximity to quartz

clusters or around single quartz crystals (Figures 2C-F, 5B) where the silicate melt contains up to 6 wt.% H_2O (see H_2O profiles in Figure 6C-F; see analysis spot locations in Supplementary Material). H_2O destabilises plagioclase and leads to hornblende crystallisation (Yoder and Tilley 1962; Holloway and Burnham 1972; Anderson 1980). At even larger H_2O in the residual dacite melt all crystallisation is suppressed and glassy rims or interstices result (see H_2O profiles in Figure 6C-F; see analysis spot locations in Supplementary Material).

Conclusions

The results of our experiments designed to explore magma mixing in nature show a number of interesting microstructural features. The "quench textures" or "chilled margins" found in our run products arise for enhanced crystal nucleation rates driven by chemical diffusion (H_2O), rather than rapid cooling, showing that mafic-felsic interactions found in the field may not be simply thermal in origin. The interface, across which chemical diffusion occurs, may play a key role in textural and chemical development. Specifically, we have generated unidirectional solidification textures (USTs), or comb layering, in which crystals nucleate at the mafic-felsic interface and grow into the mafic end-member. Comb layering is not a common microstructural feature of mafic enclaves. However, it can be considered as a specific category of "chemical chilling" where crystals do not decrease only in size towards an interaction interface (against another magma composition and or a wall rock, as observed in numerous field studies; e.g. Frost and Mahood 1987; Gourgaud and Villemant 1992), but they are also arranged perpendicularly to the interface. Our experimental results indicate that USTs can be used as a textural criterion to indicate the direction of volatile transfer. This has been observed in several mafic and

752 ultramafic rocks displaying comb layering at the margins with juxtaposed silicic rocks
753 (Sha 1995). Mafic rocks in contact with felsic rocks show a decrease in the volumetric
754 proportion of hydrous minerals such as hornblende, biotite as well as apatite and
755 titanite towards the centres of the mafic complexes. Furthermore, in the dehydration
756 zones of mafic rocks, acicular apatite crystals are typically abundant, indicative of
757 strong undercooling (e.g. Wyllie et al. 1962). Our experiments demonstrate the ability
758 of chemical quenching driven by H_2O-loss to generate a diversity of textures found in
759 hydrous magmatic systems, including those associated with ore deposits.
760
761 **Acknowledgments**
762 SNSF Grant EPM-PBEZP2_14922 and ERC Advanced Grant CRITMAG
763 supported this research. We acknowledge: K. Stuart and B. Buse for supporting
764 during the EPMA, FEG-EPMA, and SEM analyses (University of Bristol); R. Hinton
765 for assisting during the SIMS analyses (EIMF, University of Edinburgh); C. Clapham
766 and D. Hawley for technical support (University of Bristol); J. Riker for providing
767 high H_2O content silicate glasses as standards for SIMS analysis; Alberto Luisoni AG
768 (Switzerland), Nabaltec AG (Germany), and B. Tripoli (ETH-Zurich) for supplying
769 quartz crystals, APYRAL 60CD, and wollastonite used in the starting materials; O.
770 Müntener, A. Acosta-Vigil, and an anonymous reviewer for their helpful comments
771 on an earlier version of the manuscript.
772
773 **References**
774 Acosta-Vigil A, London D, Dewers TA, Morgan GB VI (2002) Dissolution of corundum and
775 andalusite in H_2O-saturated haplogranitic melts at 800 °C and 200 MPa: constraints on diffusivities and
776 the generation of peraluminous melts. J Petrol 43:1885-1908
777 Acosta-Vigil A, London D, Morgan GB VI (2005) Contrasting interactions of sodium and potassium

778 with H_2O in haplogranitic liquids and glasses at 200 MPa from hydration–diffusion experiments.
779 Contrib Mineral Petrol 149:276-287
780 Acosta-Vigil A, London D, Morgan GB VI, Dewers TA (2006) Dissolution of quartz, albite and
781 orthoclase in H_2O-saturated haplogranitic melts at 800 °C and 200 MPa: diffusive transport properties
782 of granitic melts at crustal anatectic conditions. J Petrol 43:1885-1908
783 Acosta-Vigil A, London D, Morgan GB VI (2012) Chemical diffusion of major components in granitic
784 liquids: implications for the rates of homogenization of crustal melts. Lithos 153:308-323
785 Anderson JL (1980) Mineral equilibria and crystallization conditions in the late Precambrian Wolf
786 River rapakivi massif, Wisconsin. Am J Sci 280:289-332
787 Ardia P, Giordano D, Schmidt MW (2008) A model for the viscosity of rhyolite as a function of H_2O-
788 content and pressure: a calibration based on centrifuge piston cylinder experiments. Geochim
789 Cosmochim Acta 72:6013-6123
790 Bachmann O, Bergantz GW (2004) On the origin of crystal-poor rhyolites: extracted from batholitic
791 crystal mushes. J Petrol 45:1565-1582
792 Balashov VN, Zaraisky GP, Seltmann R (2000) Fluid-magmatic interaction and oscillation phenomena
793 during granite melt crystallization with water-fluoride fluid gain-loss. Petrologiya 8:563–585
794 Baker DR, Freda C (1999) Ising models of undercooled binary system crystallization: comparison with
795 experimental and pegmatite textures. Am Mineral 84:725-732
796 Baker DR, Freda C (2001) Eutectic crystallization in the undercooled orthoclase-quartz-H_2O system:
797 experiments and simulations. Eur J Mineral 13:453–466
798 Bindeman IN, Perchuk LL (1993) Experimental studies of magma mixing at high pressures. Int Geol
799 Rev 35:721-733
800 Bindeman IN, Davis AM (1999) Convection and redistribution of alkalis and trace elements during the
801 mingling of basaltic and rhyolitic melts. Petrol 7:91-101
802 Blake S, Fink JH (1987) The dynamics of magma withdrawal from a density stratified dyke Earth
803 Planet. Sci Lett 85:516-524
804 Blundy JD (1989) The geology of the southern Adamello Massif, Italy. Dissertation, University of
805 Cambridge
806 Blundy JD, Sparks RSJ (1992) Petrogenesis of mafic inclusions in granitoids of the Adamello Massif,
807 Italy. J Petrol 33:1039-1104

808 Blundy JD, Cashman K (2001) Magma ascent and crystallization at Mount St. Helens, 1980-1986.
809 Contrib Mineral Petrol 140:631-650
810 Blundy JD, Mavrogenes J, Tattitch B, Sparks RSJ, Gilmer A (2015) Generation of porphyry copper
811 deposits by gas–brine reaction in volcanic arcs. Nature Geosci. 8:235-240
812 Boudreau AE, McBirney AR (1997) The Skaergaard Layered Series. Part III. Non-dynamic Layering. J
813 Petrol 38:1003-1020
814 Boyd FR, England JL (1960) Apparatus for phase equilibrium measurements at pressures of up to 50
815 kbars and temperatures to 1750ºC. J Geophys Res 65:741-748
816 Breiter K (2002) From explosive breccia to unidirectional solidification textures: magmatic evolution
817 of a phosphorus- and fluorine-rich granite system (Podlesí, Krušné hory Mts., Czech Republic). Bull
818 Czech Geol Survey 77:67–92
819 Breiter K., Mqller A, Leichmann J, Gabasˇova' A (2005) Textural and chemical evolution of a
820 fractionated granitic system: the Podlesı´ stock, Czech Republic. Lithos 80:323-345
821 Bunsen R. (1851) Ueber die prozesse der vulkanishen Gesteinsbildungen Islands. Annalen der Physik
822 (Leipzig) 83:197–272
823 Burnham CW, Jahns RH (1962) A method for determining the solubility of water in silicate melts. Am
824 J Sci 260:721-745
825 Cervantes P, Wallace P (2003) Role of H_2O in subduction-zone magmatism: newinsights from melt
826 inclusions in high-Mg basalts from central Mexico. Geology 31:235-238
827 Czuppon G, Lukacs R, Harangi S, Mason PRD, Ntaflos T (2012) Mixing of crystal mushes and melts
828 in the genesis of the Bogacs ignimbrite suite, northern Hungary; an integrated geochemical
829 investigation of mineral phases and glasses. Lithos Oslo 148:71-85.
830 D'Lemos RS (1987) Relantionships between the Cobo Granite and the Bordeaux Diorite Complex,
831 Guernsey. PhD Dissertation, University of Bristol
832 de Saint Blanquait M, Habert G, Horsman E, Morgan SS, Tikoff B, Launeau P, Gleizes G (2006)
833 Mechanisms and duration of non-tectonically assisted magma emplacement in the upper crust: the
834 Black Mesa pluton, Henry Mountains, Utah. Tectonophys 428:1-31
835 Devine JD, Gardner JE, Brack HP, Layne GD, Rutherford MJ (1995) Comparison of microanalytical
836 methods for estimating H_2O contents of silicic volcanic glasses. Am Mineral 80:319-328
837 Donaldson CH (1977) Laboratory duplication of comb layering in the Rhum pluton. Mineral. Magaz.

838 41:323-336
839 Fedkin A, Seltmann R, Bezmen N, Zaraisky G (2002) Experimental testing of line rocks in Li-F
840 granites: evidence from superliquidus experiments with F and P added. Bull Czech Geol Survey
841 77:113-125
842 Fenn PM (1977) The nucleation and growth of alkali feldspars from hydrous melts. Can Mineral
843 15:135-161.
844 Field L, Blundy JD, Brooker RA, Wright T, Yirgu G (2012) Magma storage conditions beneath
845 Dabbahu Volcano (Ethiopia) constrained by petrology, seismicity and satellite geodesy. Bull Volcanol
846 74:981-1004
847 Frost TP, Mahood GA (1987) Field, chemical, and physical constraints on mafic-felsic magma
848 interaction in the Lamarck Granodiorite, Sierra Nevada, California. Geol Soc of Am Bull 99:272-291
849 Gourgaud A, Villemant B (1992) Evolution of magma mixing in an alkaline suite: the Grande Cascade
850 sequence (Monts-Dore, French Massif Central). Geochemical modeling. J Volcanol Geotherm Res
851 52:255-275
852 Grasset O, Albarade F, Hybridization of mingling magmas with different densities. Earth Planet Sci
853 Lett 121:327-332
854 Hattori KH, Keith JD (2001) Contribution of mafic melt to porphyry copper mineralization: evidence from
855 Mount Pinatubo, Philippines, and Bingham deposit, Utah. Mineral. Deposita 36:799-806
856 Hinton RW (1990) Ion microprobe trace-element analysis of silicates.measurement of multi-element
857 glasses. Chem Geol 83:11-25
858 Hofmann AW (1980) Diffusion in natural silicate melts: A critical review. In: Hargraves RB (ed),
859 Physics of magmatic processes. Princeton University Press, pp 385-417
860 Holloway J.R., Burnham CW (1972) Melting relations of basalt with equilibrium water pressure less
861 than total pressure. J Petrol 13:1-29
862 Hönig S, Leichmann J, Novak M (2010) Unidirectional solidification textures and garnet layering in Y-
863 enriched garnet-bearing aplite–pegmatites in the Cadomian Brno Batholith, Czech Republic. J Geosci
864 55:113-129
865 Hort M (1998) Abrupt change in magma liquidus temperature because of volatile loss or magma
866 mixing: effects on nucleation, crystal growth and thermal history of the magma. J Petrol 39:1063-1076
867 Humphreys MCS, Kearns SL, Blundy JD (2006), SIMS investigation of electron-beam damage to

hydrous, rhyolitic glasses: implications for melt inclusion analysis. Am Mineral 91:667-679

Humphreys MCS, Edmonds M, Christopher T, Hards V (2010) Magma hybridisation and diffusive exchange recorded in heterogeneous glasses from Soufrière Hills Volcano, Montserrat. Geophys Res Lett 37:L00E06

Jackson G.E.A., Power G.M. (1995) Columnar, branching and curved feldspar growth in the St Michael's Mount Granite, Cornwall. Proc. Ussher Soc 8:363-367

Johannes WJ, Bell PM, Mao HK, Boettcher AL, Chipman DW, Hays JF, Newton RC, Seifert F (1971) An interlaboratory comparison of piston-cylinder pressure calibration using the albite breakdown reaction. Contrib Mineral Petrol 32:24-38

Johannes WJ, Holtz F (1996) Petrogenesis and Experimental Petrology of Granitic Rocks. Springer, pp. 335

John BE, Blundy JD (1993) Emplacement-related deformation of granitoidmagmas, southern Adamello Massif, Italy. Geol Soc Am Bull 105:1517-1541

Johnston AD, Wyllie PJ (1988) Interaction of granitic and basic magmas: experimental observations on contamination processes at 10 kbar with H_2O. Contrib Mineral Petrol 98:352-362

Kormilitsyn VS, Manuilova MM (1957) Rhythmic banded quartz porphyry, Bugdai Mountain, southeast Transbaykal region. Zapiski Vsesoyouz Mineral Obsch 86:355-364.

Kouchi A, Sunagawa I (1982) Experimental study of mixing of basaltic and dacitic magmas, Sci Rep Tohoku University 15:163-175

Kouchi A, Sunagawa I (1985) A model for mixing basaltic and dacitic magmas as deduced from experimental data. Contrib Mineral Petrol 89:17-23

Koyaguchi T, Blake S (1989) The dynamics of magma mixing in a rising magma batch. Bull Volcanol 52:127-137

Lange RA, Carmichael ISE (1987) Densities of Na_2O-K_2O-CaO-MgO-FeO-Fe_2O_3-Al_2O_3-TiO_2-SiO_2 liquids: new measurements and derived partial molar properties. Geochim Cosmochim Acta 51:2931-2946

Laumonier M, Scaillet B., Arbaret L., Champallier R (2014) Experimental simulation of magma mixing at high pressure. Lithos 196:281-300

Lesher CE (1994) Kinetics of Sr and Nd exchange in silicate liquids: Theory, experiments, and applications to uphill diffusion, isotopic equilibration, and irreversible mixing of magmas. J Geophys

898 Res 99:9585-9604
899 Leuthold J, Müntener O, Baumgartner LP, Putlitz B, Ovtcharova M, Schaltegger U (2012) Time
900 resolved construction of a bimodal laccolith (Torres del Paine, Patagonia). Earth Planet Sci Lett 325-
901 326:85-92
902 Leveson DJ (1966) Orbicular rocks: a review. Geol Soc Am Bull 77:409-426
903 Lofgren GE, Donaldson CH (1975) Curved branching crystals and differentiation in comb-layered
904 rocks. Contrib Mineral Petrol 49:309-319
905 London D (1992) The application of experimental petrology to the genesis and crystallization of
906 granitic pegmatites. Can Mineral 30:499-540
907 London D (2005) Granitic pegmatites: an assessment of current concepts and directions for the future.
908 Lithos 80:271-303
909 London D (2008) Pegmatites. Can Mineral Sp Publ 10, pp. 347
910 Loomis AA (1963) Noritic anorthositc bodies in the Sierra Nevada Batholith. Mineral Soc Am Spec
911 Paper 1:62-68
912 Lowenstern JB, Sinclair WD (1996) Exsolved magmatic fluid and its role in the formation of comb-
913 layered quartz at the Cretaceous Logtung W-Mo deposit, Yukon Territory, Canada. Trans Royal Soc
914 Edinburgh: Earth Sciences 87:291-303
915 Makhluf AR, Newton RC, Manning CE, Experimental determination of liquidus H_2O contents of
916 simple granites at deep crustal conditions. http://adsabs.harvard.edu/abs/2014AGUFM.V51C4778M
917 Mao HK, Bell PM (1971) Behavior of thermo-couples in the single-stage piston-cylinder apparatus.
918 Carnegie Inst Ilash Year Book 691:207-216
919 McDade P, Wood BJ, van Westrenen W, Brooker RA, Gudmudsson G, Soulard H, Najorka J, Blundy
920 JD (2002) Pressure corrections for a selection of piston-cylinder cell assemblies, Mineral Magaz
921 66:1021–1028
922 Merrill RB, Wyllie PJ (1975) Kaersutite and kaersutite eclogite from Kakanui, New Zealand: water
923 excess and water deficient melting to 30 kilobars. Geol Soc Am Bull 86:555-570
924 Moore JG, Lockwood JP (1973) Origin of comb layering and orbicular structure, Sierra Nevada
925 Batholith, California. Geol Soc Am Bull 84:1-20
926 Morgan GB VI, Acosta-Vigil A, London D (2008) Diffusive equilibration between hydrous
927 metaluminous-peraluminous haplogranite liquid couples at 200 MPa (H_2O) and alkali transport in

928 granitic liquids. Contrib Mineral Petrol 155:257-269
929 Morgavi D, et al. (2012) Interactions between rhyolitic and basaltic melts unraveled by chaotic mixing
930 experiments. Chem Geol doi10.1016/j.chemgeo.2012.10.003
931 Murphy MD, Sparks RSJ, Barclay J, Carroll MR, Brewer TS (2000) Remobilization of andesite magma
932 by intrusion of mafic magma at the Soufriere Hills Volcano, Montserrat, West Indies. J Petrol 41:21-42
933 Nabelek PI, Whittington AG, Sirbescu M-LC (2010) The role of H_2O in rapid emplacement and
934 crystallization of granite pegmatites: resolving the paradox of large crystals in highly undercooled
935 melts. Contrib Mineral Petrol 160:313-325
936 Ni H, Zhang Y (2008) H_2O diffusion models in rhyolitic melt with new high pressure data. Chem Geol
937 250:68-78
938 Oldenburg CM, Spera FJ, Yuen DA, Sewell G (1989) Dynamic mixing in magma bodies: theory,
939 simulations and implications. J Geophys Res 94:9215-9236
940 O'Neil HSC (1986) Mo-MoO2 (MOM) oxygen buffer and the free energy of formation of MoO2. Am
941 Mineral 71:1007-1010
942 Ort MH (1992) Orbicular volcanic rocks of Cerro Panizos: their origin and implications for orb
943 formation. Geol Soc Am Bull 84:1-20
944 Perugini D, Poli G (2004) Analysis and numerical simulation of chaotic advection and chemical
945 diffusion during magma mixing: petrological implications. Lithos 78:43-66
946 Plank T, Kelley KA, Zimmer MM, Hauri EH, Wallace PJ (2013) Why do mafic arc magmas contain
947 ~4 wt% water on average? Earth Planet Sci Lett 364:168-179
948 Pistone M (2012) Physical properties of crystal- and bubble-bearing magmas. Dissertation, ETH-
949 Zurich
950 Pistone M, Caricchi L, Ulmer P, Burlini L, Ardia P, Reusser E, Marone F, Arbaret L (2012)
951 Deformation experiments of bubble- and crystal-bearing magmas: rheological and microstructural
952 analysis. J Geophys Res 117:doi:10.1029/2011JB008986
953 Pistone M, Caricchi L, Ulmer P, Reusser E, Ardia P (2013) Rheology of volatile-bearing crystal
954 mushes: mobilization vs. viscous death. Chem Geol 345:16-39
955 Poldervaart A, Taubeneck WH (1959) Layered intrusions of the Willow Lake type. Geol Soc Am Bull
956 70:1395-1398
957 Romine WL, Whittington AG, Nabelek PI, Hofmeister AM (2012) Thermal diffusivity of rhyolitic

glasses and melts: effects of temperature, crystals and dissolved water. Bull Volcanol 74:2273-2287

Rouse P (2000) Experimental phase equilibria of sodic phonolites from Montaña Blanca, Tenerife. Dissertation, University of Bristol

Ruprecht P, Bachmann O (2010) Pre-eruptive reheating during magma mixing at Quizapu volcano and the implications for the explosiveness of silicic arc volcanoes. Geology 38:919-922

Ruprecht P, Bergantz GW, Cooper KM, Hildreth W (2012) The crustal magma storage system of Volcán Quizapu, Chile, and the effects of magma mixing on magma diversity. J Petrol 53:801-840

Rutter EH, Brodie KH, Irving DH (2006) Flow of synthetic, wet, partially molten "granite" under undrained conditions: an experimental study. J Geophys Res 111:doi.org/10.1029/2005JB004257

Sinclair WD (2007) Porphyry deposits, In Goodfellow WD (ed), Mineral Deposits of Canada: A Synthesis of Major Deposit-Types, District Metallogeny, the Evolution of Geological Provinces, and Exploration Methods. Geol Ass Can - Mineral Deposits Div - Spec Pub 5:223-243

Sato E, Sato H (2009) Study of effect of magma pocket on mixing of two magmas with different viscosities and densities by analogue experiments, J Volcanol Geotherm Res 181:115-123

Saunders KE, Buse B, Kilburn M, Kearns S, Blundy JD (2014) Nanoscale characterisation of crystal zoning. Chem Geol 364:20-32

Sha L-K (1995) Genesis of zoned hydrous ultramafic/mafic-silicic intrusive complexes: an MHFC hypothesis, Earth Sci Rev 39:59-90

Shannon JR, Walker BM, Carten RB, Geraghty EP (1982) Unidirectional solidification textures and their significance in determining relative ages of intrusions at the Henderson Mine, Colorado. Geology 10:293-297

Sisson TW, Layne GD (1993) H_2O in basalt and basaltic andesite glass inclusions from four subduction-related volcanoes. Earth Planet Sci Lett 117:619-635

Sisson TW, Grove TL (1993) Temperatures and H_2O contents of low MgO high-alumina basalts. Contrib Mineral Petrol 113:167-184

Sisson TW, Grove TL, Coleman DS (1996) Horneblende gabbro sill complex at Onion Valley, California, and amixing origin for the SierraNevada batholith. Contrib Mineral Petrol 126:81-108

Sparks RSJ, Marshall LA (1986) Thermal and mechanical constraints on mixing between mafic and silicic magmas. J Volcanol Geotherm Res 29:99-124

Sylvester AG (2011) The nature and polygenetic origin of orbicular granodiorite in the Lower Castle Creek pluton, northern Sierra Nevada batholith, California. Geosphere 7:1-9

Ulmer P (1986) Basische und ultrabasische Gesteine des Adamello (Provinzen Brescia und Trento, Norditalien). Disseration, ETH-Zürich

Ulmer P (2001) Partial melting in the mantle wedge: the role of H_2O in the genesis of mantle-derived "arc-related" magmas. Phys Earth Planet Inter 127:215-232

Tuttle OF, Bowen NL (1958) Origin of granite in the light of experimental studies in the system $NaAlSi_3O_8$-$KAlSi_3O_8$-SiO_2-H_2O. Geol Soc Am Mem 74, pp. 153

van der Laan SR, Wyllie PJ (1993) Experimental interaction of granitic and basaltic magmas and implications for mafic enclaves. J Petrol 34:491-517

Watson EB (1981) Diffusion in magmas at depth in the earth: the effects of pressure and dissolved H20. Earth Planet Sci Lett 52:291-301

Watson EB (1982) Basaltic contamination by continental crust: some experiments and models. Contrib Mineral Petrol 80:73-87

Watson EB, Jurewicz SR (1984) Behaviour of alkalis during diffusive interaction of granitic xenoliths with basic magmas. J Geol 92:121-131

Webb SL, Dingwell DB (1990) The onset of non-Newtonian rheology of silicate melts: a fiber elongation study. Phys Chem Miner 17:125-132

Webber KL, Falster AU, Simmons W, Foord EE (1997) The role of diffusion-controlled oscillatory nucleation in the formation of line rock in pegmatite-aplite dikes. J Petrol 38:1777-1791

Webber KL, Simmons WB, Falster AU, Foord EE (1999) Cooling rates and crystallization dynamics of shallow level pegmatite-aplite dikes, San Diego County, California. Am Mineral 84:708-717

Wyllie PJ, Cox KG, Biggar GM (1962) The habit of apatite in synthetic systems and igneous rocks. J Petrol 3:238-243

Yoder HSJr, Stewart DB, Smith JR (1957) Ternary feldspars. Carnegie Institution of Washington, Year book 55:206-214

Yoder HSJr, Tilley C.E. (1962) Origin of basalt magmas: An experimental study of natural and synthetic rock systems. J Petrol 3:342-532

Yoder HSJr (1973) Contemporaneous basaltic and rhyolitic magmas. Am Mineral 58:153-171

FIGURE CAPTIONS

Figure 1: Examples of textures produced by hydrous mafic magmas from the Tertiary Adamello Batholith, (Alps, Italy). ***A)*** Polished section from the Val Fredda Complex (Blundy and Sparks 1992) showing interaction between hornblende-rich gabbro (lower dark portion) and tonalite host (upper lighter portion). The interaction between the two rocks is marked by a fine-grained "chilled margin" to the gabbro. Wisps of solidified mafic magma can be seen rising from the interface and permeating the tonalite, which is rendered anomalously darker as a consequence. Rounded, grey quartz phenocrysts in the tonalite have developed hornblende-bearing coronas as a consequence of interaction with mafic magma. ***B)*** Example of comb layering (a variant of unidirectional solidification texture - UST) from the north-west flanks of Cornone di Blumone (John and Blundy 1993). Black hornblendes grow upwards from the curved interface in the centre of the photograph. A second comb layer lies above the main layer, separated from the first by banded, fine-grained rock. The comb layers cut equigranular gabbro host rock. ***C)*** Another example of comb layering from the same locality as (B). In this case the comb texture is defined by elongate white plagioclase crystals growing perpendicular to an interface (near coin). Mafic rock below the interface is uniformly fine-grained and banded. A second comb layer lies beneath the fine-grained layer. In the main comb layered region plagioclase grain size increases upwards away from the interface, while the number density of plagioclase grains decreases. The comb layer is asymmetric and abuts medium-grained host diorite at the top of the photograph.

Figure 2: BSE images of key textural features associated with interfaces in the different run products: ***A)*** F0-M, ***B)*** F0-M-F0, ***C)*** F50-M, ***D)*** F60-M-F60, ***E)*** F70-M, ***F)*** F80-M-F80, ***G)*** F50-M, ***H)*** M-M. Run details given in Table 1. The phases present: vesicles (black circles), hornblende (very light grey objects in M and light grey objects in F0), plagioclase (light grey objects), oxides (white objects), quartz (very dark grey objects), and silicic glass (dark grey matrix). The black and white scale bars are: 500 μm in ***A,*** 200 μm in ***C-F, H,*** and 100 μm in ***G***.

Figure 3: BSE images of textures of cooling experiments on starting material M: ***A-B)*** fast cooling (1000 to 950 °C; 3.3 °C/second; 4 kbar), and ***C-D)*** slow cooling (1000 to 950 °C; 1 °C/minute; 4 kbar). The phases present have the same grey-scale characteristics as Figure 2. Images are arranged with the

sample periphery on the right hand side and sample core on the left hand side. The black scale bar is 300 μm in ***A-B*** and 100 μm in ***C-D***.

Figure 4: ***A)*** Representative EPMA-based characteristic X-ray distribution maps of run product F0-M. ***B)*** Representative SEM-based false-colour characteristic X-ray distribution maps of run product F70-M. Both grey (***A***) and colour scales (***B***) of the X-ray distribution maps are expressed in wt.%.

Figure 5: EPMA- and SIMS-based molar ratio (ASI = $Al_2O_3/[CaO+Na_2O+K_2O]$, Al/Si, Al/Na, Al/K, and Na/K) profiles across the interaction interface in different run products. EPMA- and SIMS-based concentration profiles of major oxides and trace elements are reported in the Supplementary Material. Data are displayed according to the distance of the analysis spots from the interface(s) (see Supplementary Material).

Figure 6: SIMS- and EPMA-based H_2O contents along the different run products (except run products F50-F0 and M-M, which are reported in the Supplementary Material). Data are displayed according to the distance of the analysis spots from the interface(s) (see Supplementary Material).

Figure 7: Calculated local liquidus temperatures (T_L, computed using the model of Makhluf et al. 2014, based on EPMA and SIMS data; standard error of ±4 °C) across the different run products. A few computed values of T_L in the dacite of run products F50-M, F60-M-F60, and F70-M are < 800 °C, and therefore not displayed.

Figure 8: ***A)*** Normalised temperature ($T' = T_{experimental} / T_L$) versus dimensionless crystal nucleation and growth rate (after Hort 1998). The grey line (at $T' = 1$) separates the field of supercooling ($T' > 1$) from that of undercooling ($T' < 1$). Black and brown lines indicate the Gaussian trends of crystal growth and nucleation rate respectively. Red and blue areas indicate the nucleation and growth of crystals in the dacite and andesite respectively. The orange area indicates common conditions of nucleation and growth of crystals in the two interacting domains. Two inset schematics indicate the H_2O content conditions under which crystal nucleation rate is favoured (low H_2O content) or crystal growth rate is supported (high H_2O content). ***B-D)*** Conceptual diagrams showing the effect of

undercooling (i.e. temperature difference, ΔT, between the contact temperature at the interface, $T_{interface}$, and the liquidus temperature of the felsic (blue), $T_{L(felsic)}$, or the liquidus temperature of the mafic magma (red), $T_{L(mafic)}$) in three end-member scenarios: ***B)*** heat diffusion from anhydrous mafic to anhydrous felsic magma, which generates chilled margins at the interface of the mafic domain and limited partial melting of the felsic domain; ***C)*** both heat and H_2O diffusion from H_2O-saturated mafic to anhydrous felsic magma, which causes dramatic crystallisation of the mafic domain, including the formation of chilled margins at the interface, and diffuse partial melting of the felsic domain; ***D)*** isothermal (i.e. $T_{interface}$ = actual temperature of the interacting magmas, T_{actual}) H_2O diffusion from H_2O-saturated mafic to anhydrous (or H_2O-undersaturated) felsic magma, which promotes the generation of comb layering in the mafic domain and super-liquidus melt at the interface in the felsic domain. The H_2O diffusion promotes a drop of the $T_{L(felsic)}$, with enrichment of H_2O in the residual melt. Conversely, H_2O release from the mafic melt favours an increase of the $T_{L(mafic)}$ with an inward crystallisation (from the mafic-felsic interface to the mafic core), which is initially nucleation-driven (evidenced by the presence of microlites at the interface; Figures 1A-B), then growth-driven (characterised by elongate crystals arranged in a comb layering structure towards the mafic-felsic interface; Figures 1B-C). The diagram shows the schematics of textures generated during the experiments. Different crystals are: quartz (red hexagons) with orange SiO_2-dissolution rims, hornblende (black rectangles), plagioclase (light brown rectangles) and Fe-Ti oxides (yellow squares).

TABLE CAPTIONS

Table 1: Summary of the high-temperature and high-pressure experiments from this study. Abbreviations: ϕ = sample diameter; l = sample length; V = sample volume; m = sample mass; ρ = sample density at room conditions; V_{felsic} / V_{mafic} = total volume ratio between felsic and mafic sample; m_{felsic} / m_{mafic} = total mass ratio between felsic and mafic sample; $\rho_{felsic} / \rho_{mafic}$ = total density ratio between felsic and mafic sample; T = temperature; P = pressure; ***Glass*** = residual silicic glass; ***Hbl*** = hornblende; ***Plag*** = plagioclase; ***Ox*** = Fe-Ti oxide; ***Qz*** = quartz; ***Bubble*** = gas bubble. The values of volumetric proportions of the different phases within the single samples in the run products are reported in vol.%. Runs M_cooling_01 and M_cooling_02 were conducted with cooling rates of 3.3 °C/second (fast cooling); runs M_cooling_03 and M_cooling_04 were conducted with cooling rates of

1 °C/minute (slow cooling). Underlined = experiment conducted by using a cold seal vessel; (*) = experiment performed with Pt capsule.

Table 2: Representative EPMA analyses of the bulk matrix glass from starting materials and mineral compositions from selected experimental charges from this study. Chemical analyses are volatile-free basis. H_2O contents here reported are from SIMS analyses (*); H_2O contents are also calculated using the by-difference method (see Figure 6). Uncertainties based on counting statistics of the reported concentrations are in the range of 0.5-1.5% for SiO_2, Al_2O_3 and CaO, 1-7% for Na_2O and K_2O, 3-22% for TiO_2, FeO_T, MgO and MnO. The maximum uncertainties for reported molar ratios, calculated via error propagation, are: 31% for ASI (Al_2O_3/[CaO+Na_2O+K_2O]), 3% for Na/K, 1% for Al/K, 2% for Al/Na, and 10% for Al/Si. In italics = selected hornblende mineral located at a distance of ~50 μm far from the closest quartz crystal; the analysis of the other hornblendes display higher SiO_2 content (~50-55 wt.%) due to larger SiO_2 content in the glass surrounding quartz crystals, as evidenced by FEG-probe analyses (Supplementary Material).

Table 3: EPMA-based chemical profiles within the glass phase in the experimental charges simulating sample-sample interaction from this study (see also Figure 5). Chemical analyses are volatile-free basis; H_2O contents are calculated using the by-difference method. Locations of the EPMA and H_2O-SIMS analysis spots are displayed in the Supplementary Material.

Table 4: SIMS analyses of the silicic glass in the run products simulating sample-sample interaction (see also Figure 6). All data are Si-normalised and corrected following the Geological and Environmental Reference Materials (GeoReM) database. Locations of the analysis spots are displayed in the Supplementary Material.

SUPPLEMENTARY MATERIAL

Figure SM1: ***A-D)*** SEM-based BSE images detailing the sample-sample interaction interface of the run products: ***A)*** F0-M; ***B)*** F0-M-F0; ***C)*** F50-M; ***D)*** F60-M-F60; ***E)*** F70-M; ***F)*** F80-M-F80; ***G)*** F50-F0; ***H)*** M-M; ***I)*** F50-M (CSV). The phases present: vesicles (black circles), hornblende (very light grey objects in M and light grey objects in F0), plagioclase (light grey objects), oxides (white objects),

quartz (very dark grey objects), and silicic glass (dark grey matrix). Red and brown dots indicate EPMA analysis spots; blue and purple dots indicate SIMS analysis spots in the felsic and mafic domain respectively (and, felsic mush and felsic crystal-free sample of the run product F50-F0 respectively); yellow and orange dots indicate SIMS analysis spots in the upper mafic and lower mafic domain respectively. Black arrows indicate the location of the interfaces between samples. The black scale bar is 1 mm in all images.

Figure SM2: BSE image showing representative FEG-EPMA-based analysis spots reporting the SiO_2 content across quartz crystal and surrounding silicic glass in the run product F70-M. Black circles of Profile 1 (***A***) and Profile 2 (***B***) (see analysis spots data reported in Table SM1).

Figure SM3: EPMA- and SIMS-based concentration profiles of major elements across the interaction interface in different run products. Data are displayed according to the distance of the analysis spots from the interface(s) (see Figure SM1).

Figure SM4: SIMS-based concentration profiles of trace elements and SIMS- and EPMA-based H_2O contents along the different run products (including F50-F0 and M-M). Data are displayed according to the distance of the analysis spots from the interface(s) (see Figure SM1).

Table SM1: Representative FEG-EPMA data from analysis spots of the quartz crystals and surrounding silicic glass in the experimental charge F70-M. All presented data are affected by 1 to 5% standard error. Locations of the analysis spots are displayed in Figure SM2.

Figure 1

Figure 2

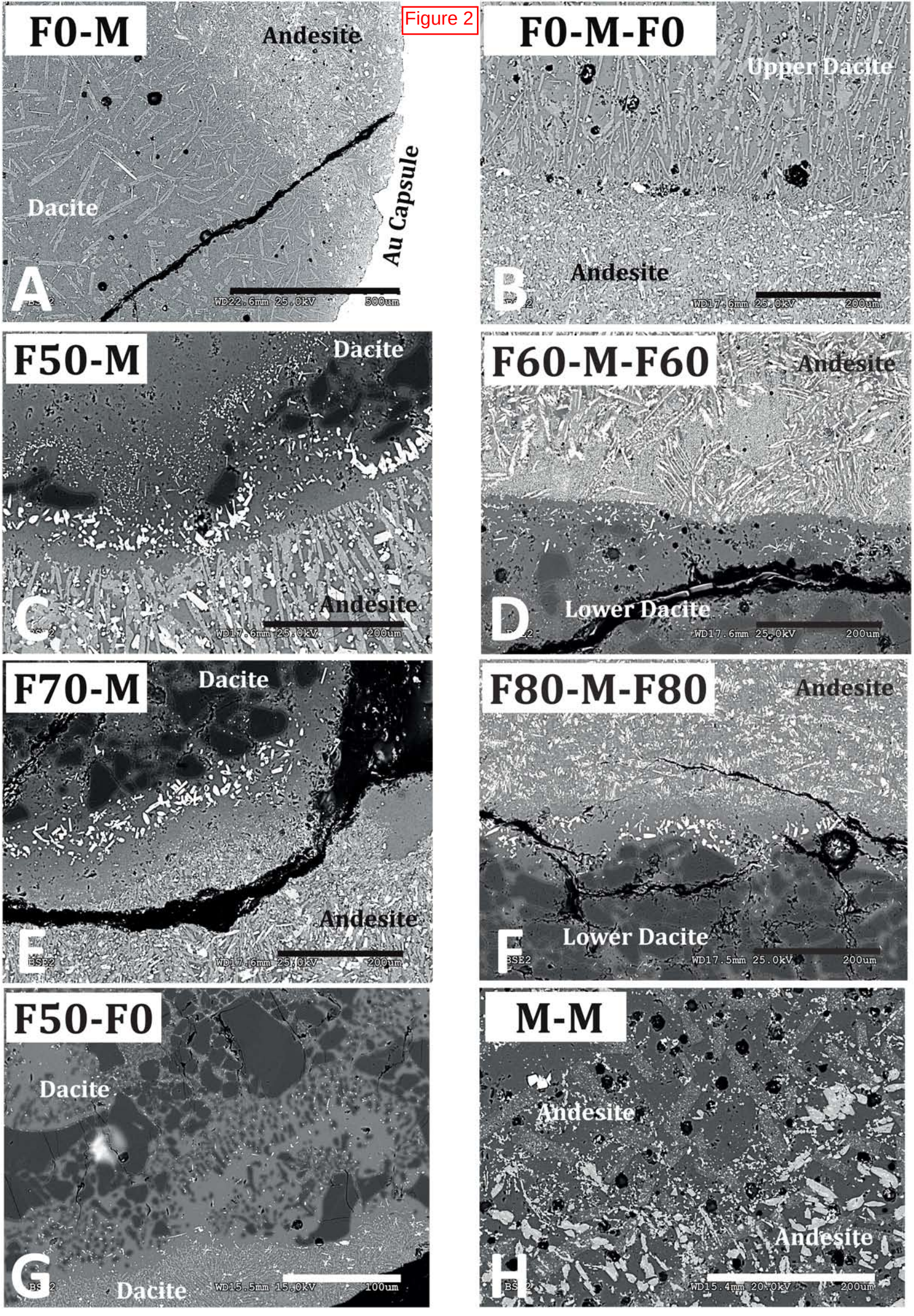
F0-M
Andesite
Dacite
Au Capsule
A
WD22.6mm 25.0kV
500um
F0-M-F0
Upper Dacite
Andesite
B
WD17.6mm 25.0kV
200um
F50-M
Dacite
Andesite
C
WD17.6mm 25.0kV
200um
F60-M-F60
Andesite
Lower Dacite
D
WD17.6mm 25.0kV
200um
F70-M
Dacite
Andesite
E
BSE2
WD17.6mm 25.0kV
200um
F80-M-F80
Andesite
Lower Dacite
F
BSE2
WD17.5mm 25.0kV
200um
F50-F0
Dacite
Dacite
G
WD15.5mm 15.0kV
100um
M-M
Andesite
Andesite
H
WD15.4mm 20.0kV
200um

Figure 3

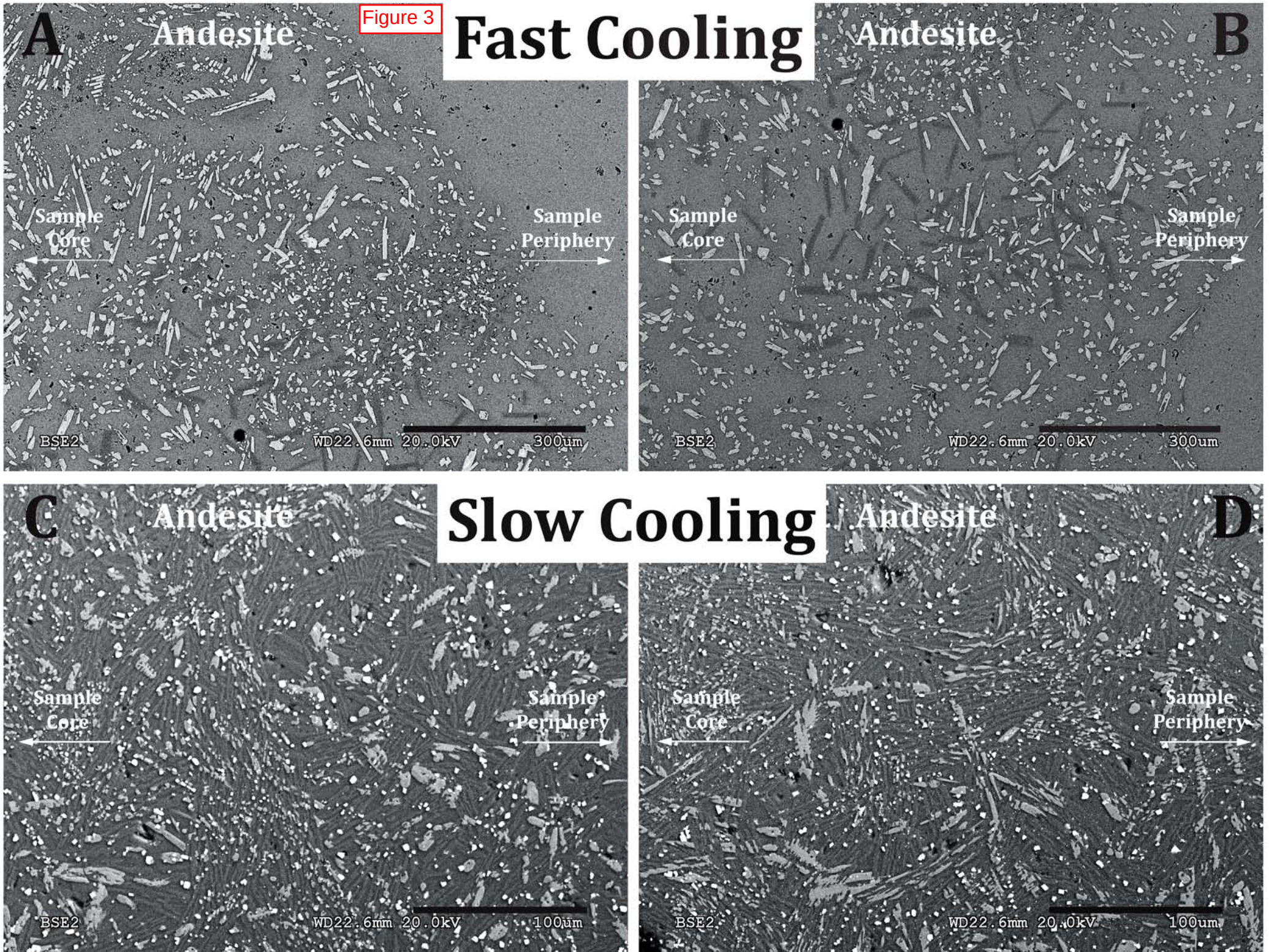
A
Andesite
Fast Cooling
Sample Core
Sample Periphery
BSE2
WD22.6mm 20.0kV
300um
B
Andesite
Sample Core
Sample Periphery
BSE2
WD22.6mm 20.0kV
300um
C
Andesite
Slow Cooling
Sample Core
Sample Periphery
BSE2
WD22.6mm 20.0kV
100um
D
Andesite
Sample Core
Sample Periphery
BSE2
WD22.6mm 20.0kV
100um

Figure 4

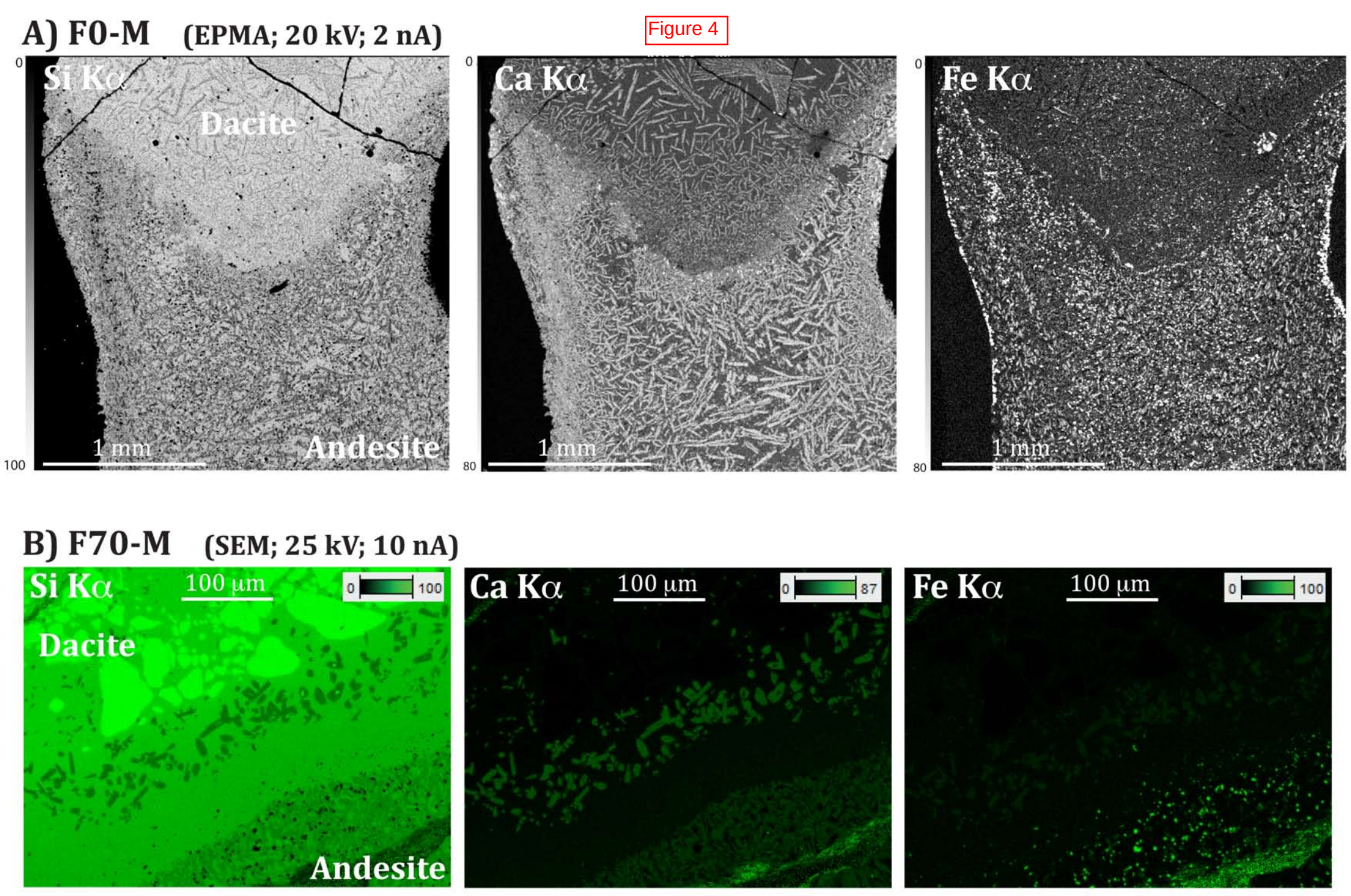
A) F0-M (EPMA; 20 kV; 2 nA)
Si Kα
Dacite
Andesite
1 mm
Ca Kα
Fe Kα
B) F70-M (SEM; 25 kV; 10 nA)
100 µm
0
100
87
80

Figure 5

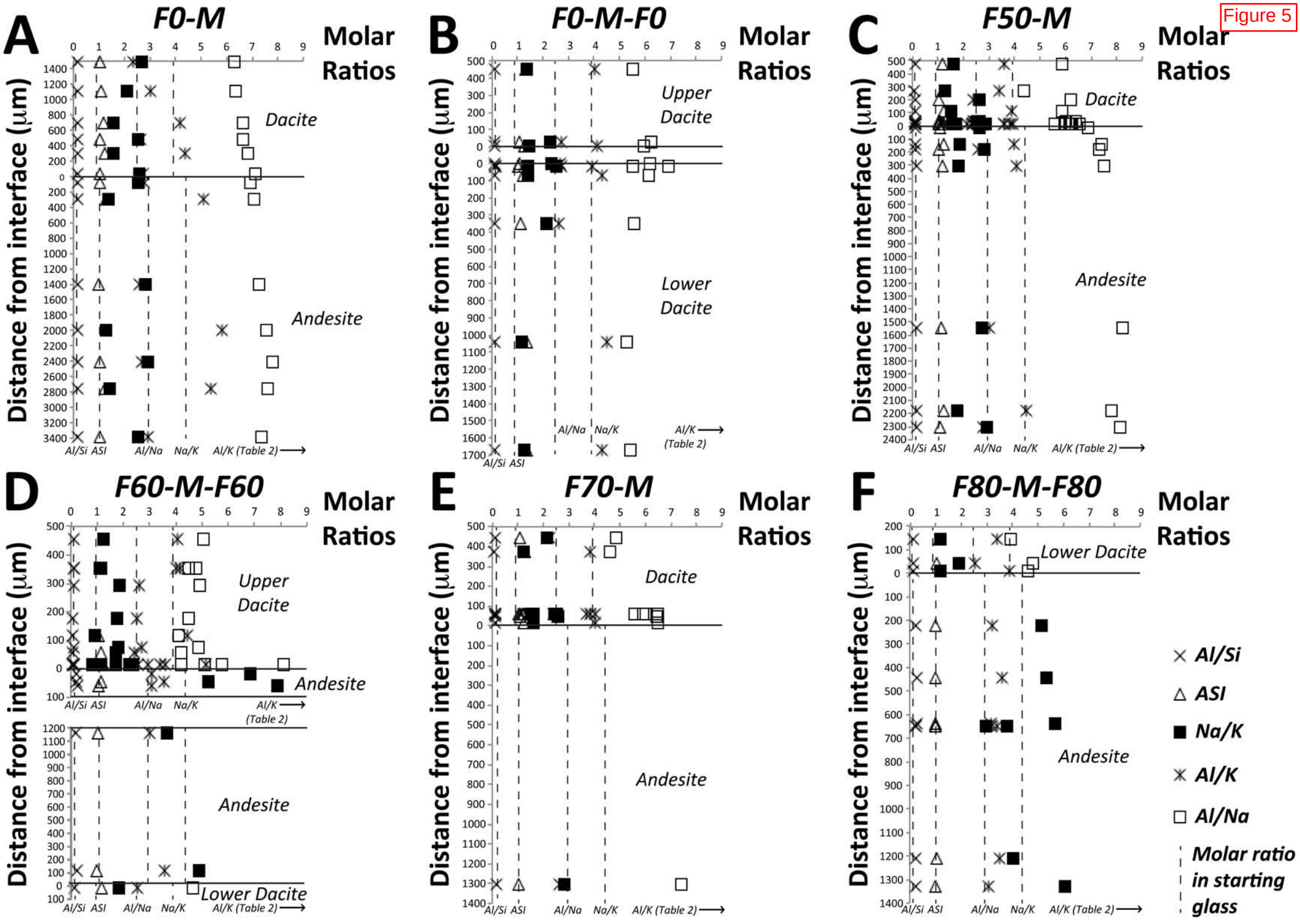
A
F0-M
Molar Ratios
Distance from interface (μm)
Dacite
Andesite
Al/Si ASI
Al/Na
Na/K
Al/K (Table 2)
B
F0-M-F0
Upper Dacite
Lower Dacite
C
F50-M
D
F60-M-F60
E
F70-M
F
F80-M-F80
Lower Dacite
Al/Si
ASI
Na/K
Al/K
Al/Na
Molar ratio in starting glass

Figure 6

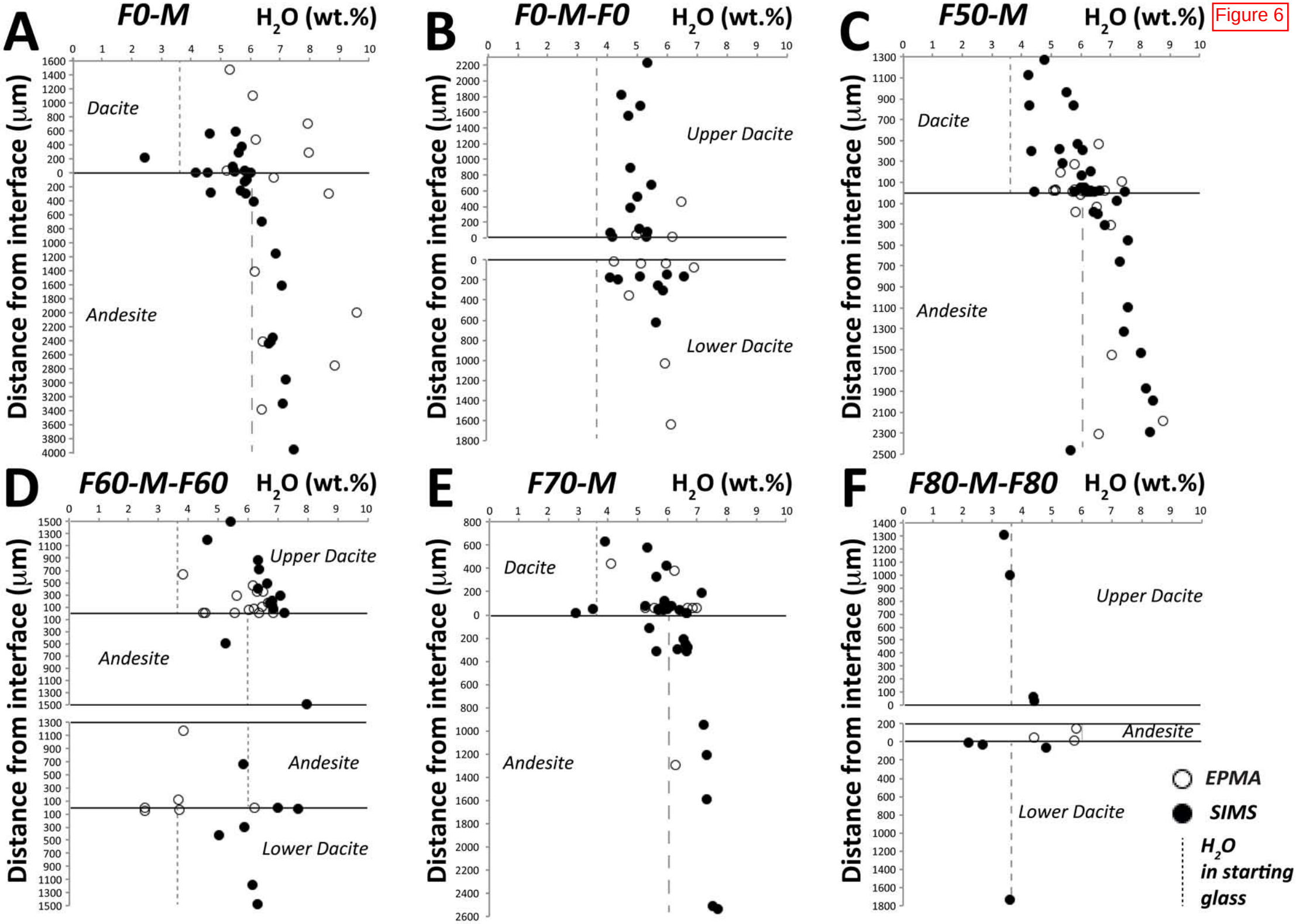
A
F0-M
H2O (wt.%)
Distance from interface (μm)
Dacite
Andesite
B
F0-M-F0
Upper Dacite
Lower Dacite
C
F50-M
D
F60-M-F60
E
F70-M
F
F80-M-F80
EPMA
SIMS
H2O in starting glass

Figure 7

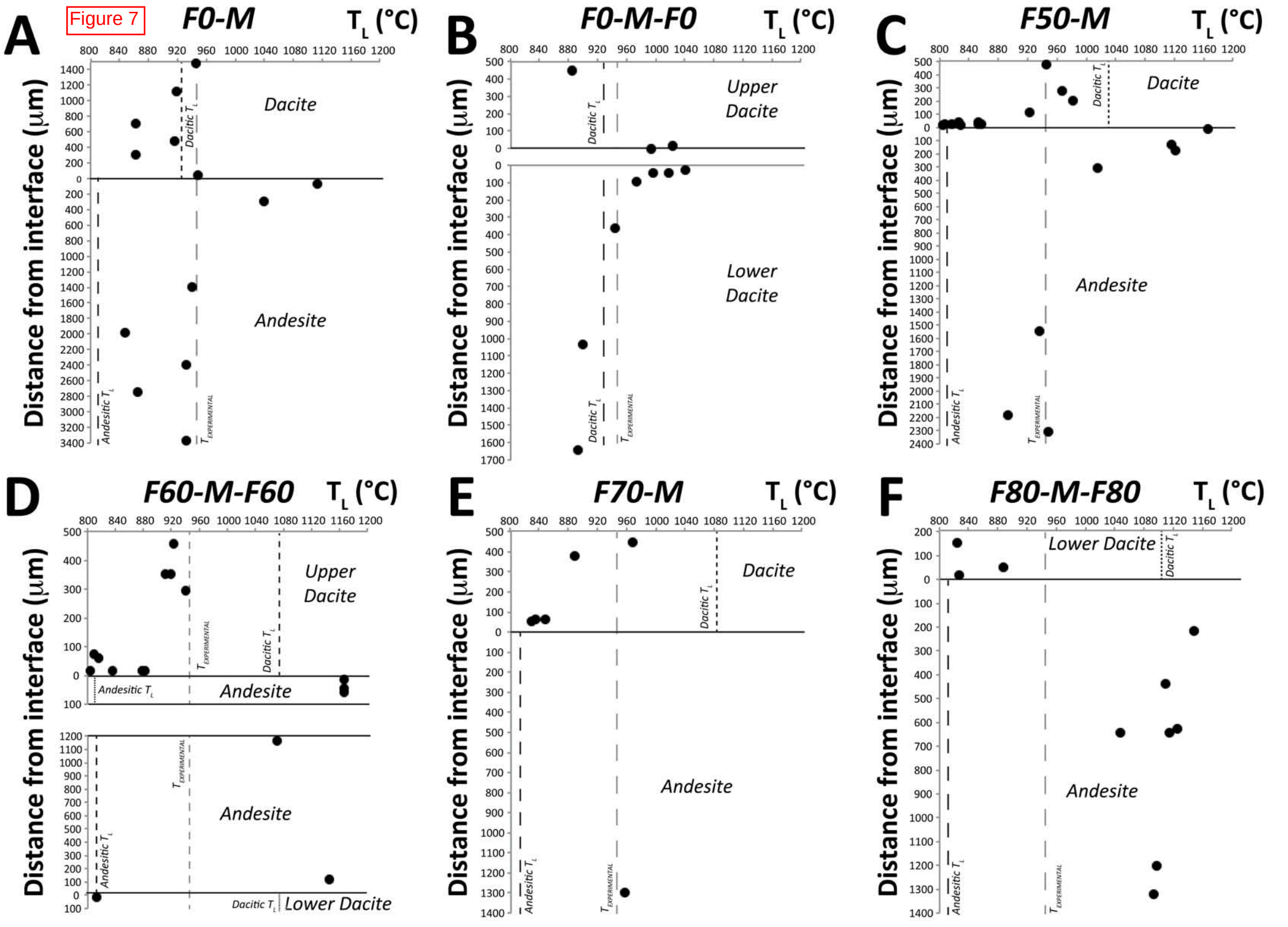
A
F0-M
T_L (°C)
Distance from interface (μm)
Dacite
Andesite
Dacitic T_L
Andesitic T_L
T_EXPERIMENTAL
B
F0-M-F0
Upper Dacite
Lower Dacite
C
F50-M
D
F60-M-F60
Lower Dacite
E
F70-M
F
F80-M-F80

Figure 8

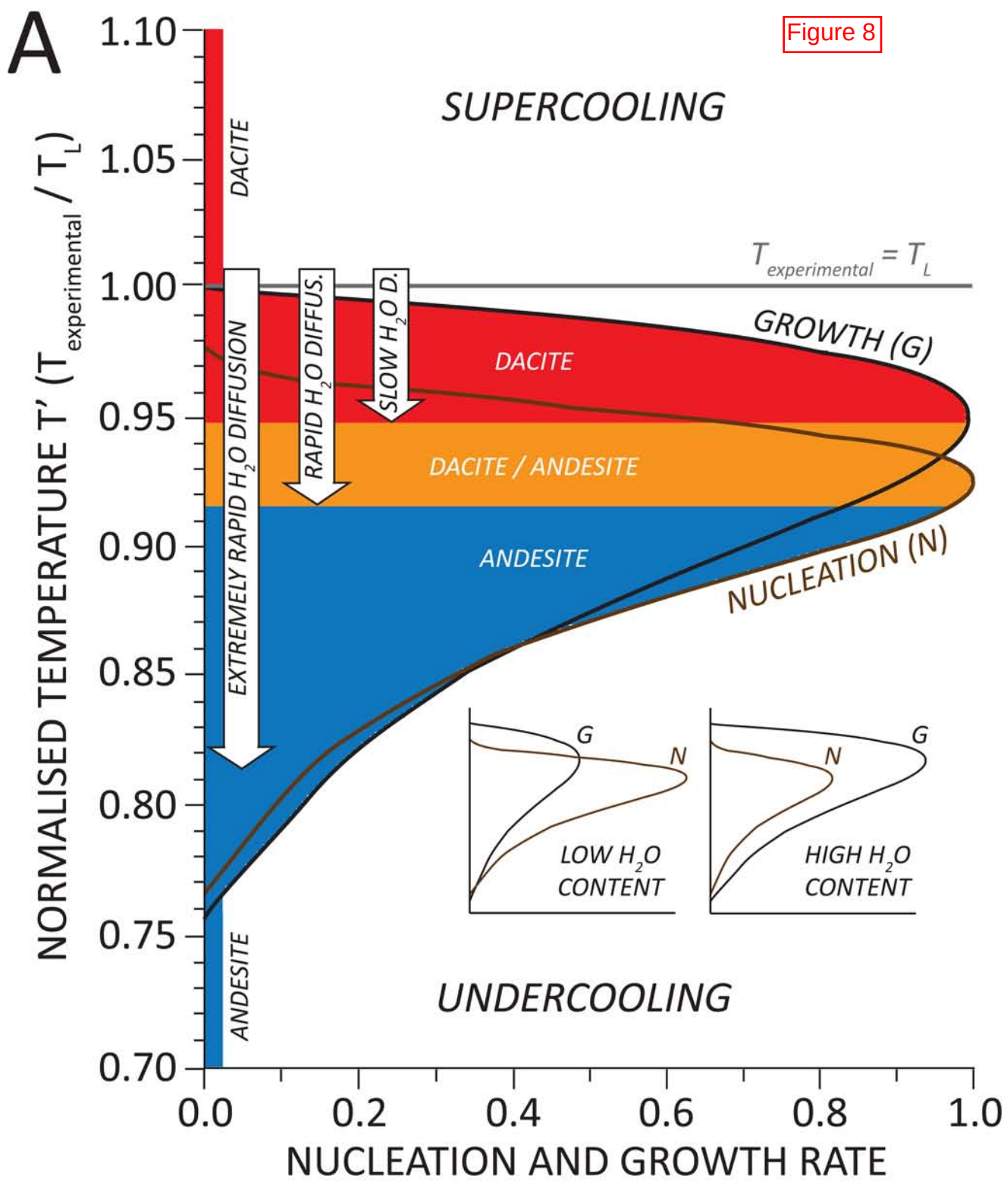
A
SUPERCOOLING
UNDERCOOLING
DACITE
ANDESITE
EXTREMELY RAPID H_2O DIFFUSION
RAPID H_2O DIFFUS.
SLOW H_2O D.
$T_{experimental} = T_L$
GROWTH (G)
NUCLEATION (N)
DACITE
DACITE / ANDESITE
ANDESITE
G
N
LOW H_2O CONTENT
HIGH H_2O CONTENT
NORMALISED TEMPERATURE T' ($T_{experimental}$ / T_L)
NUCLEATION AND GROWTH RATE
1.10
1.05
1.00
0.95
0.90
0.85
0.80
0.75
0.70
0.0
0.2
0.4
0.6
0.8
1.0

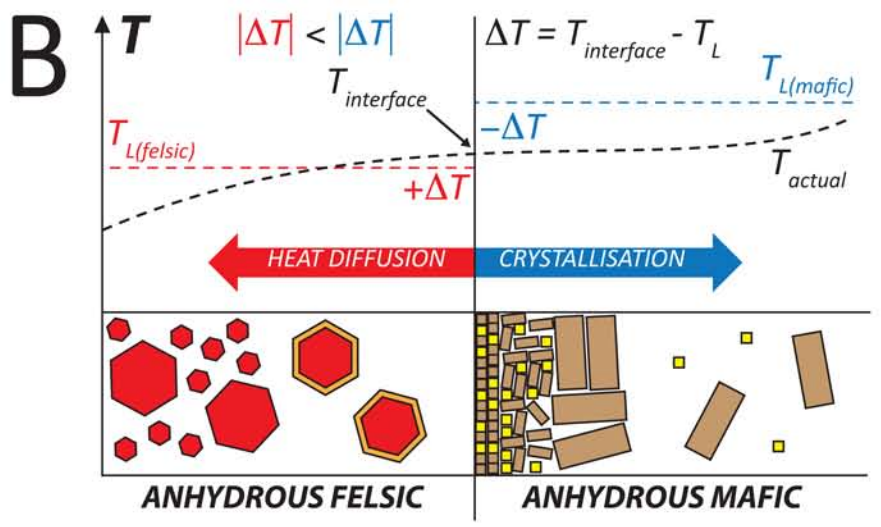
B
T
$|\Delta T| < |\Delta T|$
$\Delta T = T_{interface} - T_L$
$T_{interface}$
$T_{L(felsic)}$
$T_{L(mafic)}$
$-\Delta T$
$+\Delta T$
T_{actual}
HEAT DIFFUSION
CRYSTALLISATION
ANHYDROUS FELSIC
ANHYDROUS MAFIC

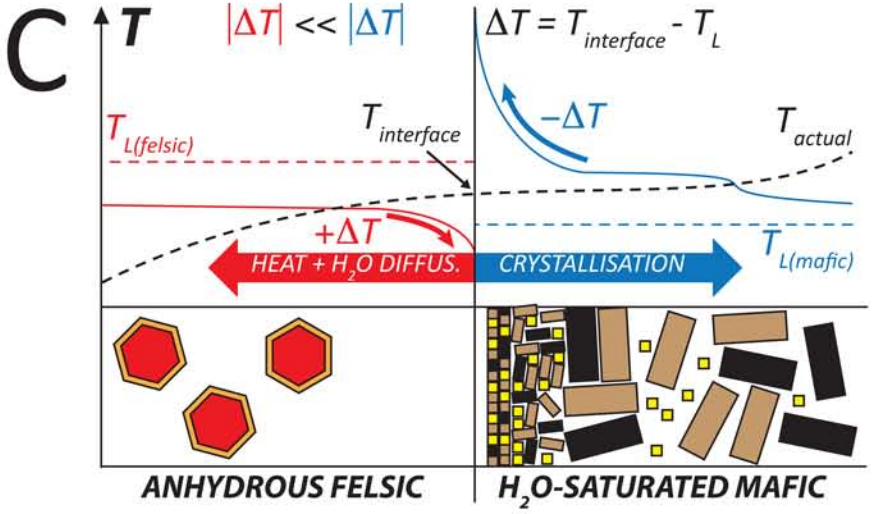
C
T
$|\Delta T| << |\Delta T|$
$\Delta T = T_{interface} - T_L$
$T_{L(felsic)}$
$T_{interface}$
$-\Delta T$
T_{actual}
$+\Delta T$
$T_{L(mafic)}$
HEAT + H_2O DIFFUS.
CRYSTALLISATION
ANHYDROUS FELSIC
H_2O-SATURATED MAFIC

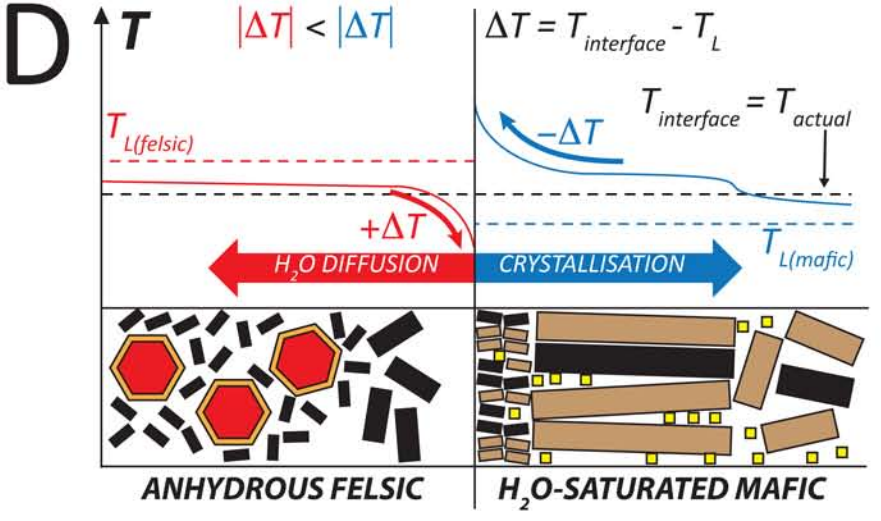
D
T
$|\Delta T| < |\Delta T|$
$\Delta T = T_{interface} - T_L$
$T_{interface} = T_{actual}$
$T_{L(felsic)}$
$-\Delta T$
$+\Delta T$
$T_{L(mafic)}$
H_2O DIFFUSION
CRYSTALLISATION
ANHYDROUS FELSIC
H_2O-SATURATED MAFIC

Table 1

Experiment	*Sample*	*ø (mm)*	*l (mm)*	*V (mm^3)*	*m (g)*	*ρ (kg/m^3)*	*V_{felsic} / V_{mafic}*	*m_{felsic} / m_{mafic}*	*$ρ_{felsic}$ / $ρ_{mafic}$*	*T (°C)*	*P (kbar)*	*Duration (hours)*	*Glass*	*Hbl*	*Plag*	*Ox*	*Qz*	*Bubbles*
F0_01(*)	*F0*	2.99	2.48	17.41	0.0416	2389	-	-	-	950	4	1	-	-	-	-	-	-
F0_02	*F0*	-	-	-	0.0226	-	-	-	-	950	4	24	60	38	0	2	0	0
F0_03	*F0*	-	-	-	0.0190	-	-	-	-	950	4	24	68	31	0	1	0	0
F80_01	*F80*	-	-	-	0.0231	-	-	-	-	950	4	24	20	0	0	0	80	0
F80_02	*F80*	-	-	-	0.0116	-	-	-	-	950	4	24	20	0	0	0	80	0
M_01(*)	*M*	2.95	1.95	13.33	0.0391	2934	-	-	-	950	4	24	-	-	-	-	-	-
M_02	*M*	-	-	-	0.0122	-	-	-	-	950	4	24	50	19	30	1	0	0
M_03	*M*	-	-	-	0.0144	-	-	-	-	950	4	24	55	10	34	1	0	0
M_cooling_01	*M*	2.91	6.16	40.97	0.1053	2570	-	-	-	1000 to 950	4	0.004	70	18	10	1	0	1
M_cooling_02	*M*	2.92	3.68	24.64	0.0517	2098	-	-	-	1000 to 950	4	0.004	70	17	11	1	0	1
M_cooling_03	*M*	2.94	5.20	35.30	0.0858	2431	-	-	-	1000 to 950	4	0.83	5	20	70	4	0	1
M_cooling_04	*M*	2.95	5.80	39.64	0.0954	2407	-	-	-	1000 to 950	4	0.83	6	24	65	4	0	1
F0-M	*F0*	3.01	2.05	14.59	0.0348	2386	0.68	0.63	0.93	950	4	24	62	34	0	3	0	1
	M	2.94	3.18	21.59	0.0553	2562							55	14	26	4	0	1
M-F0	*M*	2.90	3.10	20.48	0.0530	2588	1.45	1.38	0.95	650	4	0.5	0	35	50	5	0	10
	F0	2.99	4.22	29.63	0.0732	2470							90	3	0	2	0	5
F50-M	*F50*	2.99	1.20	8.43	0.0187	2219	0.38	0.32	0.85	950	4	24	41	5	0	3	50	1
	M	2.92	3.34	22.37	0.0587	2624							49	20	27	2	0	2
F60-M-F60	*F60*	2.94	2.09	14.19	0.0333	2347	1.22	1.11	0.91	950	4	24	27	3	0	3	65	2
	M	2.93	3.43	23.13	0.0595	2573							36	23	35	3	0	3
	F60	2.92	2.10	14.06	0.0326	2318							29	3	0	3	63	2
F70-M	*F70*	2.97	2.06	14.27	0.0342	2396	0.58	0.54	0.93	950	4	24	20	7	0	2	70	1
	M	2.94	3.60	24.44	0.0629	2574							49	17	30	2	0	2
F80-M-F80	*F80*	3.00	2.22	15.69	0.0385	2453	1.33	1.25	0.94	950	4	24	9	7	0	3	80	1
	M	2.95	3.61	24.67	0.0646	2618							40	19	37	3	0	1
	F80	3.00	2.43	17.18	0.0425	2474							9	7	0	3	80	1
F0-M-F0	*F0*	3.00	2.52	17.81	0.0435	2442	2.29	2.14	0.93	950	4	168	69	27	0	3	0	1
	M	2.91	2.38	15.83	0.0415	2622							0	37	50	12	0	1
	F0	3.00	2.61	18.45	0.0452	2450							67	29	0	3	0	1
F50-F0	*F50*	4.20	2.92	40.45	-	-	1.14	-	-	950	4	22	41	2	0	1	55	1
	F0	3.88	2.99	35.35	0.0864	2444							55	38	0	6	0	1
M-M	*M*	4.03	3.01	38.39	0.0956	2490	1.01	1.00	0.99	950	4	25	55	10	18	10	0	7
	M	4.01	3.02	38.14	0.0958	2512							43	10	35	4	0	8
F50-M	*F50*	2.95	1.74	11.89	0.0276	2321	1.21	1.09	0.90	827	2 to 1	48	27	0	0	3	50	20
	M	2.92	1.47	9.84	0.0253	2570							8	20	46	4	0	22

Table 2

Sample Type	Sample Name	SiO_2	TiO_2	Al_2O_3	FeO_{TOT}	MnO	MgO	CaO	Na_2O	K_2O	H_2O	ASI	Na/K	Al/K	Al/Na	Al/Si
Starting Materials	***M***	60.96 (0.92)	0.84 (0.12)	22.11 (0.17)	2.94 (0.59)	0.22 (0.04)	0.18 (0.07)	6.59 (0.14)	4.54 (0.27)	1.62 (0.11)	6.03 (0.02)*	1.04 [0.32]	4.26 [0.09]	12.61 [0.07]	2.96 [0.06]	0.21 [0.02]
	F0	64.54 (0.33)	0.50 (0.04)	18.12 (0.20)	3.79 (0.12)	0.26 (0.02)	1.56 (0.08)	5.28 (0.08)	4.29 (0.06)	1.66 (0.04)	3.69 (0.02)*	0.98 [0.11]	3.93 [0.03]	10.08 [0.03]	2.57 [0.02]	0.17 [0.01]
F0 / M	***Plag in M***	52.17 (0.16)	-	28.90 (0.35)	0.82 (0.25)	-	0.13 (0.04)	13.75 (0.07)	4.00 (0.15)	0.25 (0.01)	-	-	-	-	-	-
	Hbl in M	43.14 (0.10)	2.37 (0.16)	12.92 (0.62)	12.43 (0.51)	0.60 (0.51)	14.28 (0.71)	11.48 (0.07)	2.29 (0.11)	0.49 (0.03)	2.86 (0.07)	-	-	-	-	-
	Oxide in M	-	3.21 (0.57)	4.91 (0.02)	85.23 (0.79)	1.60 (0.04)	5.05 (0.71)	-	-	-	-	-	-	-	-	-
F50 / M	***Plag in M***	53.43 (1.08)	0.18 (0.09)	28.49 (0.45)	1.65 (0.31)	0.04 (0.02)	0.23 (0.06)	11.54 (0.14)	4.12 (0.22)	0.27 (0.01)	-	-	-	-	-	-
	Hbl in M	43.00 (0.08)	2.15 (0.20)	13.79 (0.65)	13.14 (0.33)	0.60 (0.45)	13.27 (0.94)	11.38 (0.18)	2.12 (0.23)	0.55 (0.14)	2.76 (0.19)	-	-	-	-	-
	Oxide in M	-	5.21 (0.21)	1.81 (0.02)	87.46 (0.88)	1.45 (0.04)	4.07 (0.45)	-	-	-	-	-	-	-	-	-
	Quartz in F50	99.87 (0.01)	-	0.04 (0.01)	0.09 (0.01)	-	-	-	-	-	-	-	-	-	-	-
	Hbl in F50	*46.55 (0.51)*	*2.51 (0.02)*	*11.46 (0.08)*	*10.36 (0.04)*	*0.77 (0.08)*	*10.22 (0.78)*	*13.48 (0.63)*	*3.87 (0.47)*	*0.78 (0.04)*	*2.74 (0.24)*	-	-	-	-	-

Table 3

F0-M	F0						M						
Analysis Spot	1	2	3	4	5	6	7	8	9	10	11	12	13
SiO_2	68.44	68.53	68.64	67.67	68.32	67.32	66.98	67.78	66.60	66.53	65.64	66.50	66.13
TiO_2	0.54	0.52	0.53	0.57	0.56	0.55	0.63	0.68	0.67	0.65	0.60	0.63	0.61
Al_2O_3	16.30	16.48	16.94	16.60	17.24	17.01	17.04	17.52	16.93	18.00	17.41	18.08	17.37
FeO_T	2.90	3.21	3.09	3.12	3.18	3.13	3.30	3.25	3.16	3.56	3.38	3.50	3.32
MnO	0.17	0.24	0.26	0.22	0.24	0.23	0.27	0.27	0.31	0.36	0.36	0.36	0.33
MgO	1.35	1.50	1.58	1.64	1.55	1.58	1.63	1.66	1.73	1.92	1.91	1.89	1.73
CaO	3.60	3.82	4.12	4.02	4.16	4.18	4.15	4.42	4.42	4.89	4.64	4.80	4.70
Na_2O	4.25	3.31	2.47	3.85	2.40	3.77	3.74	2.09	4.01	1.87	3.98	2.04	3.64
K_2O	2.39	2.39	2.36	2.32	2.34	2.21	2.27	2.30	2.16	2.20	2.06	2.19	2.18
H_2O	5.29	6.08	7.93	6.18	7.96	5.22	6.78	8.65	6.15	9.58	6.40	8.83	6.40
ASI	1.01	1.10	1.20	1.03	1.23	1.05	1.06	1.26	1.00	1.25	1.01	1.25	1.03
Na/K	2.70	2.10	1.59	2.52	1.56	2.59	2.51	1.38	2.82	1.30	2.93	1.41	2.54
Al/K	6.29	6.36	6.62	6.62	6.81	7.10	6.94	7.05	7.25	7.57	7.79	7.61	7.36
Al/Na	2.33	3.03	4.18	2.62	4.36	2.74	2.77	5.10	2.57	5.84	2.66	5.38	2.90
Al/Si	0.14	0.14	0.15	0.14	0.15	0.15	0.15	0.15	0.15	0.16	0.16	0.16	0.15
Distance (μm)	1482	1111	704	482	296	37	74	296	1407	2000	2407	2759	3389

F0-M-F0	$F0_{bottom}$							$F0_{top}$		
Analysis Spot	1	2	3	4	5	6	7	8	9	10
SiO_2	72.98	73.12	71.28	71.62	68.44	71.38	70.34	71.37	69.19	72.30
TiO_2	0.52	0.57	0.60	0.51	0.49	0.50	0.27	0.47	0.54	0.56
Al_2O_3	15.67	15.47	15.60	16.00	17.25	15.30	16.48	16.35	16.23	15.67
FeO_T	2.15	2.16	2.12	2.23	2.12	3.46	2.06	2.25	3.17	2.24
MnO	0.15	0.14	0.20	0.19	0.18	0.23	0.18	0.17	0.19	0.20
MgO	0.95	1.05	1.10	1.16	1.06	1.13	1.01	1.11	1.25	1.17
CaO	2.70	2.70	2.90	3.61	4.29	3.06	3.41	3.28	3.40	2.85
Na_2O	2.20	2.08	3.61	2.25	3.85	2.37	3.76	2.41	3.61	2.37
K_2O	2.66	2.71	2.58	2.41	2.31	2.55	2.46	2.53	2.40	2.63
H_2O	6.19	5.99	4.78	6.96	5.17	6.02	4.28	6.14	4.95	6.44
ASI	1.37	1.37	1.11	1.24	1.04	1.25	1.10	1.29	1.10	1.31
Na/K	1.26	1.16	2.13	1.42	2.53	1.41	2.32	1.45	2.29	1.37
Al/K	5.45	5.27	5.58	6.14	6.91	5.54	6.19	5.97	6.26	5.50
Al/Na	4.33	4.53	2.62	4.33	2.73	3.92	2.67	4.12	2.73	4.02
Al/Si	0.13	0.12	0.13	0.13	0.15	0.13	0.14	0.13	0.14	0.13
Distance (μm)	1645	1032	355	81	32	32	15	15	32	452

F50-M	F50							
Analysis Spot	1	2	3	4	5	6	7	8
SiO_2	74.27	72.29	73.98	72.81	72.62	73.40	74.15	72.17
TiO_2	0.41	0.43	0.42	0.50	0.52	0.51	0.52	0.56
Al_2O_3	14.08	14.71	14.44	14.31	14.92	13.93	14.17	14.69
FeO_T	2.54	2.59	2.56	2.64	2.83	2.59	2.44	2.35
MnO	0.13	0.15	0.17	0.17	0.21	0.17	0.18	0.19
MgO	0.84	0.85	0.81	0.95	1.05	0.88	0.92	1.07
CaO	3.08	3.01	3.07	2.95	3.37	2.82	3.02	3.00
Na_2O	2.39	3.77	2.25	3.60	2.36	3.55	2.38	3.79
K_2O	2.22	2.19	2.27	2.07	2.11	2.14	2.20	2.16
H_2O	6.57	5.30	7.37	5.15	6.28	5.77	6.01	5.06
ASI	1.18	1.05	1.23	1.06	1.21	1.05	1.20	1.05
Na/K	1.64	2.62	1.50	2.64	1.70	2.52	1.65	2.66
Al/K	5.86	6.22	5.87	6.39	6.52	6.03	5.96	6.27
Al/Na	3.58	2.38	3.91	2.42	3.84	2.39	3.62	2.35
Al/Si	0.11	0.12	0.12	0.12	0.12	0.11	0.11	0.12
Distance (μm)	473	200	109	36	18	36	18	18

	F50					M						
Analysis Spot	1	2	3	4	5	6	7	8	9	10	11	12
SiO_2	80.91	72.18	72.49	72.13	74.87	71.30	67.53	68.96	69.01	65.97	67.19	65.91
TiO_2	0.31	0.53	0.57	0.48	0.46	0.56	0.99	0.85	0.91	0.56	0.68	0.67
Al_2O_3	10.09	14.63	14.57	14.44	13.91	15.17	15.76	15.99	16.41	17.90	17.79	17.88
FeO_T	2.03	2.38	2.64	2.77	2.42	2.80	6.01	3.09	3.28	3.47	3.19	3.09
MnO	0.09	0.20	0.23	0.17	0.16	0.21	0.26	0.22	0.28	0.38	0.37	0.38
MgO	0.69	1.11	1.41	0.98	0.87	1.02	1.22	1.32	1.45	1.82	1.81	1.83
CaO	1.88	3.05	3.66	2.71	2.64	3.38	3.85	3.76	4.19	4.26	4.45	4.26
Na_2O	1.80	3.73	2.26	4.06	2.34	3.51	2.40	3.77	2.43	3.62	2.42	3.93
K_2O	2.14	2.19	2.15	2.16	2.30	2.04	1.96	2.02	2.02	2.01	2.11	2.03
H_2O	5.78	5.73	6.33	5.15	6.78	5.98	6.52	5.81	7.01	7.02	8.75	6.59
ASI	1.16	1.04	1.15	1.04	1.25	1.07	1.21	1.05	1.19	1.13	1.24	1.09
Na/K	1.28	2.59	1.60	2.86	1.55	2.61	1.86	2.84	1.83	2.73	1.75	2.94
Al/K	4.35	6.17	6.27	6.18	5.59	6.87	7.42	7.33	7.49	8.22	7.81	8.13
Al/Na	3.40	2.39	3.93	2.16	3.61	2.63	3.99	2.58	4.10	3.01	4.47	2.77
Al/Si	0.07	0.12	0.12	0.12	0.11	0.13	0.14	0.14	0.14	0.16	0.16	0.16
Distance (μm)	273	15	15	18	18	15	136	182	309	1546	2182	2309

F60-M-F60	$F60_{top}$										M
Analysis Spot	1	2	3	4	5	6	7	8	9	10	11
SiO_2	72.40	76.07	74.69	76.78	77.81	77.87	75.24	81.85	72.32	70.00	61.24
TiO_2	0.40	0.46	0.37	0.44	0.28	0.26	0.38	0.29	0.42	0.32	0.19
Al_2O_3	14.84	12.87	13.05	12.90	12.16	11.91	13.11	10.02	13.72	16.47	22.92
FeO_T	2.77	2.52	2.52	2.22	2.02	1.71	2.06	1.47	2.52	2.48	1.35
MnO	0.10	0.12	0.13	0.12	0.10	0.09	0.15	0.11	0.22	0.15	0.10
MgO	0.60	0.66	0.85	0.58	0.70	0.63	0.83	0.50	1.21	0.86	0.32
CaO	3.61	3.01	2.85	2.55	2.55	2.21	2.72	1.84	4.11	4.90	8.38
Na_2O	3.22	1.92	3.03	1.89	1.84	2.86	2.97	1.69	3.25	2.93	4.50
K_2O	2.04	2.35	2.46	2.50	2.51	2.45	2.50	2.21	2.21	1.88	1.00
H_2O	3.81	6.15	5.61	6.27	6.50	6.67	6.19	5.54	6.83	4.49	2.54
ASI	1.06	1.15	1.02	1.23	1.17	1.05	1.05	1.18	0.90	1.04	0.97
Na/K	2.40	1.24	1.87	1.15	1.12	1.77	1.81	1.16	2.24	2.37	6.86
Al/K	6.73	5.06	4.90	4.77	4.48	4.49	4.85	4.20	5.75	8.11	21.21
Al/Na	2.80	4.08	2.62	4.14	4.02	2.53	2.68	3.60	2.57	3.42	3.09
Al/Si	0.12	0.10	0.10	0.10	0.09	0.09	0.10	0.07	0.11	0.14	0.22
Distance (μm)	647	456	294	353	353	177	74	15	15	15	15

	$F60_{top}$				M				$F60_{bottom}$
Analysis Spot	1	2	3	4	5	6	7	8	9
SiO_2	78.24	77.85	79.24	73.16	61.61	59.78	63.17	56.61	75.91
TiO_2	0.27	0.28	0.30	0.31	0.34	0.23	0.46	0.73	0.33
Al_2O_3	10.75	10.73	11.10	11.71	22.47	24.07	19.93	20.32	13.57
FeO_T	2.42	2.21	2.05	3.50	2.15	1.65	2.60	6.85	1.70
MnO	0.15	0.15	0.15	0.35	0.10	0.07	0.22	0.29	0.13
MgO	1.31	1.25	1.21	2.49	0.40	0.24	1.75	2.66	0.47
CaO	2.96	2.51	2.19	3.91	7.93	8.21	6.21	8.04	1.95
Na_2O	1.47	2.68	1.31	2.43	3.86	4.78	4.00	3.43	3.26
K_2O	2.42	2.36	2.44	2.13	1.11	0.92	1.65	1.06	2.68
H_2O	6.47	6.03	6.35	4.58	3.67	2.54	3.83	3.65	6.17
ASI	1.03	0.93	1.26	0.87	1.02	1.01	1.01	0.95	1.15
Na/K	0.92	1.73	0.82	1.74	5.26	7.90	3.69	4.91	1.85
Al/K	4.10	4.21	4.20	5.08	18.62	24.16	11.17	17.68	4.68
Al/Na	4.46	2.44	5.13	2.92	3.54	3.06	3.03	3.60	2.53
Al/Si	0.08	0.08	0.08	0.09	0.21	0.24	0.19	0.21	0.11
Distance (μm)	118	59	15	15	44	59	1162	118	15

F70-M	F70									M
Analysis Spot	1	2	3	4	5	6	7	8	9	10
SiO_2	77.54	78.69	73.74	72.09	72.21	71.76	70.03	71.16	70.83	65.54
TiO_2	0.35	0.35	0.59	0.61	0.61	0.54	0.56	0.61	0.60	0.67
Al_2O_3	12.12	12.10	14.42	14.67	15.06	14.93	15.87	15.91	15.96	17.78
FeO_T	1.72	1.78	2.43	2.37	2.60	2.37	2.53	2.53	2.62	3.05
MnO	0.10	0.11	0.18	0.21	0.21	0.20	0.21	0.23	0.23	0.36
MgO	0.65	0.60	0.98	1.08	1.18	1.14	1.25	1.21	1.35	1.94
CaO	1.89	2.02	2.88	2.97	3.35	2.99	3.41	3.66	3.71	4.33
Na_2O	3.29	1.92	2.36	3.74	2.38	3.72	3.84	2.40	2.40	4.09
K_2O	2.32	2.42	2.39	2.26	2.35	2.33	2.27	2.27	2.27	2.21
H_2O	4.11	6.23	6.67	5.25	6.96	5.55	5.68	6.83	6.61	6.27
ASI	1.07	1.28	1.23	1.05	1.20	1.06	1.06	1.22	1.21	1.05
Na/K	2.16	1.21	1.50	2.51	1.54	2.42	2.57	1.61	1.60	2.81
Al/K	4.83	4.62	5.56	5.99	5.92	5.91	6.45	6.47	6.48	7.42
Al/Na	2.24	3.83	3.71	2.39	3.85	2.44	2.51	4.03	4.04	2.64
Al/Si	0.09	0.09	0.12	0.12	0.12	0.12	0.13	0.13	0.13	0.16
Distance (μm)	442	375	58	58	58	58	47	58	15	1302

F80-M-F80	$F80_{bottom}$			M						
Analysis Spot	1	2	3	4	5	6	7	8	9	10
SiO_2	77.39	72.63	73.32	59.15	58.69	60.98	62.00	59.18	60.37	57.66
TiO_2	0.39	0.42	0.44	0.52	0.33	0.47	0.48	0.36	0.43	0.37
Al_2O_3	12.13	14.19	14.32	22.92	23.57	20.75	19.99	23.88	22.67	21.59
FeO_T	2.33	2.96	2.90	3.15	2.05	3.14	3.07	1.84	2.38	3.60
MnO	0.10	0.15	0.15	0.11	0.13	0.25	0.23	0.09	0.14	0.33
MgO	0.45	0.76	0.84	0.50	0.89	1.99	2.08	0.43	0.71	3.61
CaO	2.16	2.72	2.84	8.03	9.20	6.83	6.77	8.36	7.87	7.46
Na_2O	2.17	3.42	2.25	4.32	3.96	3.98	3.55	4.62	3.93	4.27
K_2O	2.85	2.74	2.88	1.28	1.13	1.60	1.81	1.23	1.48	1.07
H_2O	5.81	4.39	5.76	2.31	2.04	3.29	4.04	1.30	2.26	2.38
ASI	1.15	1.05	1.20	0.99	0.96	1.00	0.99	0.99	1.01	0.99
Na/K	1.16	1.90	1.19	5.15	5.32	3.77	2.98	5.69	4.03	6.08
Al/K	3.93	4.78	4.59	16.60	19.25	11.95	10.21	17.89	14.13	18.67
Al/Na	3.40	2.52	3.87	3.22	3.62	3.17	3.42	3.14	3.51	3.07
Al/Si	0.09	0.12	0.12	0.23	0.24	0.20	0.19	0.24	0.22	0.22
Distance (μm)	147	44	15	221	441	647	647	632	1205	1324

Table 4

F0-M																											
								F0											M								
Analysis Spot	1	2	3	4	5	6	7	8	9	10	11	12	13	14	15	16	17	18	19	20	21	22	23	24	25	26	27
TiO_2	0.29	0.30	0.30	0.30	0.17	0.31	0.35	0.38	0.31	0.30	0.29	0.25	0.60	0.39	0.35	0.36	0.37	0.35	0.37	0.34	0.35	0.33	0.34	0.35	0.32	0.32	0.32
FeO_t	1.61	2.33	1.67	1.73	1.17	1.64	1.58	1.56	1.83	2.32	1.75	1.40	4.61	1.70	1.71	1.73	1.75	1.74	1.93	2.03	1.95	1.81	1.95	2.04	1.66	1.62	1.58
MgO	0.74	1.82	0.80	0.83	0.41	0.79	0.83	0.85	1.03	1.66	0.96	0.61	2.81	0.94	0.93	0.94	0.94	0.92	1.05	1.14	1.12	1.09	1.12	1.06	1.05	1.06	1.02
CaO	2.44	4.32	2.58	2.63	5.55	2.51	2.58	2.61	3.05	4.75	3.44	4.23	4.89	2.81	2.79	2.84	2.86	2.79	3.08	3.22	3.24	3.22	3.31	3.21	3.18	3.27	2.99
H_2O	5.51	4.65	5.71	5.62	2.44	5.44	5.49	5.82	6.01	4.57	5.41	4.18	4.66	5.87	5.82	5.85	6.10	5.69	6.39	6.86	7.07	7.21	6.70	6.76	6.63	7.10	7.45
Li	2.43	2.23	2.50	2.50	1.38	2.42	2.47	2.59	2.62	2.14	2.36	1.81	2.19	2.51	2.49	2.50	2.52	2.53	2.62	2.68	2.83	2.85	2.87	2.97	2.88	3.07	3.27
B	13.38	11.59	13.48	14.02	6.80	15.27	21.00	24.53	15.10	12.74	14.13	12.95	27.39	28.21	19.45	20.85	22.21	18.79	29.08	36.89	39.06	40.56	38.77	39.05	38.23	38.23	38.43
FeO_t/MgO	2.17	1.28	2.09	2.10	2.84	2.07	1.91	1.84	1.77	1.40	1.82	2.29	1.64	1.82	1.83	1.85	1.85	1.90	1.84	1.79	1.74	1.66	1.74	1.93	1.58	1.53	1.55
Distance (µm)	593	556	370	296	222	37	19	37	10	10	93	10	278	93	130	296	407	259	704	1148	1611	2963	2407	2355	2444	3296	3963

F0-M-F0							$F0_{top}$							M					$F0_{bottom}$				
Analysis Spot	1	2	3	4	5	6	7	8	9	10	11	12	13	14	15	16	17	18	19	20	21	22	23
TiO_2	0.23	0.26	0.19	0.14	0.22	0.27	0.31	0.11	0.13	0.22	0.30	0.21	0.26	0.22	0.19	0.22	0.32	0.23	0.22	0.32	0.30	0.24	0.31
FeO_t	1.14	1.33	1.08	1.08	1.11	1.13	1.20	1.03	1.10	1.09	1.24	1.16	1.43	1.90	2.32	1.18	1.43	1.22	1.32	1.32	1.20	1.09	1.11
MgO	0.64	0.84	0.55	0.59	0.57	0.63	0.63	0.50	0.59	0.50	0.64	0.51	1.29	1.04	2.88	0.43	0.62	0.46	0.95	0.72	0.61	0.59	0.58
CaO	1.95	1.92	2.97	1.88	2.49	1.90	1.96	2.83	1.88	3.77	2.05	3.53	2.13	4.46	5.50	3.94	1.97	3.69	3.43	1.92	1.97	1.87	1.88
H_2O	5.31	5.10	4.46	4.70	4.74	5.46	4.99	4.75	5.30	4.15	5.31	4.07	5.07	4.52	3.06	4.13	5.75	4.38	5.13	5.92	6.61	6.04	5.68
Li	5.30	5.12	4.68	5.21	4.93	5.15	4.96	4.47	5.05	4.07	5.05	4.17	4.60	3.76	3.00	3.73	4.77	3.80	4.06	4.93	4.75	4.70	4.78
B	15.03	22.73	12.15	14.52	13.00	16.24	18.15	12.71	23.54	22.26	25.37	20.85	23.49	41.33	28.19	25.92	32.68	19.15	22.32	29.58	34.47	25.84	19.81
FeO_t/MgO	1.77	2.07	1.96	1.82	1.94	1.79	1.90	2.06	1.86	2.18	1.94	2.29	1.12	1.83	0.80	2.72	2.30	2.64	1.40	1.84	1.97	1.86	1.92
Distance (µm)	2226	1677	1823	1548	887	677	516	387	15	10	81	65	113	532	484	177	258	194	161	307	161	145	629

F50-M												F50													M						
Analysis Spot	1	2	3	4	5	6	7	8	9	10	11	12	13	14	15	16	17	18	19	20	21	22	23	24	25	26	27	28	29	30	31	32	33	34	35
TiO_2	0.12	0.10	0.13	0.11	0.13	0.15	0.19	0.28	0.21	0.22	0.22	0.21	0.12	0.25	0.25	0.29	0.24	0.27	0.28	0.27	0.21	0.49	0.27	0.47	0.74	1.32	0.37	0.32	1.88	0.36	0.34	0.38	0.36	0.36	0.83
FeO_t	1.16	0.94	1.21	1.08	1.15	1.36	1.28	1.90	1.33	1.27	1.32	1.34	1.11	1.31	1.41	1.59	0.00	1.56	1.57	1.44	1.16	4.62	1.50	1.93	4.31	10.71	2.02	2.06	22.38	2.13	1.92	1.83	1.89	1.73	4.98
MgO	0.55	0.30	0.41	0.35	0.60	0.38	0.43	0.84	0.47	0.49	0.46	0.45	0.22	0.55	0.51	0.59	0.47	0.67	0.64	0.56	0.33	0.59	0.57	0.87	0.97	1.15	0.94	0.98	2.44	1.29	1.05	1.18	1.13	1.05	4.89
CaO	1.75	1.23	1.72	1.30	1.67	1.84	1.93	4.29	2.91	2.65	2.00	1.93	0.95	1.92	2.01	2.34	1.81	2.16	2.87	2.08	1.20	4.66	2.22	2.84	2.86	2.67	2.86	2.92	7.89	3.20	3.09	3.10	3.09	3.04	5.88
H_2O	4.78	4.24	4.27	5.50	5.74	5.29	5.87	4.32	5.37	6.30	6.01	6.06	5.77	6.44	6.15	5.99	7.48	6.26	6.62	6.31	6.12	4.41	7.19	6.42	6.79	6.56	7.56	7.29	7.56	7.44	8.01	8.16	8.42	8.31	5.65
Li	1.80	0.76	2.08	2.21	2.03	3.38	3.64	3.07	3.38	3.72	3.56	3.65	2.58	3.76	3.71	4.00	3.45	3.65	3.73	3.77	2.65	3.18	4.05	4.16	4.18	4.61	4.42	4.41	4.73	4.56	4.58	4.82	4.78	4.79	4.75
B	5.69	4.11	6.91	5.73	5.77	8.70	8.57	8.44	9.25	9.94	8.90	9.30	4.94	13.06	14.37	16.72	12.94	13.75	14.62	14.91	11.76	13.18	14.70	36.99	45.13	39.15	45.71	44.17	41.94	42.02	43.89	43.30	41.22	41.94	31.44
FeO_t/MgO	2.11	3.12	2.95	3.04	1.92	3.62	2.97	2.27	2.83	2.60	2.88	3.00	4.99	2.38	2.76	2.69	0.00	2.33	2.46	2.58	3.46	7.80	2.66	2.22	4.45	9.28	2.15	2.10	9.17	1.65	1.82	1.55	1.67	1.65	1.02
Distance (µm)	1273	1127	836	964	836	418	473	400	282	209	164	409	10	10	10	55	10	10	18	18	55	10	73	182	309	200	455	665	1091	1327	1527	1873	1982	2290	2464

F60-M-F60							$F60_{top}$							M				$F60_{bottom}$			
Analysis Spot	1	2	3	4	5	6	7	8	9	10	11	12	13	14	15	16	17	18	19	20	21
TiO_2	0.16	0.14	0.17	0.15	0.14	0.19	0.17	0.14	0.14	0.15	0.14	0.14	0.67	0.21	0.77	0.15	0.15	0.13	0.25	0.10	0.11
FeO_t	1.77	1.35	1.11	1.11	1.04	1.12	0.92	0.99	1.15	0.90	1.00	1.28	5.40	0.94	7.75	0.71	0.71	0.78	1.42	1.01	0.81
MgO	1.61	0.98	0.51	0.55	0.45	0.31	0.23	0.40	0.54	0.35	0.37	0.62	0.38	0.41	5.38	0.23	0.23	0.32	0.59	0.60	0.24
CaO	3.16	1.97	1.71	1.98	1.55	1.49	1.39	1.51	1.60	1.50	1.32	1.56	3.88	1.88	6.90	1.13	1.15	0.93	1.68	1.81	1.27
H_2O	5.40	4.64	6.33	6.36	6.33	6.63	7.04	6.80	6.78	7.20	6.72	6.83	5.24	7.92	5.80	6.97	7.65	5.83	5.02	6.10	6.28
Li	6.21	3.57	5.41	6.41	5.95	6.45	6.86	6.12	6.00	7.27	5.07	6.07	6.75	10.29	7.07	6.99	7.22	4.72	6.47	6.25	5.73
B	11.80	7.01	11.90	7.52	8.17	7.58	8.04	6.92	6.31	12.38	6.74	7.51	42.22	48.00	33.65	33.01	28.29	15.87	11.57	11.23	9.89
FeO_t/MgO	1.10	1.37	2.18	2.03	2.29	3.62	4.05	2.50	2.13	2.57	2.73	2.05	14.02	2.30	1.44	3.12	3.09	2.48	2.40	1.69	3.42
Distance (µm)	1500	1206	882	721	412	500	294	206	132	10	177	74	485	1485	662	10	29	309	427	1191	1485

F70-M									F70										M												
Analysis Spot	1	2	3	4	5	6	7	8	9	10	11	12	13	14	15	16	17	18	19	20	21	22	23	24	25	26	27	28	29	30	31
TiO_2	0.18	0.16	0.17	0.16	0.12	0.20	0.29	0.22	0.21	0.30	0.32	0.28	0.32	0.38	0.29	0.25	0.20	0.25	0.51	0.41	0.40	0.43	0.38	0.40	0.74	0.36	0.37	0.37	0.37	0.39	0.47
FeO_t	1.10	0.95	0.95	0.96	1.02	1.13	1.36	3.08	1.85	2.00	1.36	1.23	1.30	1.77	1.34	1.25	1.29	1.19	2.24	1.72	1.74	1.70	1.64	1.58	4.56	1.73	1.79	1.79	1.97	1.62	3.36
MgO	0.30	0.28	0.32	0.28	0.23	0.47	0.86	0.91	1.07	0.65	0.68	0.56	0.64	0.74	0.67	0.61	0.87	0.63	1.62	1.13	1.04	1.19	0.96	0.98	3.92	1.08	1.13	1.13	1.13	1.08	1.16
CaO	1.37	1.18	1.24	1.00	0.69	1.24	2.15	6.79	5.56	3.84	2.25	1.84	2.10	2.38	2.34	2.03	2.18	2.14	4.23	2.91	2.90	2.93	2.91	2.78	5.14	3.00	3.14	3.14	3.31	3.13	3.29
H_2O	3.88	5.31	5.93	5.61	7.11	6.06	5.77	2.91	3.49	5.25	6.02	6.11	5.87	5.98	5.86	6.62	6.39	5.66	5.38	6.59	6.63	6.54	6.67	6.32	5.60	7.18	7.29	7.29	7.66	7.48	7.24
Li	3.22	4.29	4.65	4.55	3.81	4.97	5.99	3.98	4.61	6.12	6.33	6.21	6.51	6.90	4.84	2.91	5.59	6.66	6.34	7.22	7.40	7.31	7.24	7.31	6.14	7.53	8.07	8.07	7.89	8.05	7.89
B	12.27	8.36	9.91	9.42	9.81	13.41	19.79	19.09	26.74	21.86	22.80	19.56	23.54	26.44	24.04	22.71	14.86	17.26	34.90	43.43	44.47	44.87	42.79	45.27	38.55	40.04	38.88	38.88	39.56	46.50	48.69
FeO_t/MgO	3.69	3.32	2.99	3.41	4.37	2.40	1.58	3.37	1.73	3.09	1.99	2.19	2.02	2.39	1.99	2.03	1.48	1.89	1.38	1.52	1.67	1.42	1.71	1.60	1.16	1.60	1.58	1.58	1.73	1.50	2.90
Distance (µm)	628	581	419	326	186	70	58	15	47	70	70	70	116	47	35	15	35	35	116	256	314	209	279	302	314	954	1209	1593	2535	2512	2530

F80-M-F80					$F80_{top}$				$F80_{bottom}$			
Analysis Spot	1	2	3	4	5	6	7	8				
TiO_2	0.18	0.19	0.22	0.26	0.16	0.29	0.22	0.16				
FeO_t	1.28	1.05	1.12	1.19	1.24	1.60	1.26	1.50				
MgO	0.28	0.28	0.30	0.38	0.28	0.42	0.27	0.25				
CaO	1.51	1.42	1.18	1.43	5.23	1.72	5.62	2.22				
H_2O	3.38	3.58	4.37	4.38	2.67	4.82	2.22	3.59				
Li	7.08	5.69	10.25	11.77	7.86	11.24	7.57	7.46				
B	11.71	9.96	16.52	27.57	12.97	28.77	16.84	8.79				
FeO_t/MgO	4.54	3.74	3.71	3.11	4.38	3.86	4.71	6.03				
Distance (µm)	1309	1000	59	29	29	59	10	1735				

F50-F0					F50				F0				
Analysis Spot	1	2	3	4	5	6	7	8	9	10	11	12	13
TiO_2	0.11	0.11	0.12	0.11	0.11	0.18	0.12	0.19	0.61	0.75	0.25	0.28	0.29
FeO_t	0.85	0.82	0.85	1.18	0.76	1.08	0.99	1.17	4.46	5.35	1.48	1.45	1.20
MgO	0.32	0.32	0.33	0.34	0.25	0.31	0.27	0.29	0.98	0.50	0.63	0.36	0.34
CaO	1.20	1.21	1.22	1.45	0.92	1.22	1.07	1.19	1.22	1.27	2.78	2.51	1.66
H_2O	3.10	3.19	3.18	3.14	2.30	2.93	2.79	2.97	3.08	3.32	3.10	3.12	3.55
Li	5.75	5.59	5.39	5.92	3.77	4.79	2.41	3.40	5.57	6.03	5.64	5.75	6.17
B	8.76	9.80	11.04	8.17	6.71	13.02	10.20	28.98	16.56	17.45	13.68	14.41	16.11
FeO_t/MgO	2.66	2.55	2.60	3.49	3.04	3.48	3.68	4.06	4.56	10.78	2.36	3.98	3.54
Distance (µm)	3559	3088	2618	2000	735	235	147	29	250	500	1088	1956	2632

M-M						M_{top}						M_{bottom}				
Analysis Spot	1	2	3	4	5	6	7	8	9	10	11	12	13	14	15	16
TiO_2	0.34	0.38	0.51	0.30	0.60	0.39	0.50	0.55	0.37	0.42	0.40	0.35	0.38	0.36	0.34	0.50
FeO_t	2.73	3.06	4.08	2.68	4.98	3.34	3.19	3.26	2.81	3.04	3.00	2.78	2.97	2.77	2.73	3.71
MgO	1.53	1.61	2.54	1.50	3.28	1.70	1.67	1.69	1.52	1.52	1.49	1.49	1.47	1.42	1.39	2.65
CaO	4.00	4.77	4.84	4.21	5.42	4.22	4.72	4.01	3.82	3.84	3.83	3.85	3.84	3.76	3.83	4.62
H_2O	6.47	6.33	6.10	6.75	5.75	6.44	6.86	6.98	6.78	6.94	6.85	6.88	6.93	7.04	6.85	6.32
Li	2.27	2.32	2.11	2.15	2.10	2.12	2.08	2.14	2.24	2.20	2.13	2.12	2.14	2.30	2.16	1.96
B	35.15	36.02	32.81	33.10	31.79	37.29	46.67	56.77	38.69	53.49	51.55	38.53	50.11	49.09	37.09	40.28
FeO_t/MgO	1.79	1.90	1.60	1.79	1.52	1.97	1.91	1.93	1.84	2.00	2.01	1.86	2.02	1.95	1.96	1.40
Distance (µm)	5185	5074	4796	4444	4296	3482	2074	1111	37	74	148	185	185	444	833	704

Table SM 1

Element Profile 1				Element Profile 2			
Analysis Spot	SiO_2	Al_2O_3	CaO	Analysis Spot	SiO_2	Al_2O_3	CaO
1	89.85	3.65	0.55	1	75.82	9.07	1.52
2	98.14	0.20	0.13	2	76.05	9.77	1.41
3	98.14	0.20	0.13	3	73.93	10.81	1.20
4	80.15	8.03	1.18	4	76.73	10.05	1.42
5	79.96	7.84	1.33	5	77.44	9.21	1.41
6	98.14	0.20	0.13	6	77.28	9.79	1.25
7	98.14	0.20	0.13	7	76.31	9.53	1.40
8	80.47	9.07	1.49	8	76.79	9.93	1.19
9	77.32	9.65	1.12	9	76.26	10.07	1.42
10	78.64	8.37	1.25	10	74.99	9.48	1.29
11	79.03	8.24	1.46	11	75.40	8.88	1.20
12	85.80	5.32	1.04	12	75.77	9.67	1.68
13	89.49	4.89	0.89	13	76.11	8.79	1.49
14	97.08	0.32	0.11	14	75.81	10.47	1.22
15	76.19	9.45	1.36	15	75.42	8.45	1.32
16	72.99	9.43	1.35	16	74.75	10.13	1.44
17	76.37	7.62	1.29	17	78.20	8.00	1.33
18	73.24	9.40	1.28	18	78.22	9.62	1.55
19	77.58	9.78	1.15	19	79.13	9.85	1.45
20	75.42	9.88	1.20	20	78.04	9.29	1.25
21	76.74	8.94	1.23	21	74.89	9.31	1.39
22	83.07	6.88	0.96	22	78.47	9.91	1.46
23	98.65	0.36	0.04	23	76.14	8.94	1.48
24	98.14	0.20	0.13	24	74.08	8.90	1.42
25	75.53	9.75	1.31	25	78.15	9.30	1.28
26	77.47	8.57	1.29	26	77.38	8.72	1.67
27	77.15	9.64	1.34	27	78.32	9.74	1.36
28	79.32	9.80	1.43	28	75.70	9.76	1.44
29	75.85	8.63	1.48	29	78.14	10.22	1.48
30	76.01	8.56	1.11	30	77.84	10.19	1.32
31	79.71	8.92	1.16	31	73.76	9.03	1.40
32	77.10	9.98	1.25	32	76.04	9.51	1.47
33	80.62	7.61	1.35	33	76.92	10.33	1.31
34	96.94	1.03	0.34	34	75.55	10.94	1.35
35	98.14	0.20	0.13	35	73.30	8.61	1.65
36	76.36	9.62	1.13	36	74.61	9.45	1.51
37	74.33	9.91	1.33	37	74.80	9.23	1.46
38	76.64	9.58	1.39	38	78.07	9.46	1.52
39	75.27	10.62	1.10	39	74.96	9.06	1.44
40	76.90	10.40	1.40	40	75.80	9.68	1.31
41	75.84	9.04	1.38	41	76.25	8.97	1.20
42	76.40	8.44	1.18	42	76.61	8.89	1.25
43	78.34	9.02	1.36	43	73.99	9.32	1.30
44	74.26	9.23	1.11	44	75.65	8.85	1.40
45	76.18	9.33	1.26	45	79.22	10.48	1.29
46	77.13	9.37	1.24	46	74.23	9.15	1.21
47	79.43	7.25	1.06	47	78.22	8.82	1.31
48	73.69	9.01	1.50	48	76.45	9.10	1.32
49	76.85	9.81	1.42	49	78.71	9.26	1.23
50	77.38	10.13	1.47	50	76.71	9.03	1.21
51	74.34	10.17	1.29	51	75.67	10.29	1.50
52	75.44	8.78	1.25	52	77.18	9.55	1.25
53	75.30	9.52	1.43	53	75.05	9.68	1.39
54	77.58	9.46	1.24	54	77.28	8.91	1.32
55	77.39	9.69	1.16	55	78.17	9.71	1.50
56	79.14	9.32	1.43	56	75.61	9.61	1.53
57	77.14	9.85	1.27	57	75.69	9.18	1.59
58	77.27	7.98	1.34	58	76.08	10.06	1.14
59	75.75	10.28	1.34	59	78.44	9.68	1.25
60	75.02	8.72	1.72	60	79.14	8.44	1.31
61	75.49	9.88	1.62	61	76.88	10.02	1.30
62	75.63	8.50	1.59	62	76.90	11.13	1.27
63	74.98	9.64	1.35	63	77.99	9.37	1.18
64	75.10	8.91	1.52	64	77.29	8.60	1.28
65	75.03	9.68	1.27	65	78.01	10.34	1.10
66	77.62	9.31	1.24	66	75.64	9.71	1.19
67	75.25	8.67	1.44	67	76.69	9.62	1.35
68	79.35	8.80	1.44	68	78.76	9.23	1.47
69	74.64	9.35	1.41	69	77.09	8.35	0.96
70	74.39	10.59	1.38	70	77.30	9.23	1.47
71	75.72	9.95	1.42	71	75.34	9.23	1.34
72	76.64	8.81	1.29	72	77.92	9.56	1.44
73	75.48	10.33	1.38	73	77.22	9.27	1.19
74	76.76	9.88	1.42	74	75.75	9.65	1.34
75	74.20	9.24	1.38	75	76.72	9.46	1.24
76	80.24	8.65	1.45	76	77.43	8.07	1.45
77	76.80	9.81	1.32	77	78.15	9.31	1.51
78	76.56	8.13	1.48	78	75.27	9.47	1.17
79	75.45	8.56	1.43	79	74.71	10.30	1.32
80	75.32	10.42	1.12	80	76.21	9.70	1.22
81	73.24	8.60	1.64	81	74.94	9.50	1.38
82	74.70	10.08	1.30	82	75.14	9.46	1.44
83	76.76	9.75	1.49	83	77.06	9.34	1.20
84	74.75	9.60	1.47	84	76.70	7.34	1.40
85	74.39	8.92	1.37	85	75.42	8.67	1.29
86	77.44	9.47	1.02	86	77.06	9.32	1.45
87	73.33	9.41	1.38	87	76.25	9.88	1.34
88	76.69	9.56	1.62	88	76.30	8.20	1.10
89	74.12	10.30	1.29	89	77.75	8.46	1.03
90	75.76	10.63	1.38	90	94.07	3.30	0.62
91	76.36	8.80	1.37	91	98.14	0.20	0.13
92	79.96	10.35	1.42	92	98.14	0.20	0.13
93	77.01	10.23	1.32	93	98.14	0.20	0.13
94	76.47	9.80	1.38	94	90.41	4.92	0.52
				95	77.66	7.67	1.16
				96	79.94	9.79	1.37
				97	78.42	9.02	1.20
				98	77.91	10.79	1.57
				99	75.37	9.28	1.15
				100	77.60	9.53	1.10
				101	75.90	8.92	1.39
				102	75.16	8.38	1.80
				103	78.77	10.12	1.09
				104	78.21	8.05	0.93
				105	76.23	9.35	1.26
				106	75.28	7.85	1.10
				107	76.84	8.92	1.25
				108	89.44	3.79	0.80
				109	98.14	0.20	0.13
				110	98.14	0.20	0.13
				111	98.14	0.20	0.13
				112	98.14	0.20	0.13
				113	98.14	0.20	0.13
				114	98.14	0.20	0.13
				115	95.39	2.83	0.29
				116	74.49	9.07	1.15
				117	75.26	8.48	1.32
				118	76.42	9.59	1.39
				119	76.47	8.29	1.31
				120	98.14	0.20	0.13
				121	98.14	0.20	0.13
				122	99.97	0.06	0.07
				123	98.14	0.20	0.13
				124	98.14	0.20	0.13
				125	98.14	0.20	0.13

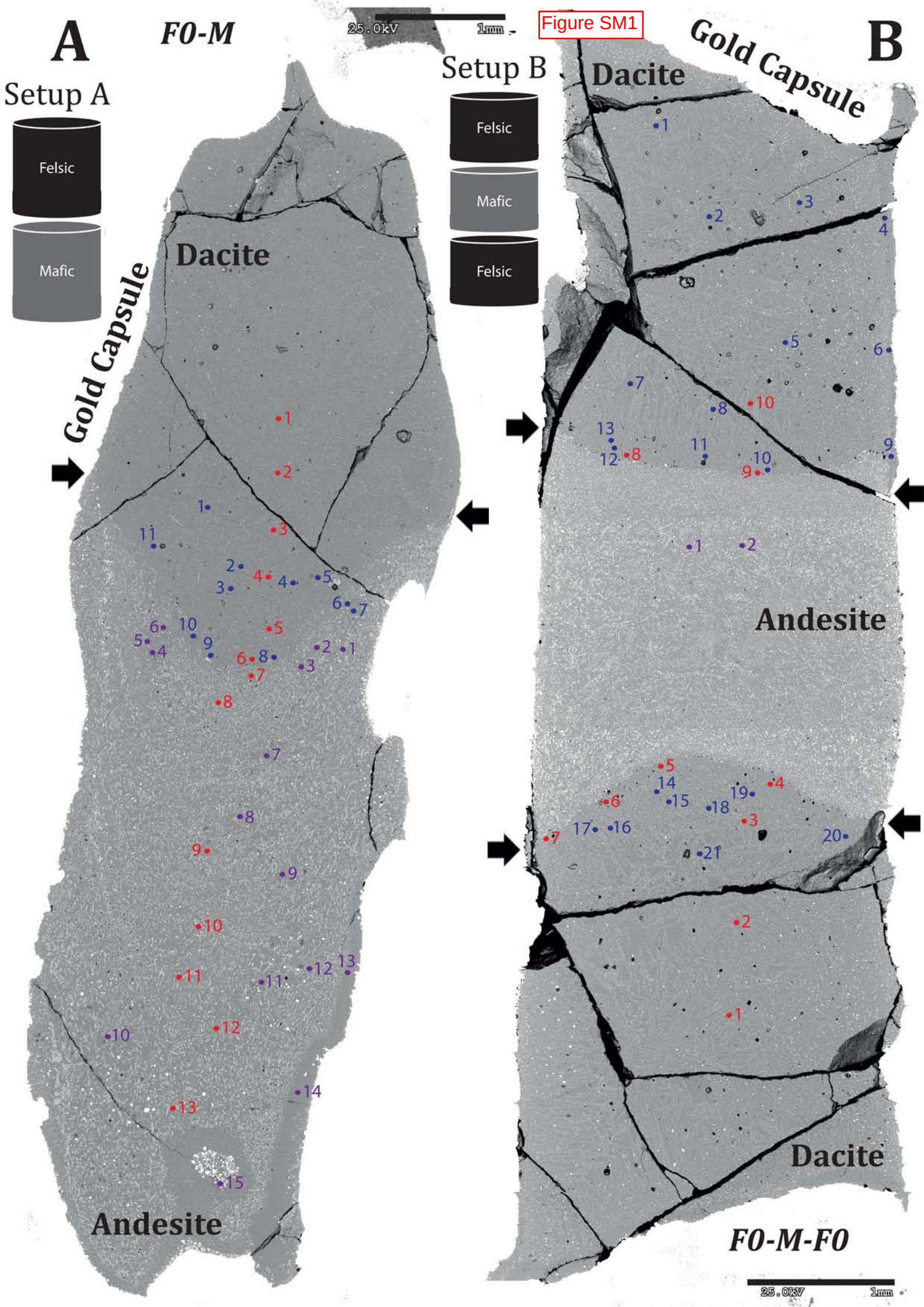
Figure SM1
A
F0-M
25.0kV
1mm
Setup A
Felsic
Mafic
Dacite
Gold Capsule
Andesite
B
Setup B
Felsic
Mafic
Felsic
Dacite
Gold Capsule
Andesite
Dacite
F0-M-F0
25.0kV
1mm

Figure SM1 cont'

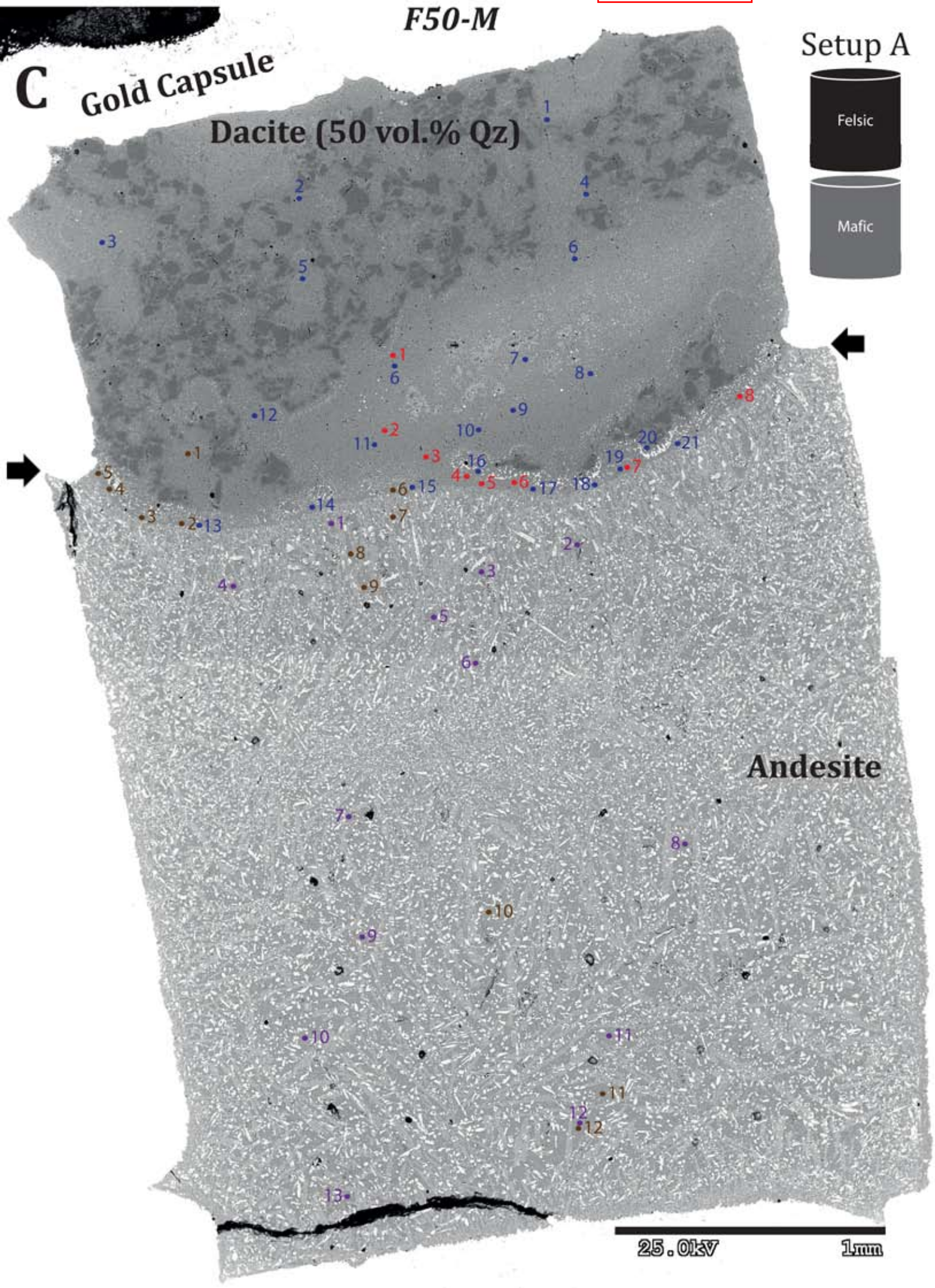

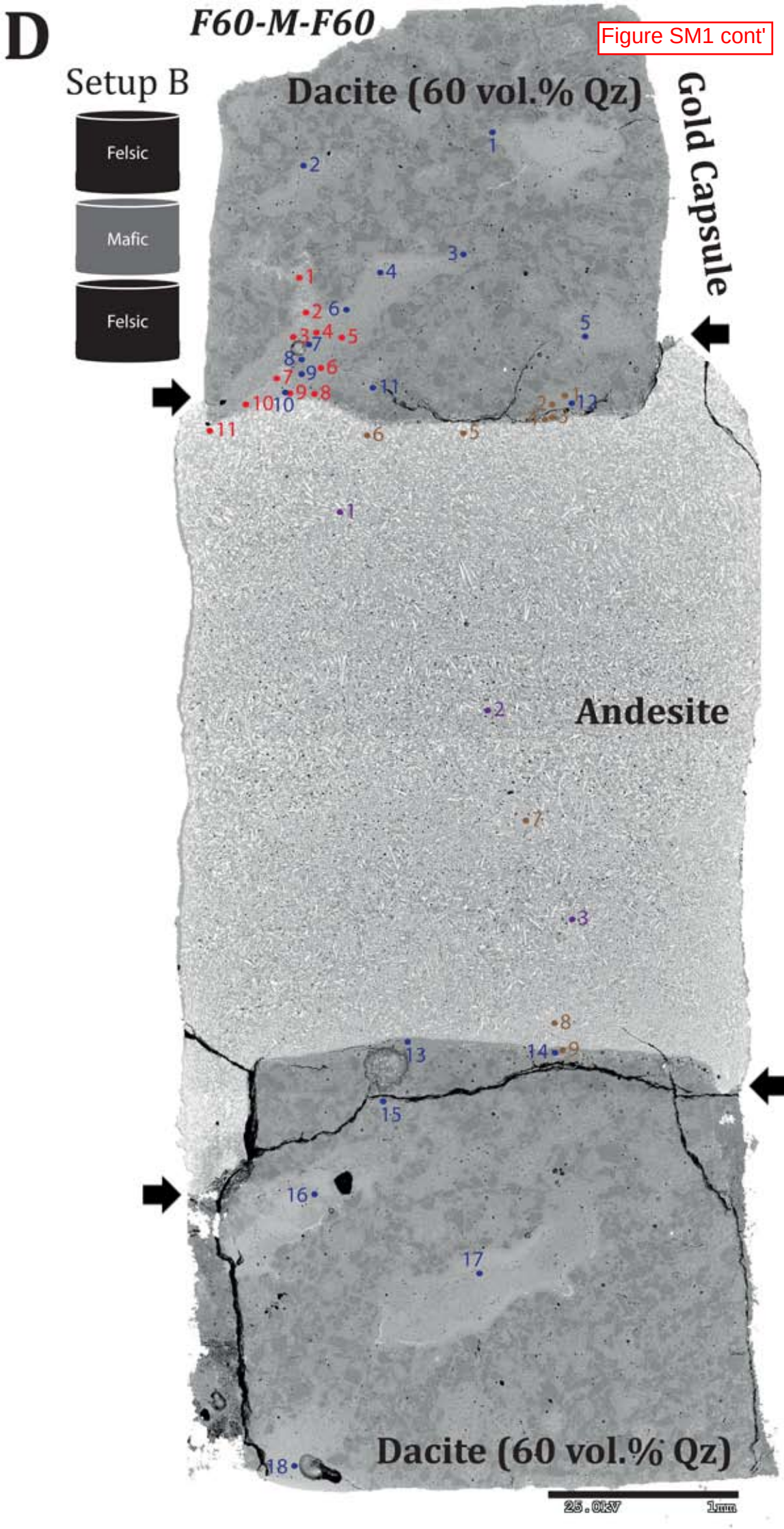
D
F60-M-F60
Figure SM1 cont'
Setup B
Felsic
Mafic
Felsic
Dacite (60 vol.% Qz)
Gold Capsule
Andesite
Dacite (60 vol.% Qz)
25.037
1mm

Figure SM1 cont'

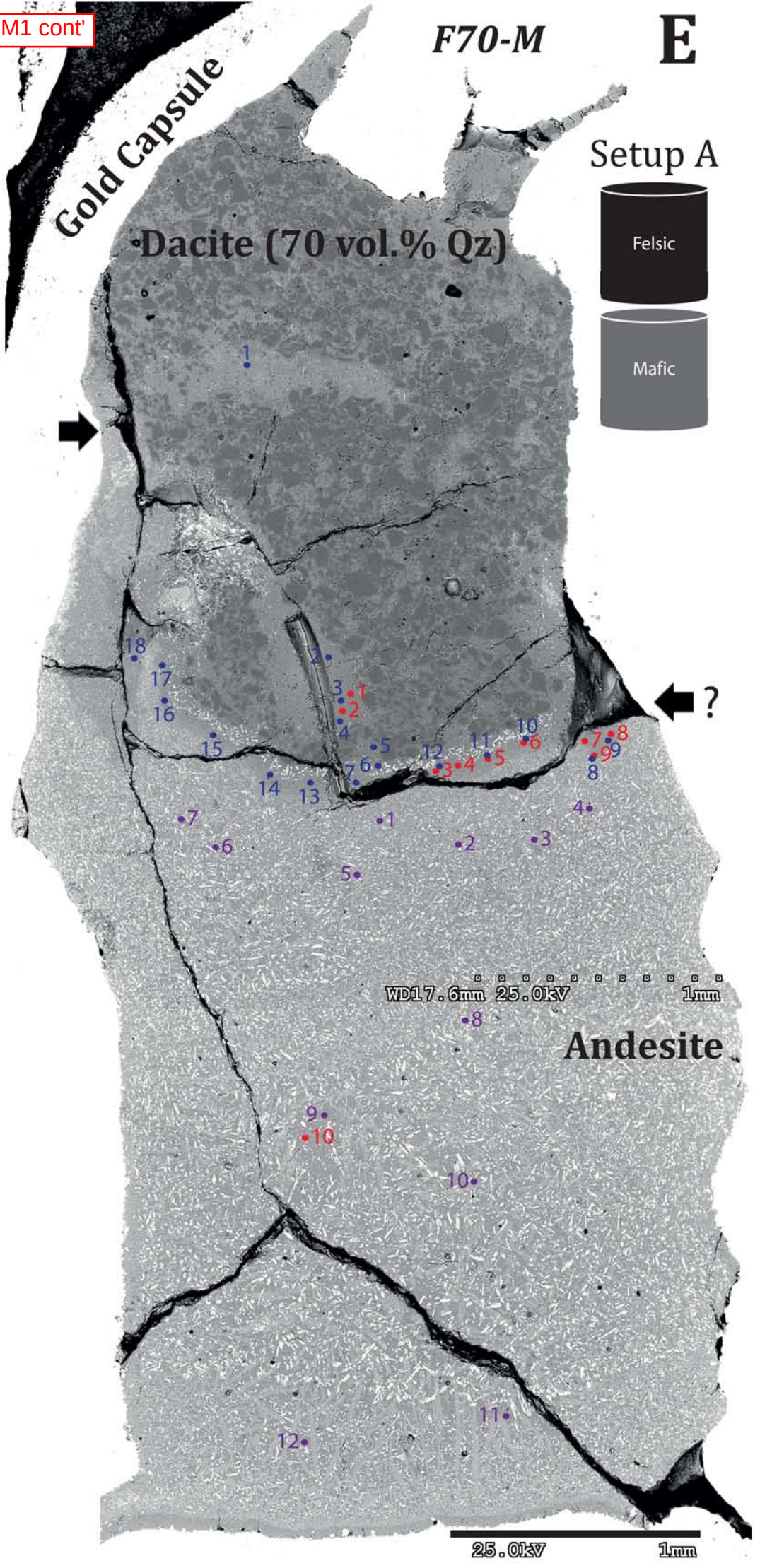

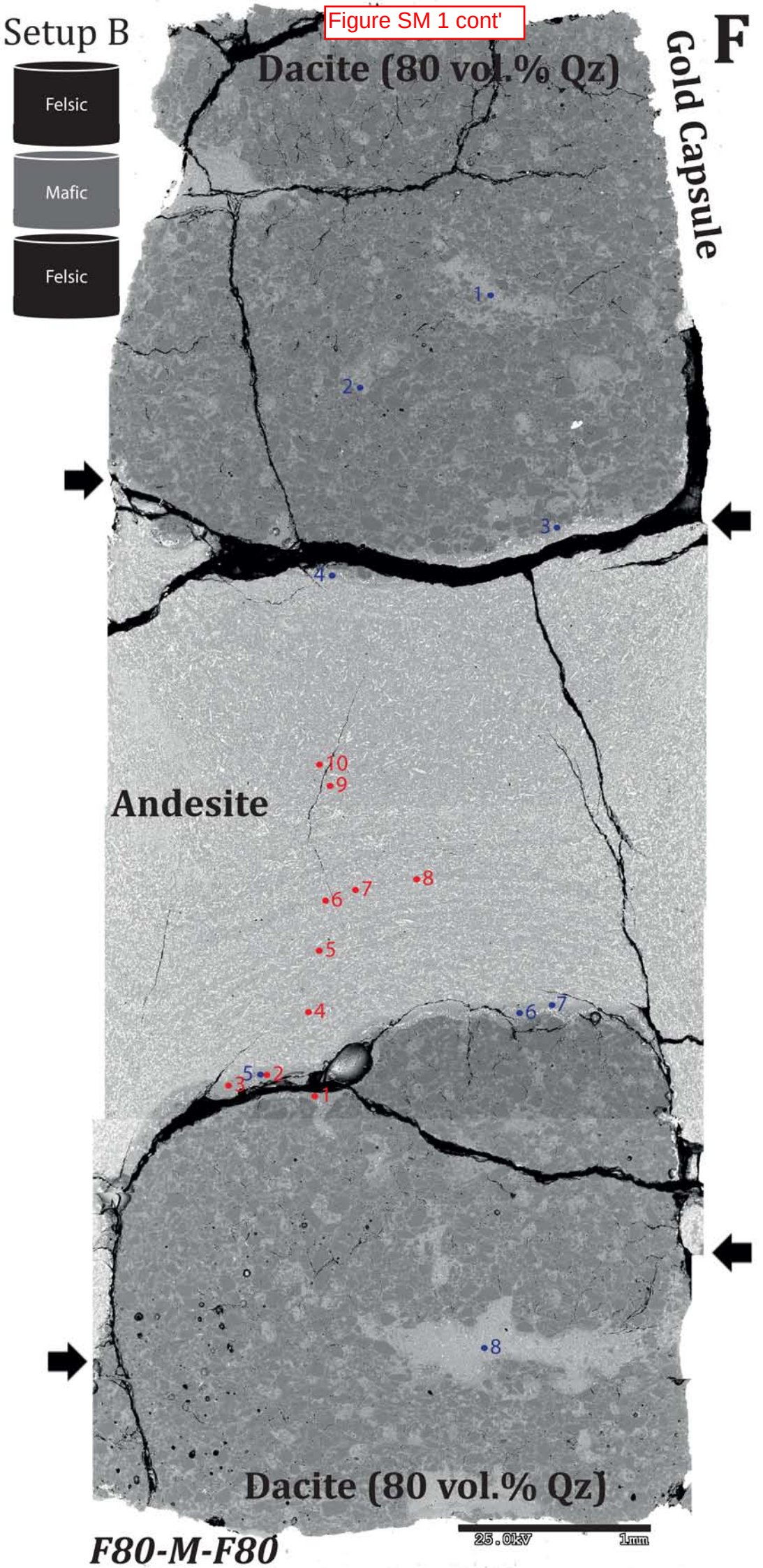
Figure SM 1 cont'
Setup B
Felsic
Mafic
Felsic
Dacite (80 vol.% Qz)
F
Gold Capsule
1
2
3
4
Andesite
10
9
8
7
6
5
4
6
7
5
2
3
1
8
Dacite (80 vol.% Qz)
F80-M-F80
25.0kV
1mm

Figure SM 1 cont'

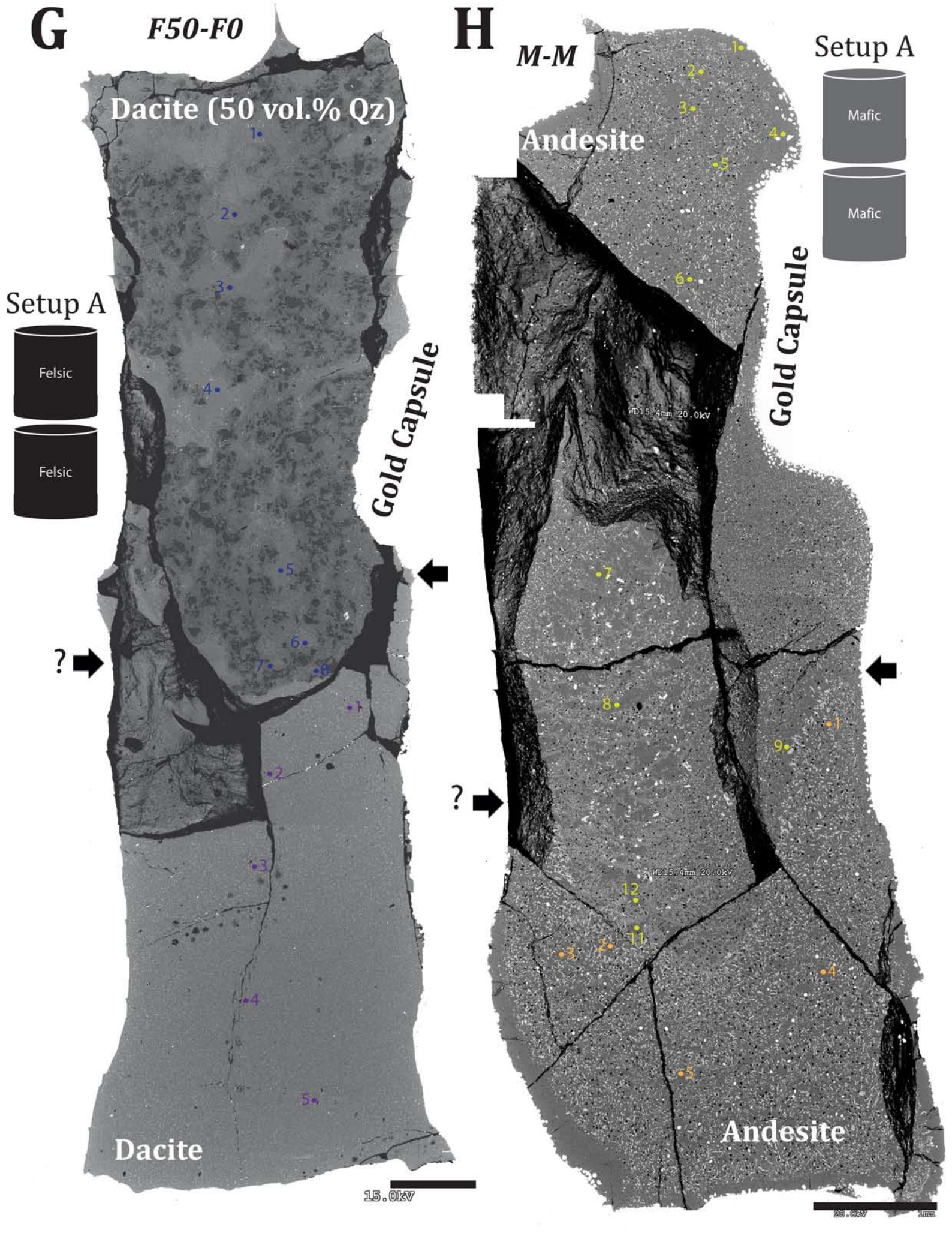

Figure SM 1 cont'

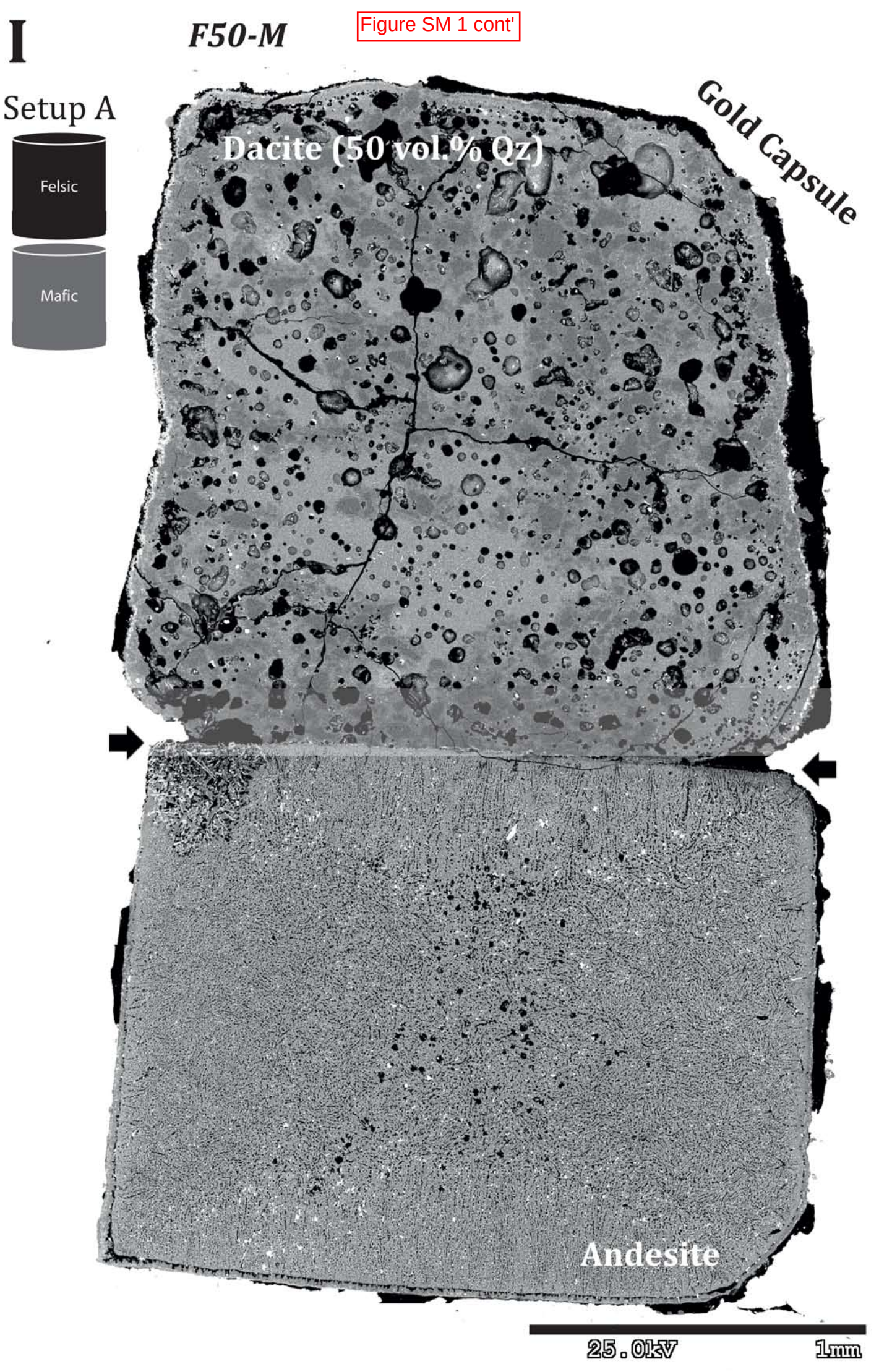

Figure SM 2

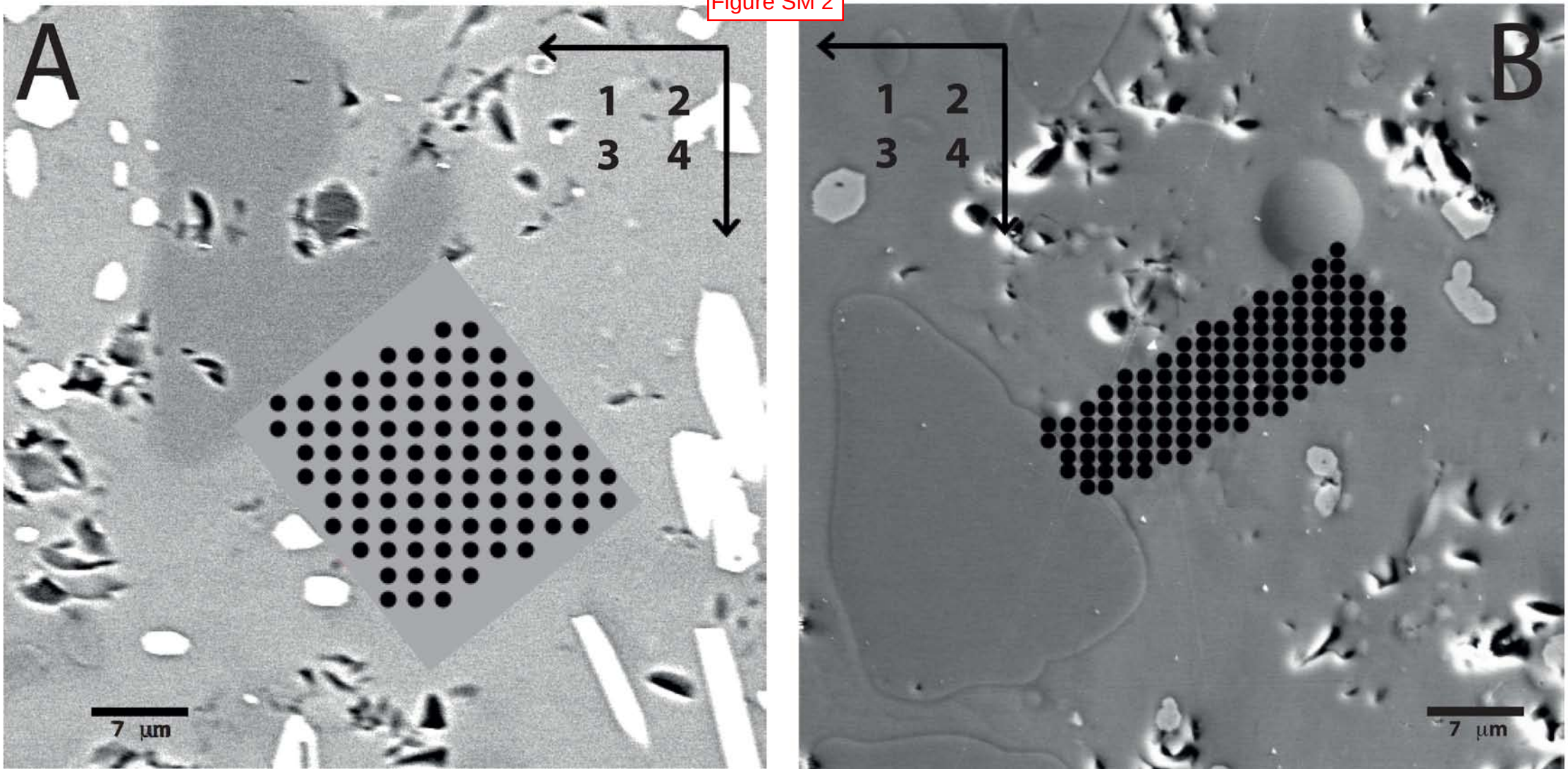

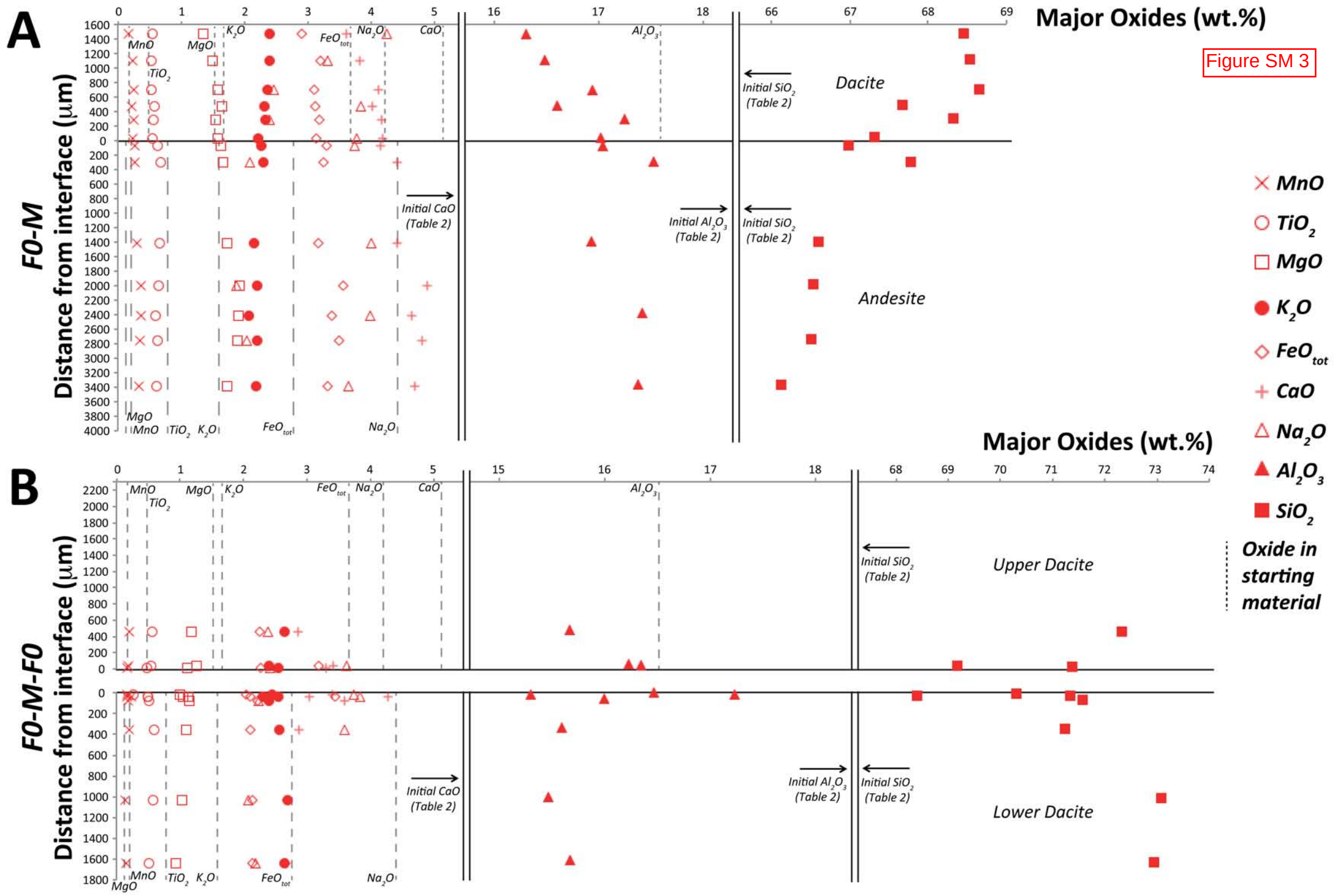
A
F0-M
Distance from interface (μm)
Major Oxides (wt.%)
Figure SM 3
MnO
MgO
K2O
FeOtot
Na2O
CaO
TiO2
Al2O3
SiO2
Initial CaO (Table 2)
Initial Al2O3 (Table 2)
Initial SiO2 (Table 2)
Dacite
Andesite
B
F0-M-F0
Upper Dacite
Lower Dacite
Oxide in starting material

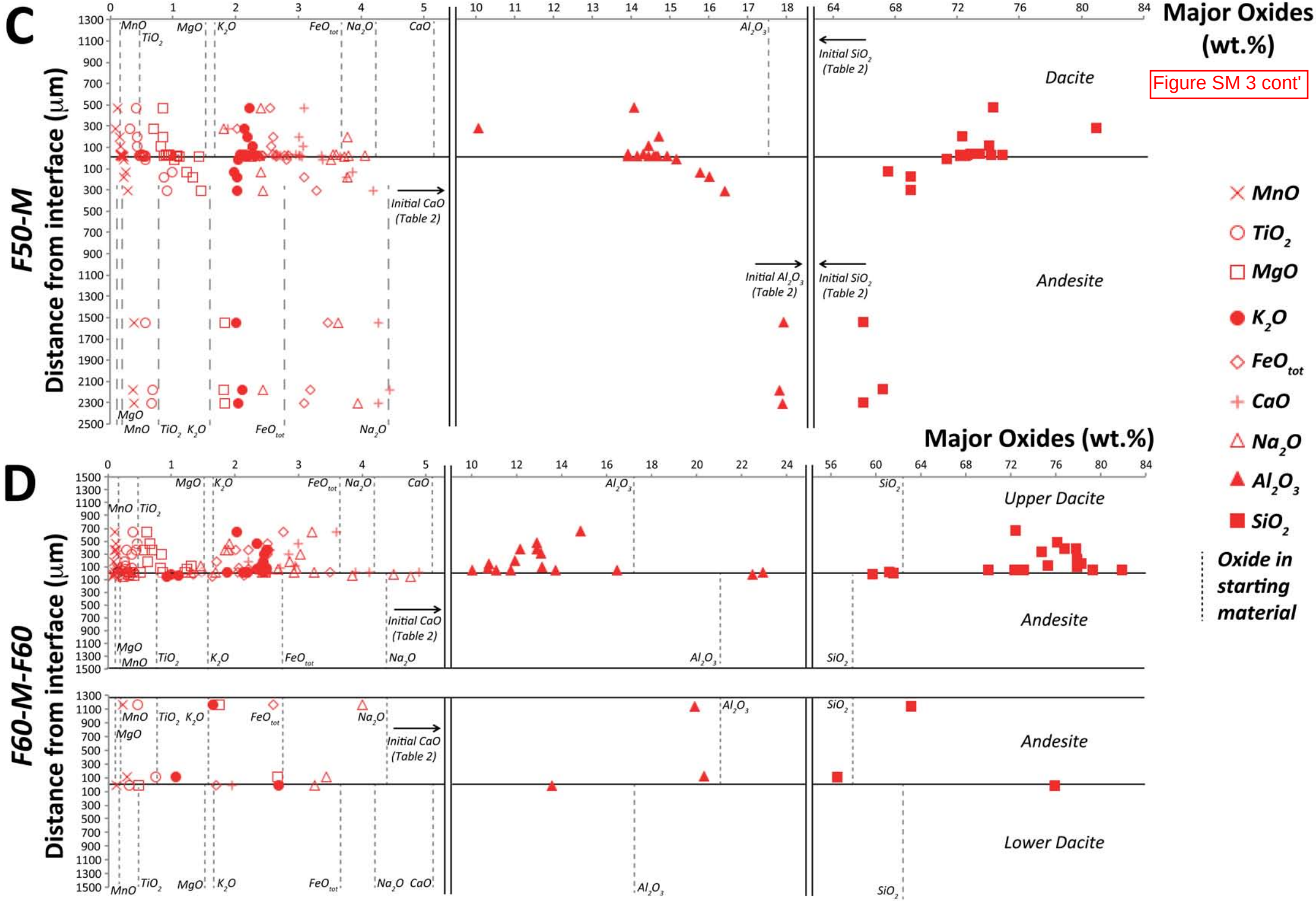
C
F50-M
Distance from interface (μm)
Major Oxides (wt.%)
Figure SM 3 cont'
MnO
TiO2
MgO
K2O
FeOtot
Na2O
CaO
Al2O3
SiO2
Initial CaO (Table 2)
Initial SiO2 (Table 2)
Initial Al2O3 (Table 2)
Dacite
Andesite
D
F60-M-F60
Upper Dacite
Lower Dacite
Oxide in starting material

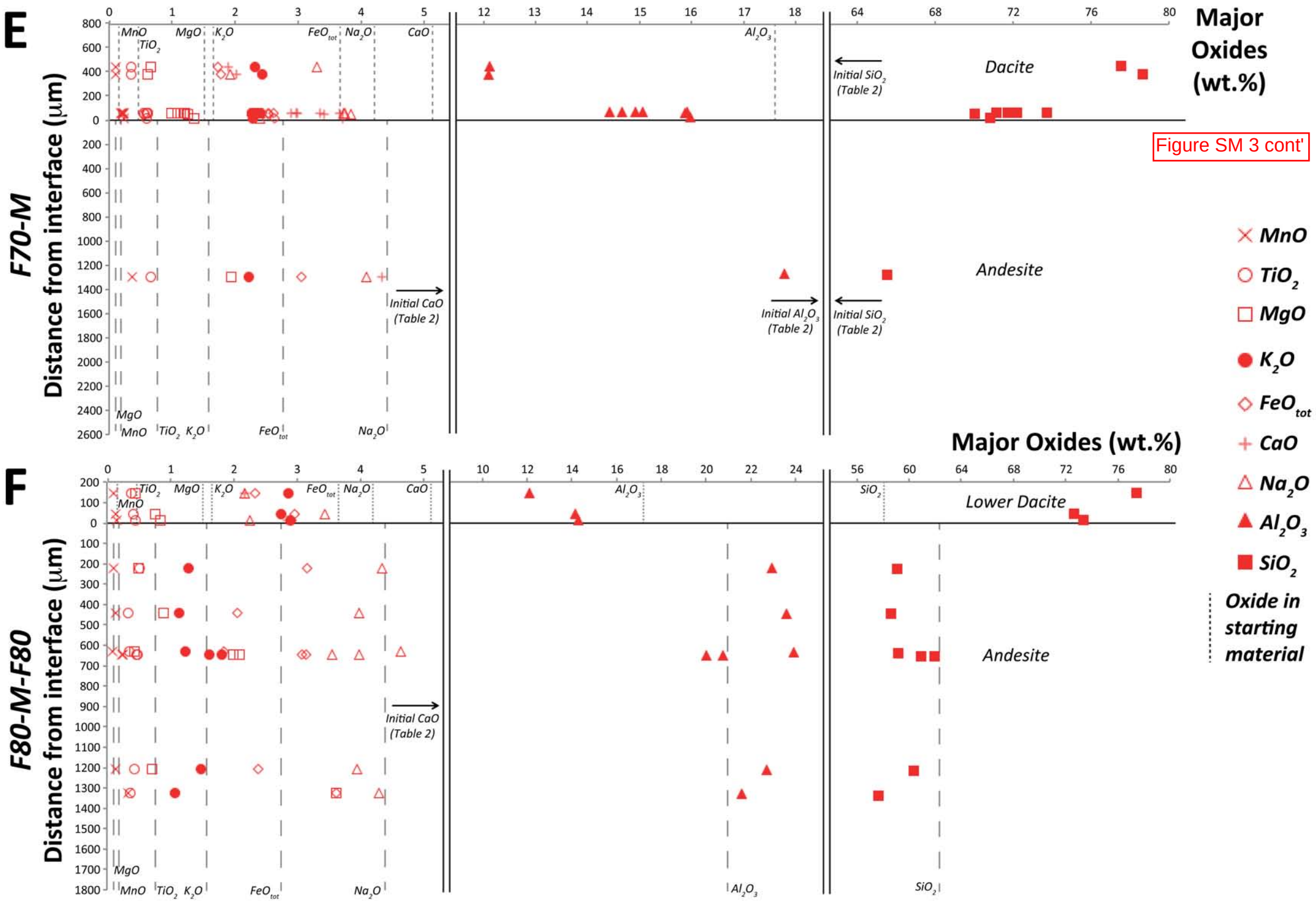
E
F70-M
Distance from interface (μm)
MnO
TiO2
MgO
K2O
FeOtot
Na2O
CaO
Al2O3
SiO2
Initial CaO (Table 2)
Initial Al2O3 (Table 2)
Initial SiO2 (Table 2)
Dacite
Andesite
Major Oxides (wt.%)
Figure SM 3 cont'
F
F80-M-F80
Lower Dacite
Oxide in starting material

Figure SM 4

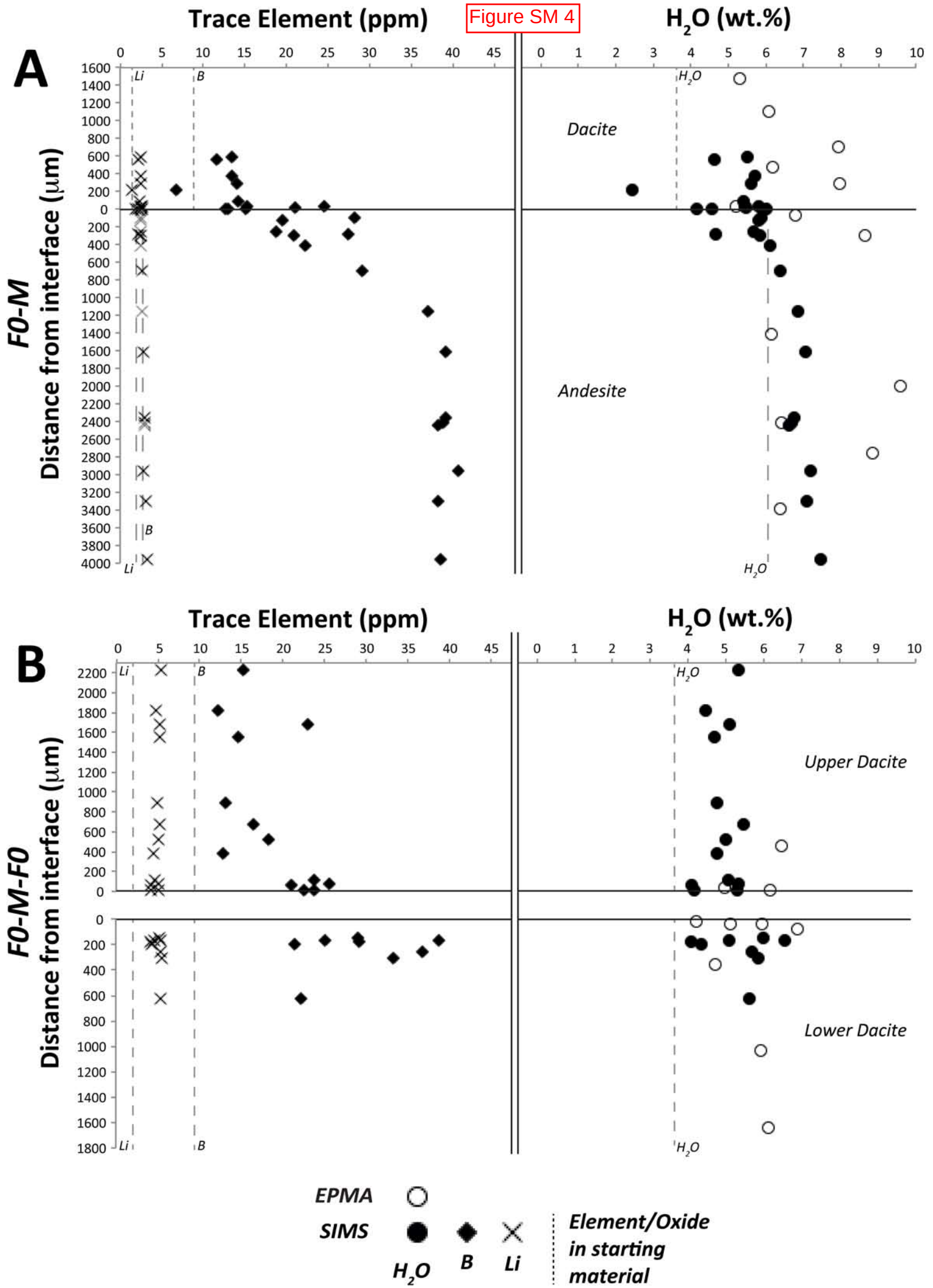
A
Trace Element (ppm)
H2O (wt.%)
Distance from interface (μm)
F0-M
Li
B
H2O
Dacite
Andesite
B
Li
H2O
B
Trace Element (ppm)
H2O (wt.%)
Distance from interface (μm)
F0-M-F0
Li
B
H2O
Upper Dacite
Lower Dacite
Li
B
H2O
EPMA
SIMS
H2O
B
Li
Element/Oxide in starting material

Figure SM 4 cont'

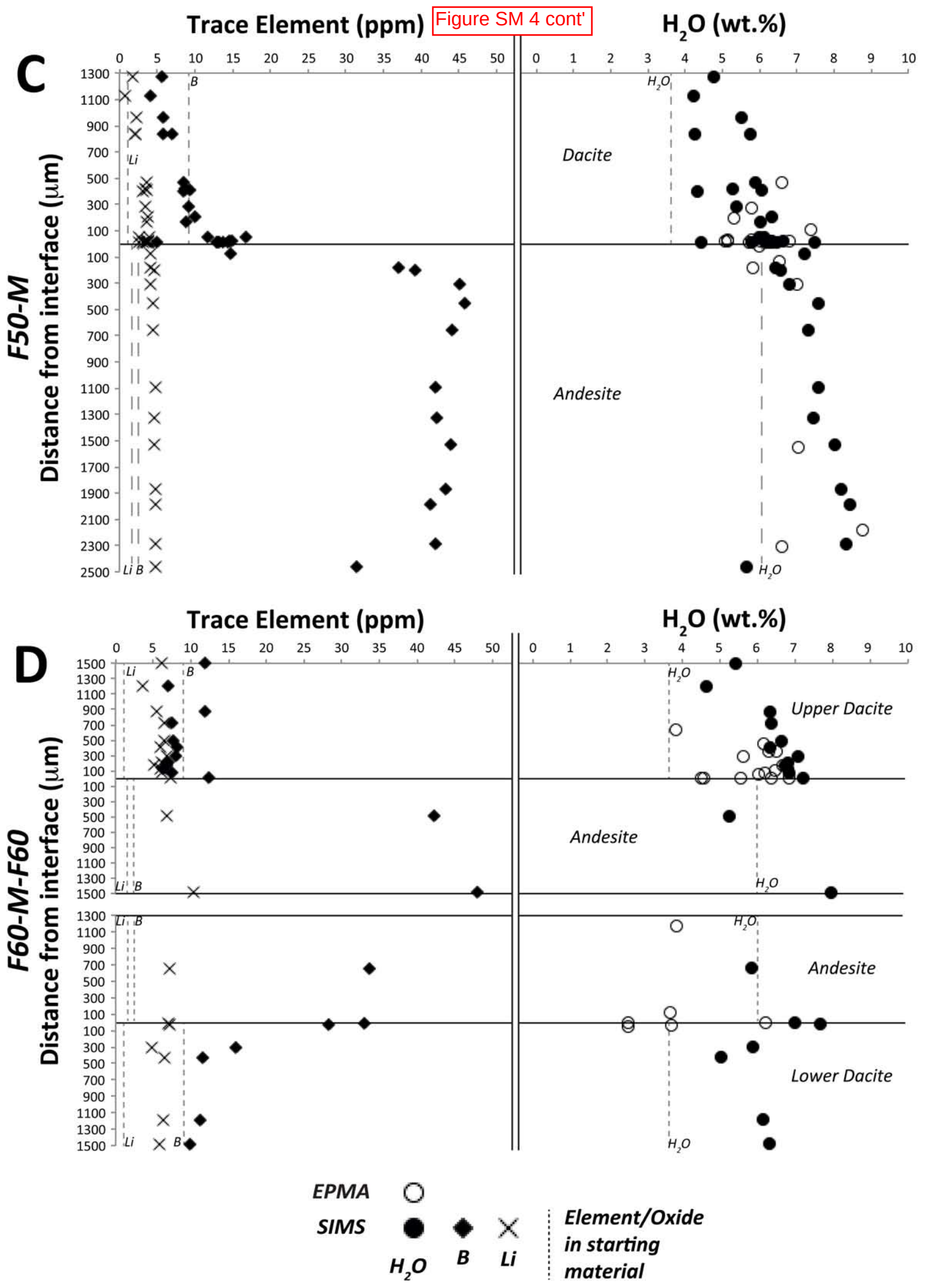

Figure SM 4 cont'

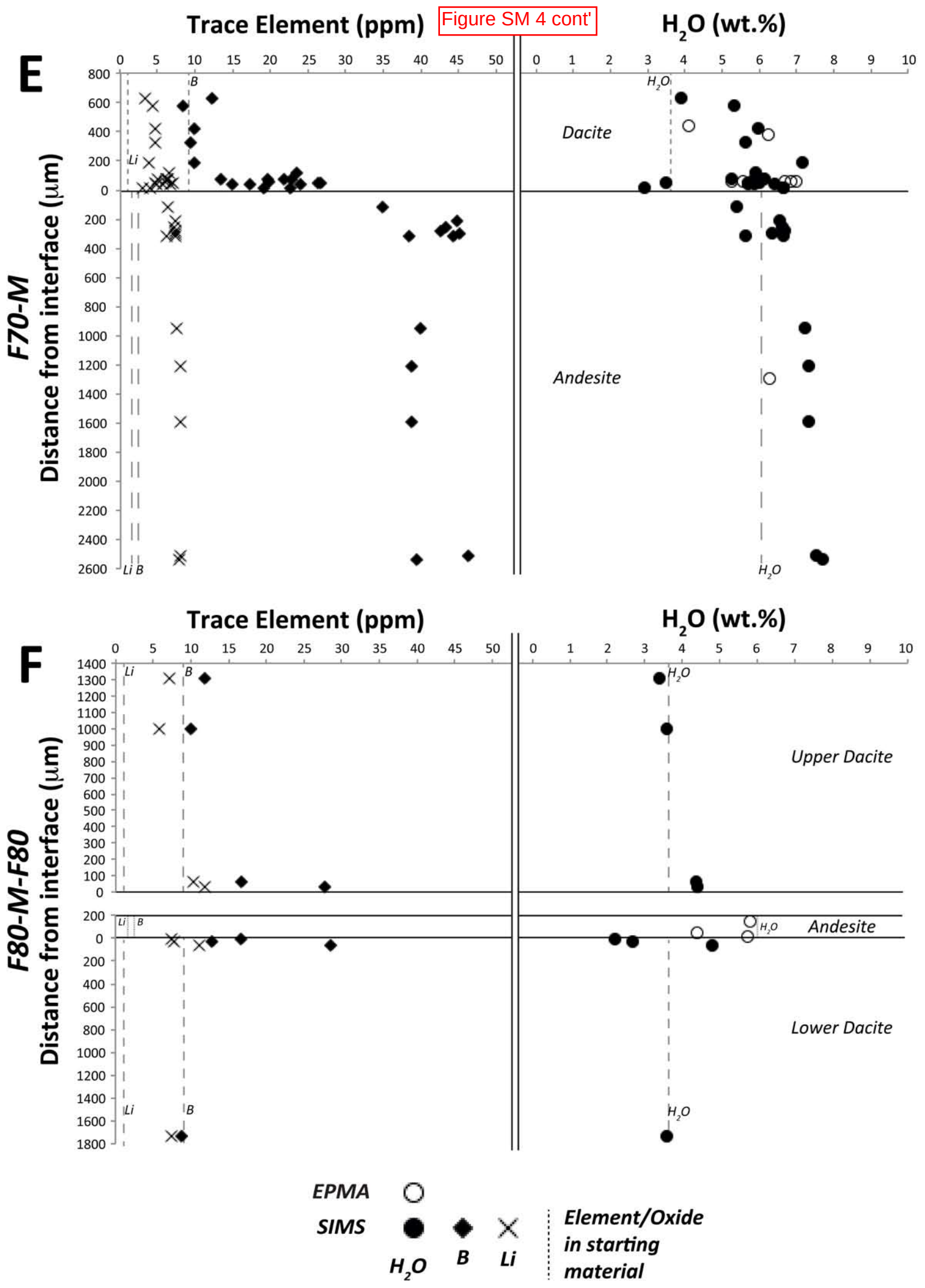

Figure SM 4 cont'